Master's Thesis

MEG II 実験輻射崩壊検出器の電極開発と動作試験

Development and performance of the electrode of the Radiative Decay Counter in the MEG II experiment

February 7, 2025

Department of Physics
238S110S
Hiromu Suzuki

Master's Course, Graduate School of Science
Kobe University

Abstract

The $\mu \to e\gamma$ decay, predicted in new physics models beyond the Standard Model of particle physics, is being searched in the MEG II experiment. The Radiative Decay Counters (RDCs) placed on the beam axis detect low-momentum positrons from the Radiative Muon Decay (RMD) bound to the beam axis. The RMD is one of the sources of the background. The downstream RDC is in operation; the upstream RDC is currently under development in this study. An aging test using X-rays with the irradiation dose of $54\,\mathrm{C/cm^2}$, corresponding to about the half of that expected in MEG II from the data taking was performed. Fluorine deposits, inducing the degradation of the gas gain were observed. To realize stable operation, the electrode structure and the quality of the pillars on the electrode were improved by using an alternative material. The detection efficiency reached more than 45 % with a single layer. In addition, electrodes with conductive strips and protective covers for improving its rate capability were fabricated, and their performance was evaluated in terms of the stability and quenching capability. It was found that the width and effective resistance of the cover for the conductive strips should exceed certain values for stable operation.

Contents

Chapter 1

Introduction

Modern elementary particle physics is founded on the Standard Model (SM). The SM successfully describes the electroweak interaction and has been validated through experimental evidence. However, the discovery of neutrino oscillation [1] [2] has revealed that neutrinos have mass, which cannot be accommodated within the original framework of the SM. It implies the existence of new physics beyond the SM.

In the SM, the lepton flavor must be conserved. However, charged Lepton Flavor Violation (cLFV) processes are predicted to occur in various new physics models within the sensitivity of modern experiments. The discovery of such a process would provide direct evidence for physics beyond the SM.

A search for one of the cLFV processes, the $\mu \to e\gamma$ decay, was conducted in the MEG experiment from 2009 to 2013, achieving a sensitivity of 5.3×10^{-13}. This search set the upper limit on the branching ratio, $\mathcal{B}(\mu^+ \to e^+\gamma) < 4.2 \times 10^{-13}$, at 90 % confidence level in 2016 [3]. The $\mu \to e\gamma$ is a two-body decay, emitting a photon and a positron back-to-back, both having an energy of half of the muon mass $m_\mu/2$. The Radiative Muon Decay (RMD), $\mu \to e\overline{\nu}_e\nu_\mu\gamma$, is also a muon decay process, emitting a photon. The dominant background in MEG is an overlap between a positron from a Michel decay and a photon from the RMD or positron annihilation in flight, both of which have the energy close to $m_\mu/2$, producing a similar characteristic of the $\mu \to e\gamma$ signal.

The MEG II experiment was developed with several significant upgrades: an increased muon beam intensity, enhanced detector resolution, and the introduction of additional detectors for identifying the background events. MEG II aims to search for the $\mu \to e\gamma$ decay at a sensitivity of 6×10^{-14}, representing an order of magnitude improvement. The Radiative Decay Counters (RDCs) are proposed as part of these upgrade projects. It is planned to place two new detectors upstream and downstream of the muon stopping target centered on the beam axis to detect positrons from the RMD for identification of the accompanied photons. While the downstream RDC (DS-RDC) has been in operation since 2017, the upstream RDC (US-RDC) is currently under development by the MEG II Japan group, consisting of laboratories at the University of Tokyo and Kobe University. In 2023, the first result of the MEG II physics run in 2021 was reported. It provided the most stringent upper limit to date, $\mathcal{B}(\mu^+ \to e^+\gamma) < 3.1 \times 10^{-13}$, with a combined sensitivity of 4.3×10^{-13} when integrated with the final MEG result [4]. This result does not include the contribution of the US-RDC.

The US-RDC will further increase the acceptance for the RMD and the sensitivity. It will operate in a high-intensity (7×10^7 μ^+/s) and low-momentum ($28\,\mathrm{MeV}/c$) muon beam environment, imposing difficult requirements. The US-RDC must minimize interference with the muon beam, detect low-momentum positrons with high efficiency, and achieve fast-timing resolution. Furthermore, the detector diameter has to be extended as large as $16\,\mathrm{cm}$ due to constraints from the acceptance for the RMD positrons. A Resistive Plate Chamber with Diamond-Like Carbon-based electrodes (DLC-RPC) has been chosen and developed as the US-RDC technology due to its low material budget and high-rate capability. Previous studies demonstrated its suitability for these requirements as follows; verification of compliance of the DLC-RPC with material budget, timing resolution, and detection

efficiency requirements was done [5]; evaluation of its rate capability($1\,\mathrm{MHz/cm^2}$) and introduced improvements to an electrode structure to enhance it were studied [6]; and also [7], the investigations on radiation hardness using fast neutrons and X-rays were performed, finding that no degradation of its performance was observed with three order of magnitude lower irradiation dose than the expected dose in MEG II. Additionally, a new module for demonstration of the rate capability improvement by implementing the structure suggested [6] was produced and tested; however, its operation was prevented by a distorted electric field.

This thesis focuses on the development of the US-RDC. The chapters are organized as follows.

- Chapter 2 provides an overview of $\mu \to e\gamma$ physics.
- Chapter 3 describes the principles of the MEG II experiment.
- Chapter 4 reviews the requirements for the US-RDC, the operation principle of conventional RPCs, and summarizes past studies.
- Chapter 5 discusses the latest study on the radiation hardness of the DLC-RPC.
- Chapter 6 discusses on electrode structure improvements.
- Chapter 7 summarizes the findings and presents the conclusion.

Chapter 2

$\mu \to e\gamma$ physics

In this chapter, physics motivation of the $\mu \to e\gamma$ decay, being searched for in the MEG II experiment, is presented.

2.1 Muon in the Standard Model

Modern elementary particle physics is based on the Standard Model (SM), which is a gauge theory describing the interactions of quarks and leptons. Physics of electroweak ($\mathcal{O}(100)$ GeV scale) interaction is described successfully and experimentally proved.

The SM particles are shown in Figure 2.1. It consists of 12 fermions, 5 gauge bosons, and the Higgs boson. The muon is a charged lepton, which is categorized in the second generation. The main muon decay channels through the SM processes are presented in Table 2.1.

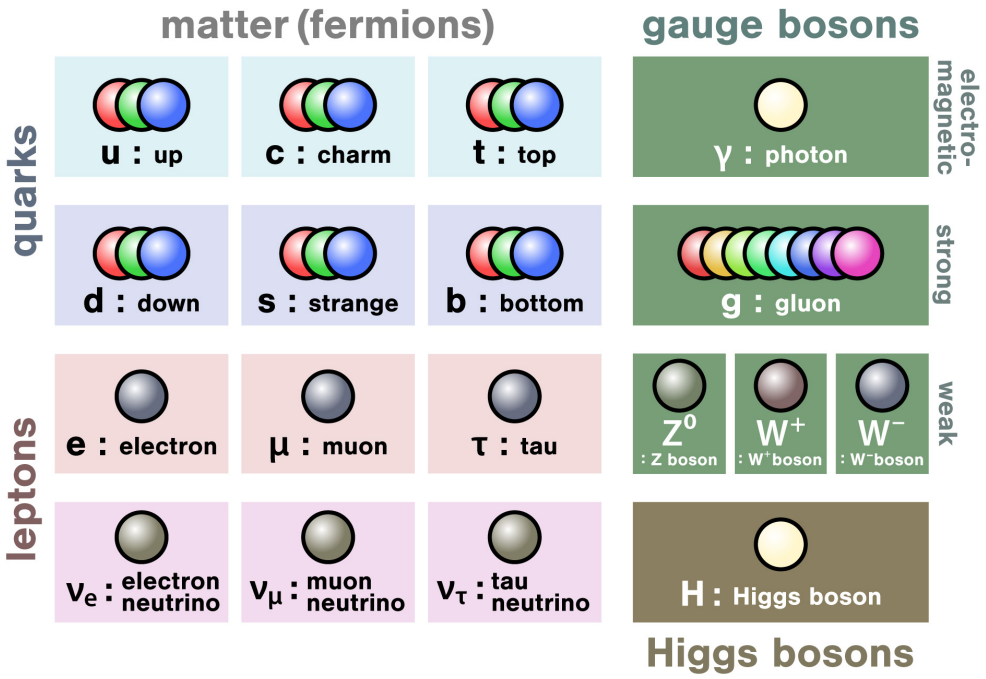

Figure 2.1: Particles in the SM [8].

Table 2.1: Muon decay modes (E_e: Electron energy, E_γ: Photon energy).

Decay mode	Branching ratio	Notes
Michel decay $\mu \to e\overline{\nu}_e\nu_\mu$	$\sim$1 [9]	-
Radiative muon decay $\mu \to e\overline{\nu}_e\nu_\mu\gamma$	$(6.0\pm0.5)\times10^{-8}$ [9]	$E_e > 45\,\mathrm{MeV}$ and $E_\gamma > 40\,\mathrm{MeV}$
	$(1.4\pm0.4)\times10^{-2}$ [10]	$E_\gamma > 10\,\mathrm{MeV}$
$\mu \to e\overline{\nu}_e\nu_\mu e\overline{e}$	$(3.4\pm0.4)\times10^{-5}$ [9]	-

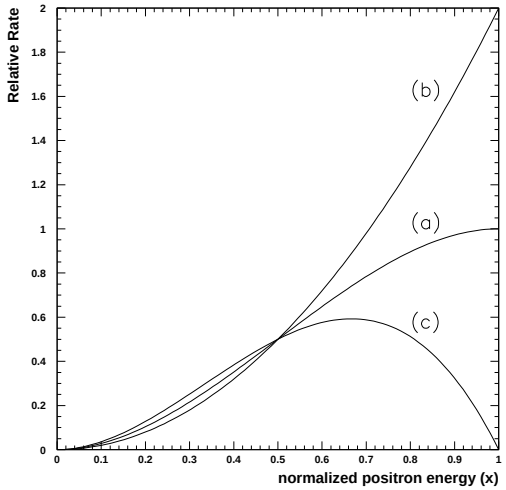

Figure 2.2: Positron energy spectrum from 100 % polarized muon [11].
(a) $\cos\theta_e = 0$; (b) $\cos\theta_e = 1$; (c) $\cos\theta_e = -1$;
x is positron energy normalized by half of the muon mass.

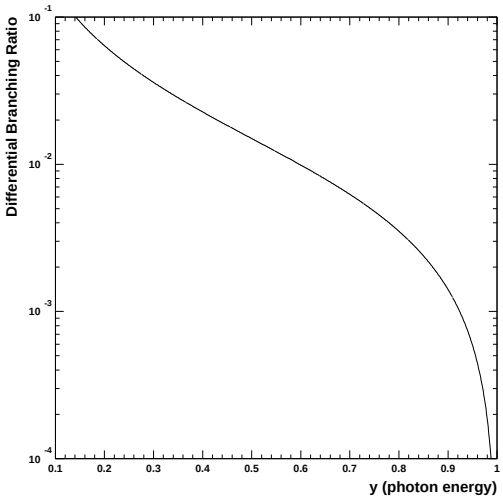

Figure 2.3: RMD photon energy spectrum [11].
y is photon energy normalized by half of the muon mass.

Michel decay

The Michel decay, $\mu \to e\overline{\nu}_e\nu_\mu$, accounts for almost all muon decay modes, as shown in Table 2.1. The differential branching ratio is given by [11]:

$$\frac{d^2\Gamma(\mu^\pm \to e^\pm\nu\overline{\nu})}{dx\,d\cos\theta_e} = \frac{m_\mu^5 G_F^2}{192\pi^3}x^2[(3-2x) \pm P_\mu\cos\theta_e(2x-1)]. \tag{2.1}$$

Here, m_μ is the muon mass, G_F is the Fermi coupling constant, x is the electron energy normalized by half of the muon mass $\left(E_e \cdot \frac{2m_\mu}{m_\mu^2+m_e^2}\right)$ and θ_e is the angle between the polarization of the muon P_μ and the electron three-momenta. The Michel positron energy spectrum is shown in Figure 2.2. The distribution varies depending on θ_e. In particular, the fraction of the events close to the kinematic endpoint, $x = 1.0$, increases with $\cos\theta_e$.

Radiative muon decay

The Radiative Muon Decay (RMD), $\mu \to e\overline{\nu}_e\nu_\mu\gamma$, is a muon decay process that results in the emission of a photon. Figure 2.3 shows the RMD photon energy spectrum. Photons up to an energy of half of the muon mass can be emitted in this process. In the context of the MEG II experiment, RMD events pose a potential background. If both the RMD positrons and photons have energies close to $52.8\,\mathrm{MeV}$, they may resemble the signal. Furthermore, a positron from a Michel decay overlapped with a photon from an RMD decay, both of which have $E_e \sim m_\mu/2$, may mimic the $\mu \to e\gamma$ signal in

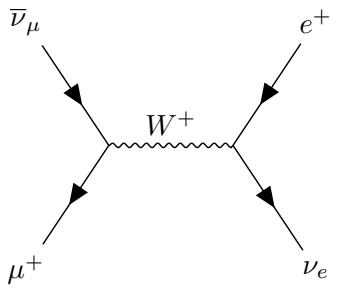

Figure 2.4: An diagram of the Michel decay.

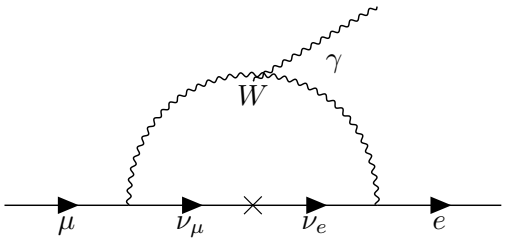

Figure 2.5: An example of the $\mu \to e\gamma$ decay diagrams induced by the contribution from neutrino oscillations.

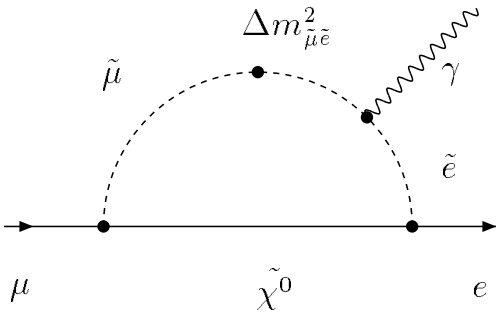

Figure 2.6: A diagram of the $\mu \to e\gamma$ decay through slepton flavor mixing [11].

MEG II. Further discussions about this background are given in Section 3.1.

2.2 $\mu \to e\gamma$ decay

The $\mu \to e\gamma$ decay is one of charged Lepton Flavor Violation (cLFV) processes. Its discovery would be clear evidence of physics beyond the SM. Although the SM assumes that lepton-flavor quantum numbers are conserved, the discovery of neutrino oscillations [1, 2] revealed that neutrinos have mass, and lepton-flavor quantum numbers are not conserved. This violation occurs in the quark and neutral lepton sectors, and several new physics models suggest that it can also appear in the charged lepton sector. The decay branching ratio has been theoretically predicted taking into account neutrino oscillations [11] [12].

The branching ratio is calculated as follows:

$$\mathcal{B} = \frac{3\alpha}{32\pi} \left| \sum_{i=2,3} U^*_{\mu i} U_{ei} \frac{\Delta m^2_{i1}}{M^2_W} \right|^2 \sim 10^{-54} \tag{2.2}$$

where α is the fine-structure constant, each U_{ij} represents the lepton flavor mixing matrix (Pontecorvo-

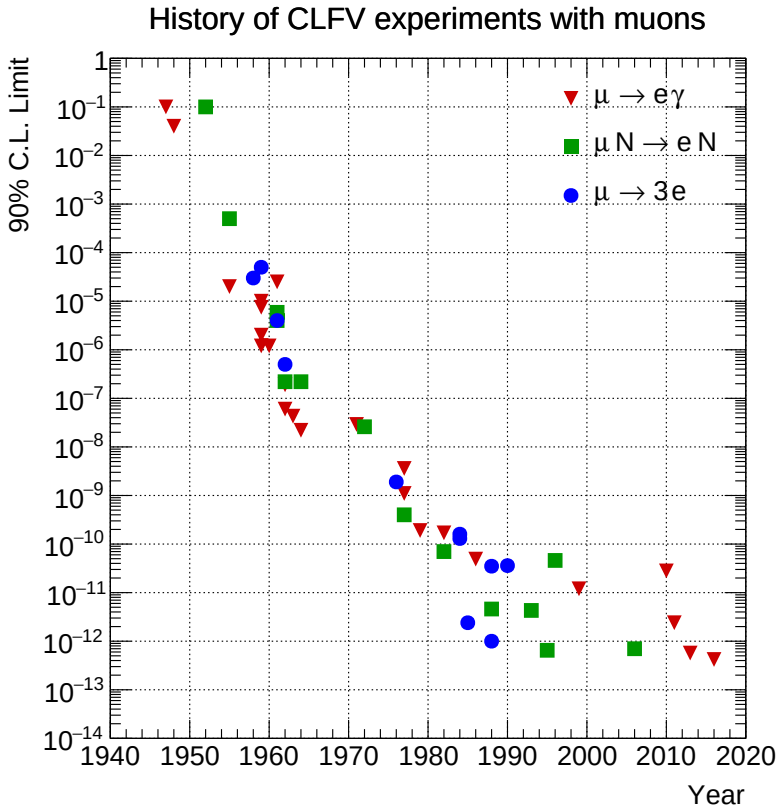

Figure 2.7: The upper limits on cLFV processes reported up to 2018 [15].

Maki-Nakagawa-Sakata matrix), M_W is the mass of the W boson, and Δm^2_{i1} represents neutrino mass squared differences. Eq. 2.2 shows that the branching ratio of the $\mu \to e\gamma$ is extremely small due to small neutrino mass and it is not observable with our current experimental sensitivities.

However, it can be observable at the branching ratios of $\mathcal{O}(10^{-12} - 10^{-14})$ for example, in new physics models, in which the Grand Unified Theory (GUT) [13] and the Supersymmetric model [14] are introduced, where flavor mixing through scalar leptons is present. For this reason, various experiments searching for the $\mu \to e\gamma$ decay have been carried out to find evidence for new physics models.

2.3 Experiment searching for $\mu \to e\gamma$ decay

The upper limits on three muon decay modes: $\mu \to e\gamma$, $\mu \to eee$, and $\mu N \to eN$ to 2018 are shown in Figure 2.7. The current upper limit on the $\mu \to e\gamma$ decay, $\mathcal{B}(\mu^+ \to e^+\gamma) < 3.1 \times 10^{-13}$ at the 90 % confidence level, is provided combining the 2021 MEG II data and the final MEG result [4].

Chapter 3

The MEG II experiment

The MEG II experiment, searching for the $\mu \to e\gamma$ decay using the most intense direct current muon beam to date, is introduced. Firstly, signal and background kinematics are presented in this chapter. Secondly, the experimental apparatus is introduced. Finally, the sensitivity of the MEG II experiment is discussed.

3.1 The signal and background

3.1.1 The Signal

The signal event, the $\mu \to e\gamma$ decay, has a kinematical configuration of a two-body decay, where a position and a photon are emitted back-to-back. Both particles will have the energy of $52.8\,\mathrm{MeV}$, half of the muon mass $m_\mu/2$. A schematic drawing of the signal event is shown in Figure 3.1.

The expected number of signals is calculated by the formula below:

$$N_{\mathrm{sig}} = R_{\mu^+} \times T \times \Omega \times \mathcal{B} \times \epsilon_\gamma \times \epsilon_{e^+} \times \epsilon_{\mathrm{s}}. \tag{3.1}$$

Here, R_{μ^+} is the muon stopping rate, T is the measurement time, Ω is the solid angle subtended by the photon and positron detectors, $\mathcal{B}$ is the branching ratio of the $\mu \to e\gamma$ decay, ϵ_γ, ϵ_{e^+}, and ϵ_{s} are the efficiency of the photon and positron detectors and the selection efficiency, respectively.

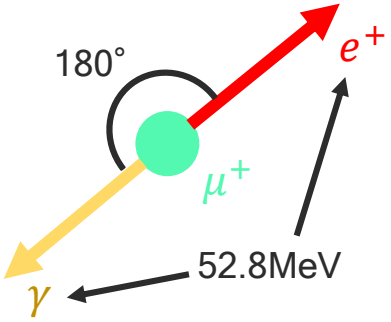

Figure 3.1: A schematic drawing of a signal event of the $\mu \to e\gamma$ decay.

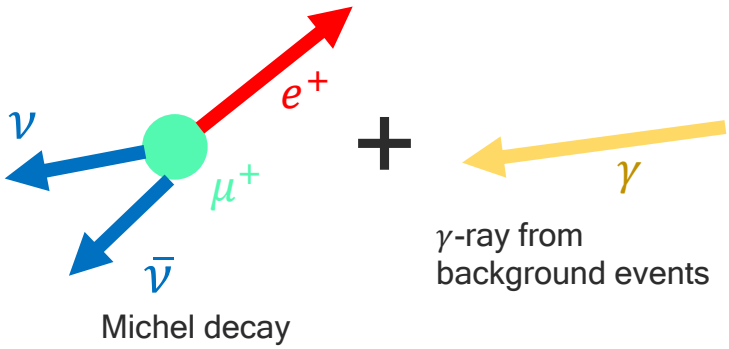

Figure 3.2: A schematic drawing of an accidental background.

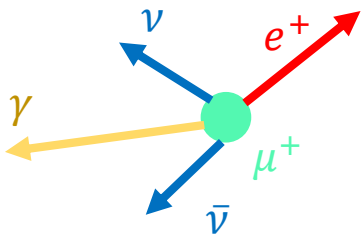

Figure 3.3: A schematic drawing of an RMD.

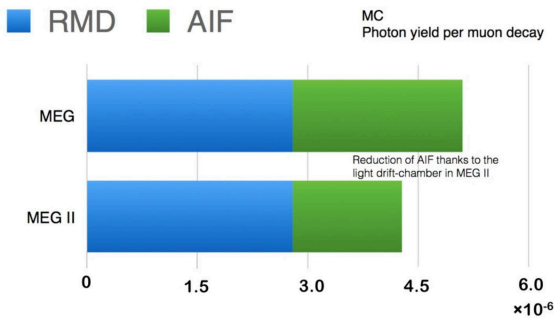

Figure 3.4: Sources of the background photons in the accidental background events for MEG and MEG II [15].

3.1.2 Accidental background events

The main background in the MEG II experiment is an accidental coincidence of a background positron and a background photon. Figure 3.2 shows a schematic drawing of the accidental background. The background positron comes from the Michel decay. As discussed in Section 2.1, a number of high-energy positrons around $52.8\,\mathrm{MeV}$ is generated, which gives a positron similar to that from the $\mu \to e\gamma$ decay. The background photons come from either radiative muon decay (RMD) or positron annihilation-in-flight (AIF). As shown in Figure 3.3, the RMD emits a positron and a photon. This photon, whose energy is around $52.8\,\mathrm{MeV}$, resembles that from the signal event. The number of RMD and AIF events per muon decay is shown in Figure 3.4. The reduction of the material budget in the Cylindrical drift chamber decreased the AIF photons as detailed in Section 3.2.2. On the other hand, the RMD still remains a dominant accidental background source in MEG II.

The number of the accidental backgrounds is described as

$$N_{\mathrm{acc}} \propto R_{\mu^+}^2 \times \Delta E_\gamma^2 \times \Delta E_e \times \Delta p_{e^+} \times \Delta \Theta_{e^+\gamma}^2 \times \Delta t_{e^+\gamma} \times T, \tag{3.2}$$

where p_{e^+} is the positron momentum, $\Theta_{e^+\gamma}$ is the angle between the positron and the photon, $t_{e^+\gamma}$ is the time difference between the positron and photon, and Δ represents the resolution of each parameter.

3.1.3 Background of physical origin

When the RMD emits a positron and a photon back-to-back with two neutrinos, possessing small energies, it can also mimic the signal. This would be a background in MEG II. It is proportional to the beam rate R_{μ^+}, unlike the accidental background. From the relation of $N_{\mathrm{acc}} \propto R_{\mu^+}^2$, the accidental background will be dominant in MEG II since the beam rate is 10 times larger than that in MEG.

3.2 Experimental apparatus

The MEG II experiment is conducted at the Paul Scherrer Institute (PSI), in Switzerland, aiming to search for the $\mu^+ \to e^+\gamma$ decay at a sensitivity on the branching ratio of 6×10^{-14}. The MEG II apparatus is shown in Figure 3.5. Muons produced by the PSI proton accelerator stop at the muon stopping target, where they decay, emitting positrons and photons. The positrons are detected by the positron spectrometer, while the photons are observed by the liquid xenon photon detector. In addition, the RMD is identified by newly installed detectors.

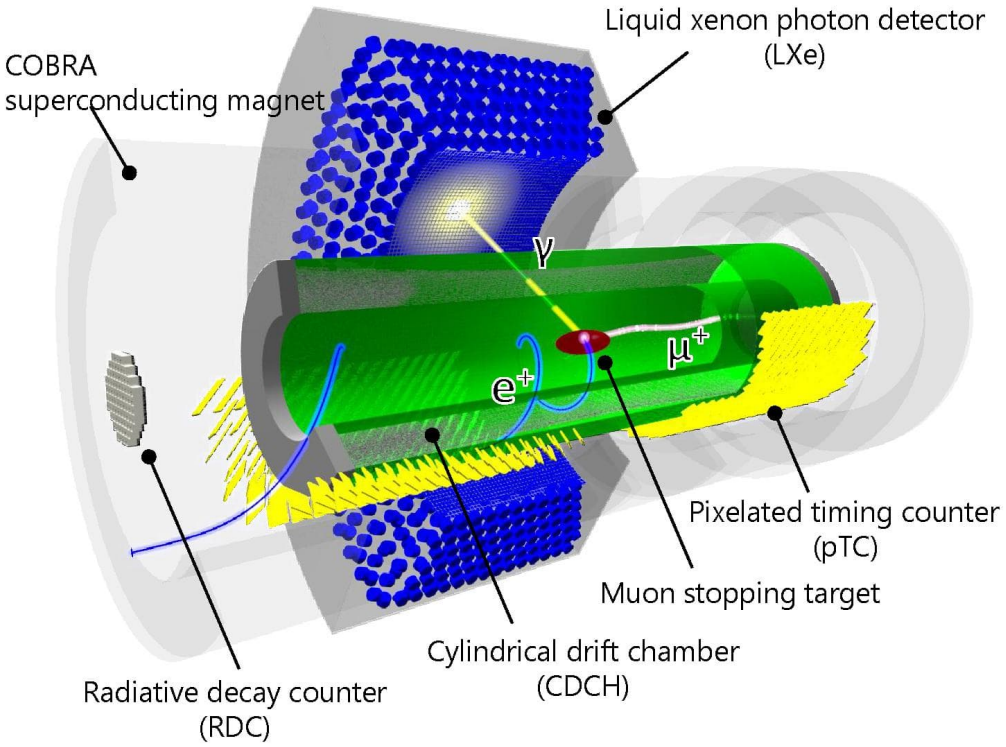

Figure 3.5: The MEG II apparatus [15]. The incoming muons from the right stop at the target, and decay into the signal final state $e^+\gamma$.

3.2.1 Muon beam line and the target

The PSI proton accelerator

Protons are extracted in a Cockcroft-Walton accelerator, which contains the proton source derived from hydrogen atoms. At this stage, they are fed into a pre-accelerator (Injector II), where they are accelerated again to $72\,\mathrm{MeV}$. Finally, the protons are accelerated to $590\,\mathrm{MeV}$ in the main ring cyclotron, as shown in Figure 3.6. The proton beam has an intensity of $2.2\,\mathrm{mA}$, a frequency of $50.93\,\mathrm{MHz}$, and a pulse interval of $19.75\,\mathrm{ns}$.

Generating muon beam

Protons collide into a graphite target of $4\,\mathrm{cm}$ thickness, producing pions. These pions decay via $\pi^+ \to \mu^+\nu_\mu$, resulting in surface muons emerging on the target surface. In the SM, the initial muon polarization is expected to be $P_\mu = -1$. However, measurements from the MEG run from 2009 to 2011 estimated the polarization to be $P_\mu = -0.86 \pm 0.02\,(\mathrm{stat})\,^{+0.05}_{-0.06}\,(\mathrm{syst})$ from the data [16], due to the depolarization caused by muon spin interactions during production and transport. Since the muon lifetime is $2.2\,\mu\mathrm{s}$ is much longer than the pulse interval of the proton accelerator and the pion lifetime, $26\,\mathrm{ns}$, the muon beam is regarded as direct current. The muons are then transported to the πE5 beamline.

Beam transport

The muons fed into the πE5 beamline are transported to the muon stopping target through two quadrupole magnets (Triplet I and II), the Wien-filter (Separator), and the Beam Transport Solenoid

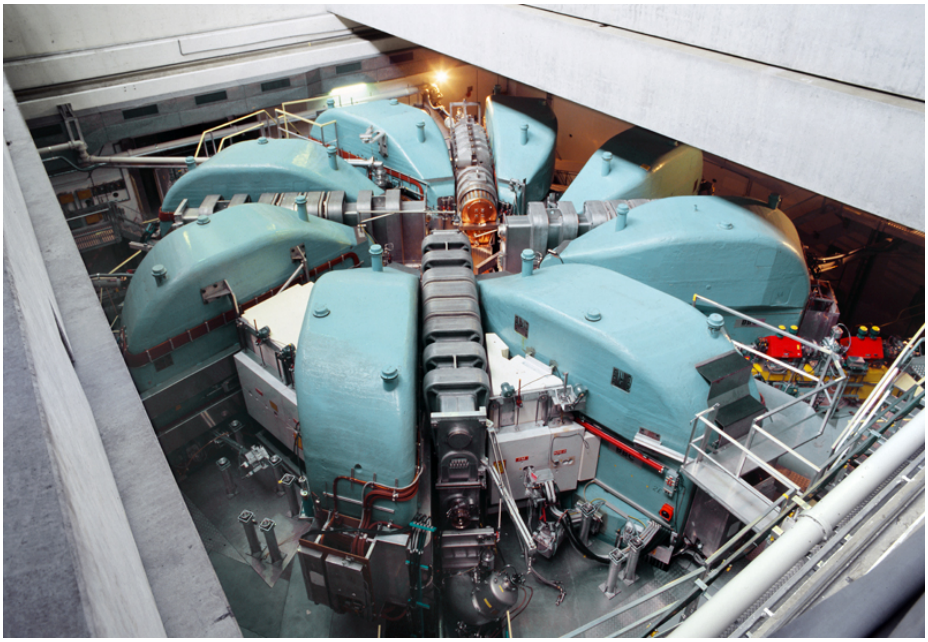

Figure 3.6: The PSI proton cyclotron (Main ring) [17].

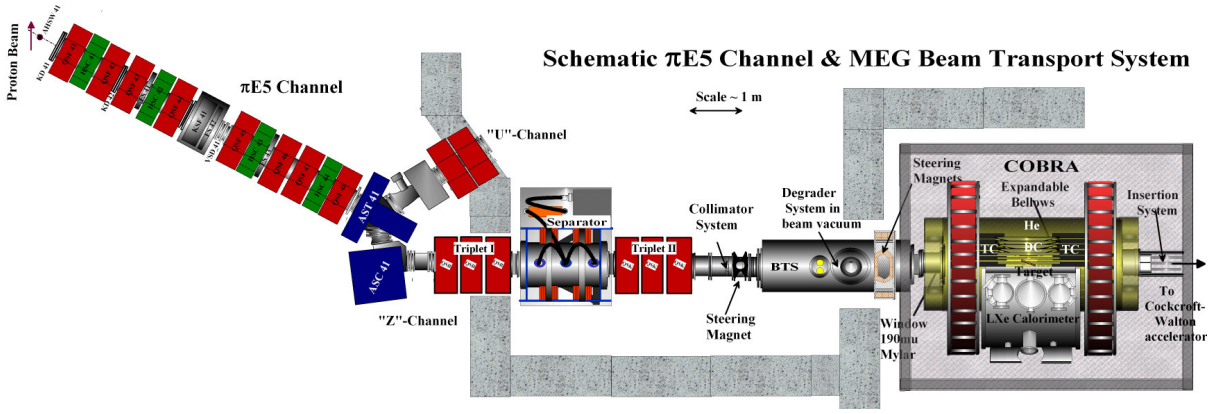

Figure 3.7: πE5 channel and the MEG beam transport system [15].

(BTS) as shown in Figure 3.7. The Wien-filter removes contamination (positrons) in the surface muon beam. The BTS focuses the muon beam to achieve the desired beam profile. The maximum muon beam rate, 2×10^8 μ^+/s, is measured at the collimator located between Triplet II and the BTS. This rate is adjusted using slits (FS41-FS43) in the πE5 channel. The momentum of the muons just before entering the BTS is $28\,\mathrm{MeV}/c$. A Mylar degrader with a thickness of $300\,\mu\mathrm{m}$ (equivalent to $0.105\ \%X_0$) reduces the momentum from $28\,\mathrm{MeV}/c$ to $21\,\mathrm{MeV}/c$ in the BTS to maximize the muon stopping efficiency. The muon is then transported to the MEG II apparatus. When the US-RDC is installed, as described in Chapter 4, the thickness of the Mylar degrader is reduced accordingly.

Muon-stopping target

The muon stopping target is required to satisfy:

- a high muon stopping density
- suppressing multiple Coulomb scattering, positron AIF, and bremsstrahlung

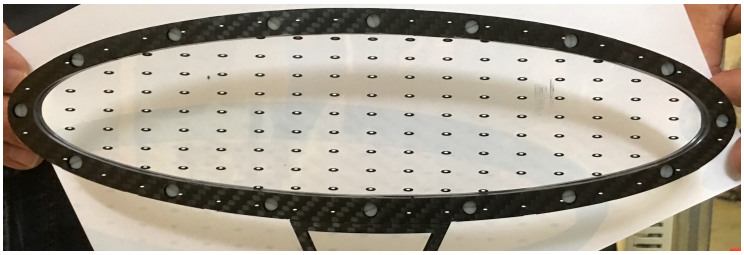

Figure 3.8: The muon stopping target [15].

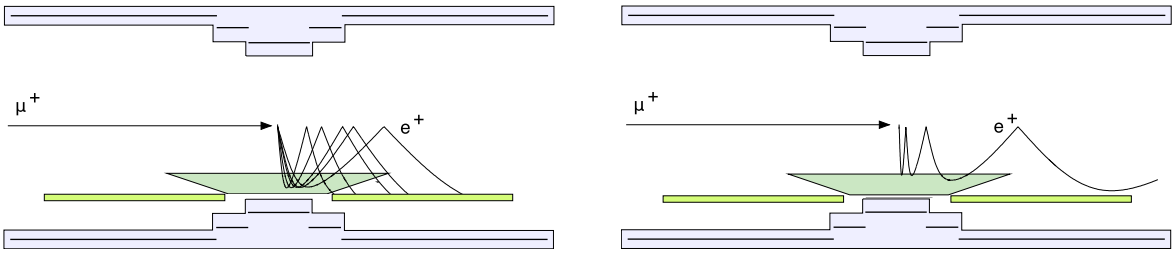

(a) Positrons have a trajectory with a constant bending radius. **(b)** Positrons are swept out quickly.

Figure 3.9: Concept of the COBRA magnet [3]. The schematics are from MEG.

- mechanically stable and remotely moveable for calibrations.

In MEG, a polyethylene target with a thickness of $205\,\mu\mathrm{m}$ for its low material budget was installed at $20.5°$ and its position and its distortion gave an uncertainty of about 5 % to the upper limit of the branching ratio while other detectors gave about 1 %. The thickness of the target in MEG II was reduced to $174\,\mu\mathrm{m}$ on average and placed at $15.0°$ to improve the momentum resolution. To assess its shape and position and reduce uncertainty, the position and shape of the target are monitored precisely using two CCD cameras and LEDs. As shown in Figure 3.8, dots are marked on the target, enabling the measurement of the distortion.

3.2.2 Positron spectrometer

The positron spectrometer consists of:

- COnstant Bending Radius (COBRA) solenoid, providing magnetic field gradient sweeping out positrons
- Cylindrical Drift CHamber (CDCH) for positron tracking
- pixelated Timing Counter (pTC) measuring the timing of positrons.

COBRA magnet

The COBRA magnet was inherited from the MEG experiment and induces a gradient magnetic field along the beam axis. The range is from $0.49\,\mathrm{T}$ at the end to $1.27\,\mathrm{T}$ at the center, which brings a constant bending radius to a high-energy positron, reaching the CDCH. It is also to sweep them out of the spectrometer quickly, as shown in Figure 3.9.

Cylindrical drift chamber

The Cylindrical Drift Chamber (CDCH) is designed as a positron tracker, which has nine layers of 192 drift cells, enabling a precise measurement of the position of positrons. Figure 3.10 shows the assembled CDCH. It is $191\,\mathrm{cm}$ long, with an inner radius of $17\,\mathrm{cm}$, and an outer radius of $29\,\mathrm{cm}$.

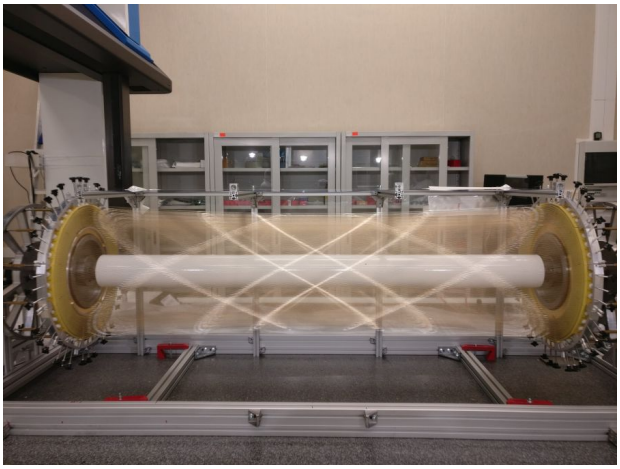

Figure 3.10: Cylindrical drift chamber [15].

Wires are strung in a crisscrossed pattern with alternating signs, creating stereo angles from $6.0°$ to $8.5°$ to allow for longitudinal hit reconstruction.

The CDCH was required to suppress the AIF by reducing its material. Specifically, the gas mixture is helium (He) and isobutane (C_4H_{10}) in the ratio 90:10 for their low material budget with 1 % isopropyl alcohol and 0.5 % oxygen. Sense wires, with a radius is $20\,\mu m$, are made of gold (Au)-plated tungsten (W) and are surrounded by $50\,\mu m$ silver (Ag)-plated aluminum (Al) field wires.

Pixelated timing counter

The pixelated Timing Counter (pTC), upgraded from MEG, enables precise measurement of the positron timing. The MEG timing counter had 30 scintillation counters with photomultiplier tubes (PMTs). However, the timing resolution deteriorated from $40\,ps$ to $70\,ps$ during the MEG physics run due to the degradation of the PMT performance and a large variation of photon passing attributed to the large size of the scintillation counter.

To overcome these issues, in the pTC, 512 scintillation tiles are mounted, as shown in Figure 3.11, instead of 30 scintillation bars and separated into two sectors: upstream and downstream of the target. Two tiles in different widths, as shown in Figure 3.12, are made of an ultra-fast plastic scintillator, BC-422, with dimensions L (Length) $\times$ W (Width) $\times$ T (Thickness) $= 120 \times 40 \times 5\,mm^3$. Six Silicon Photomultipliers (SiPM) are mounted at their edges. After wrapping these modules in a black sheet for light tightness, they are mounted all over the pTC. The timing resolution of a single tile is 80 ps, and the overall timing resolution of the pTC is approximately $35\,ps$, achieved through the segmentation of the scintillation tiles.

3.2.3 Liquid xenon photon detector

The Liquid Xenon photon detector (LXe) measures the energy, timing, and position of photons. Figure 3.13 shows the detection of a photon and PMTs inside of the LXe photon detector in MEG. $900\,L$ of liquid xenon is used as a scintillator and is surrounded by 846 PMTs to detect the scintillation light.

In the MEG experiment, 216 PMTs covered the photon entrance inner face of the LXe detector. However, round-shaped PMTs could not fully cover the region, leading to energy resolution degradation due to non-uniform light collection efficiency. In substituting Multi-Pixel Photon Counters (MPPCs) for PMTs to fully cover the region, it was necessary to overcome the problem that conventional MPPCs were not sensitive to the scintillation light in the vacuum violet (VUV) range (wavelength $\lambda = 175 \pm 5\,nm$) produced by the LXe detector.

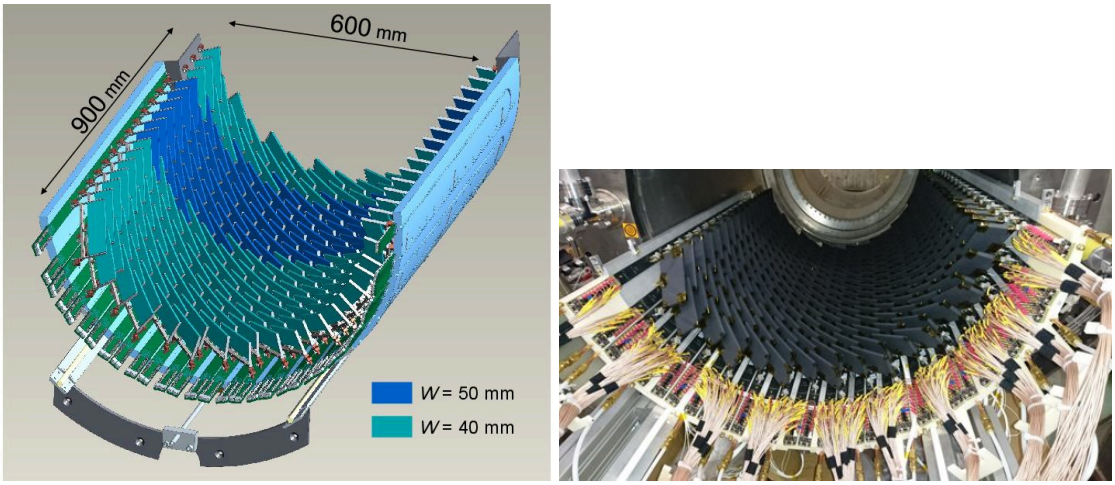

(a) Schematic view [15]. **(b)** Photograph [18].

Figure 3.11: The Pixelated timing counter.

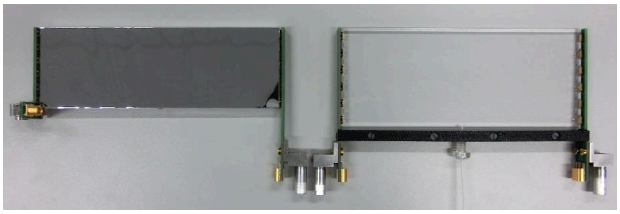

Figure 3.12: Scintillation tiles. Left: Wrapped in a reflector ($W = 40\,\mathrm{mm}$). Right: Before wrapping in a reflector ($W = 50\,\mathrm{mm}$) [15].

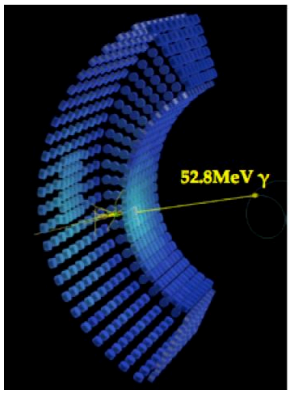

Figure 3.13: The LXe photon detector in MEG [15].

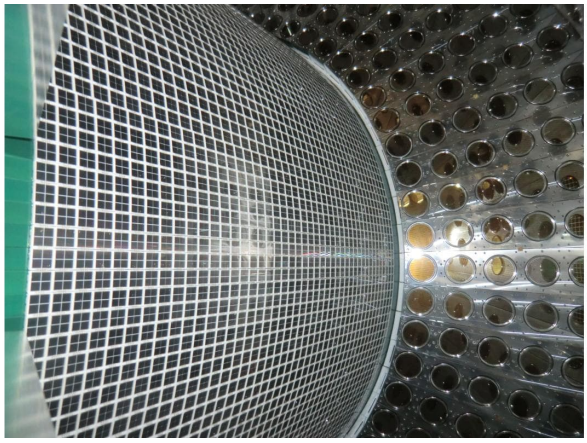

Figure 3.14: The inside of the LXe detector in MEG II [15].

To address this issue, a novel type of SiPM, the VUV-MPPC, was developed for the MEG II experiment to replace the PMTs [19]. Figure 3.14 shows the arrangement of 4092 VUV-MPPCs across the inner face. This new configuration achieves high-granularity photon detection, as illustrated in Figure 3.15.

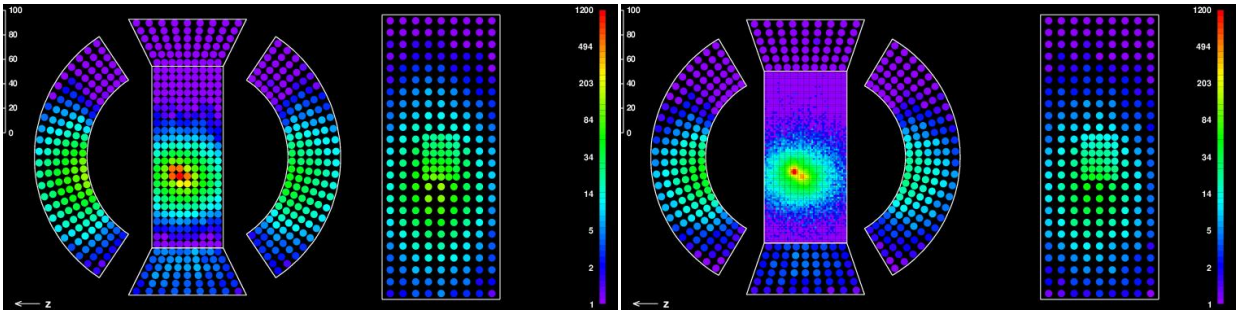

(a) PMTs covering the inner face in MEG. **(b)** MPPCs covering the inner face in MEG II.

Figure 3.15: Comparison of scintillation light detection configurations for the LXe detector [15].

3.2.4 Radiative decay counter

The Radiative Decay Counters (RDCs) are newly installed to suppress the accidental backgrounds in the MEG II experiment. Background photons from the RMD with $E_\gamma > 48\,\mathrm{MeV}$ are regarded as the accidental background sources. Such RMD simultaneously emits low-momentum positrons. ($E_e = 1$–$5\,\mathrm{MeV}$), which are exploited for background identification.

The strategy for identifying the background photons involves detecting these RMD positrons in time coincidence with the detection of the RMD photons in the LXe photon detector. The positrons travel along the magnetic field generated by COBRA with a small radius of approximately $10\,\mathrm{cm}$ at most. Therefore, the RDCs are positioned upstream and downstream on the beam axis, as shown in Figure 3.16.

Approximately 52 % of RMD positrons come upstream, and the rest of them come downstream. Currently, only the downstream RDC is in operation in MEG II, and the upstream RDC remains under development.

The downstream RDC

The pictures of the downstream RDC (DS-RDC) are shown in Figure 3.17. The DS-RDC consists of 12 plastic scintillator bars for positron timing and 76 LYSO crystal calorimeters for positron energy measurement.

Figure 3.18 illustrates the simulated time differences between the DS-RDC and the LXe. The red histogram represents the accidental background events with a peak corresponding to the RMD events, and the blue histogram is for the $\mu \to e\gamma$ event. Figure 3.19 shows that the Michel positrons are detected in the blue histogram. Since the energies of the Michel positrons are higher than those of the RMD positrons, these types of positrons can be distinguished at a high probability.

The DS-RDC demonstrated its capability to detect RMD events in the muon beam during the MEG II physics run in 2021 [20]. The measured time differences between positrons detected by the RDC and photons in the LXe are presented in Figure 3.20. The peak in Figure 3.20 corresponds to the RMD events.

The upstream RDC

The upstream RDC (US-RDC) has been developed in this study. Since the US-RDC will be installed in a high-intensity ($7 \times 10^7\ \mu^+/\mathrm{s}$) and low-momentum ($28\ \mathrm{MeV}/c$) muon beam, it must minimize interference with the muon beam, while it should detect the low-momentum positron with high efficiency. The details of this discussion are presented in Chapter 4.

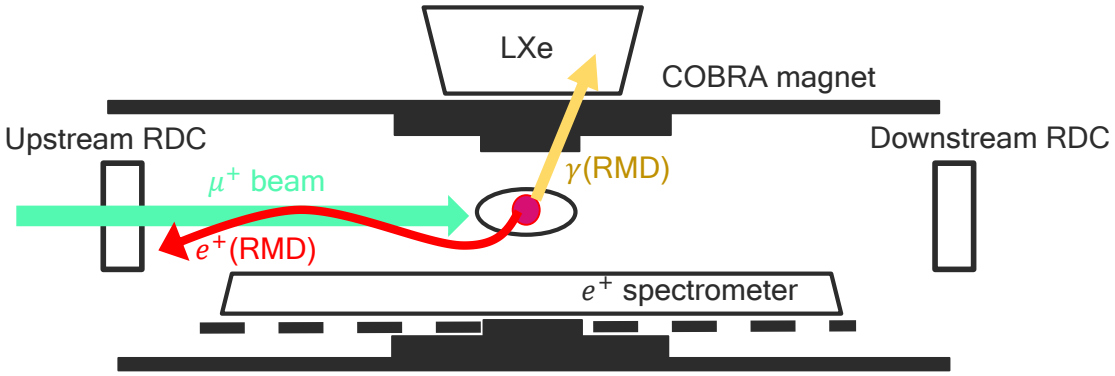

Figure 3.16: RDC in the MEG II experiment.

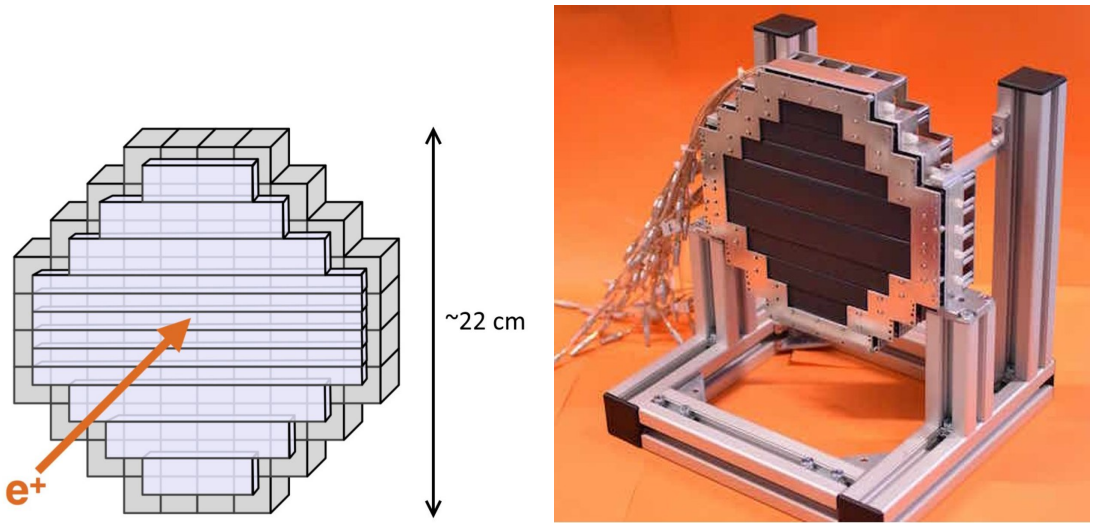

(a) A sketch [15].

(b) A photograph [21].

Figure 3.17: The DS-RDC.

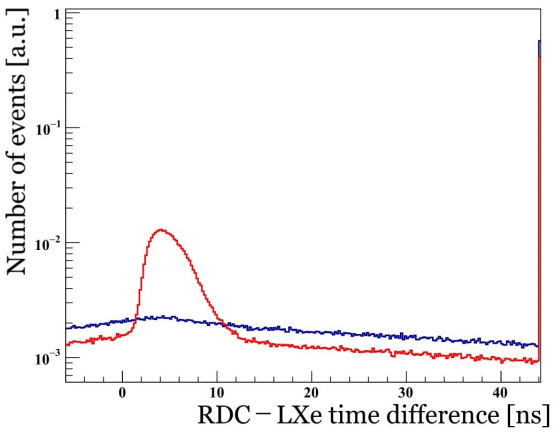

Figure 3.18: Simulated time differences between the DS-RDC and the LXe [15]. Red: Accidental background, Blue: $\mu \to e\gamma$ event.

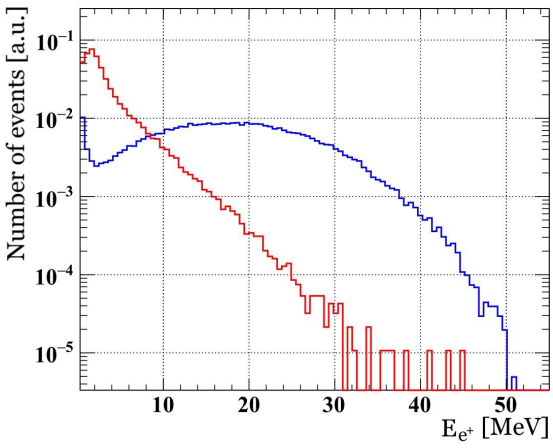

Figure 3.19: The energy spectrum of positrons from RMD decays with $E_\gamma > 48\,\mathrm{MeV}$ (red), and those from the Michel decays (blue) [15].

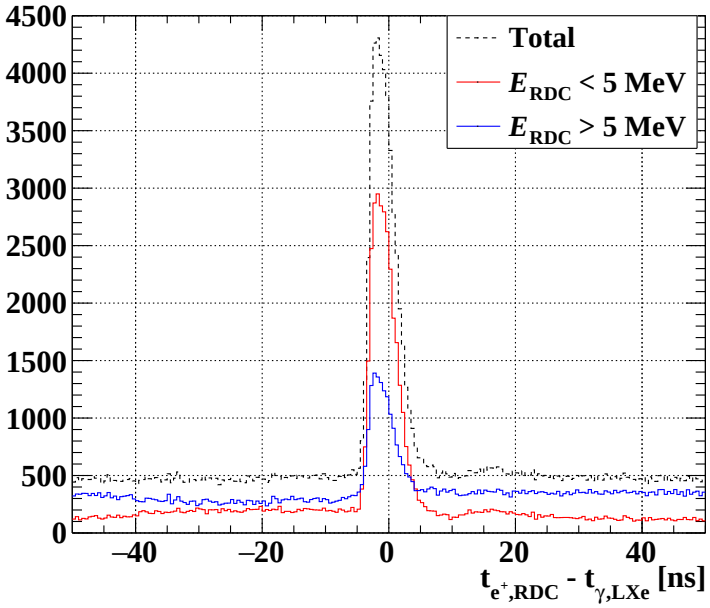

Figure 3.20: Measured time differences between positrons detected in the DS-RDC and photons detected in the LXe photon detector during the MEG II physics run in 2021 [20].

3.2.5 Trigger and DAQ

Waveform digitizer

Full waveform information needs to be taken for the offline pile-up reconstruction and pile-up rejection in MEG II. The DRS4 is used as the DAQ waveform digitizer [22].

WaveDREAM board

The DRS4-based readout module (WaveDREAM board) was developed for MEG II to handle the threefold increase in the number of channels compared to MEG. It also addresses the need for signal amplification for the SiPMs introduced in MEG II, as the SiPMs have a lower gain than PMTs. The schematic of the WaveDREAM board is shown in Figure 3.21. The board serves both as a trigger and a DAQ module, allowing digitization of input signals with a sampling frequency of up to 5 GSPS / 12 bit. Additionally, it can also carry out continuous trigger operations at a frequency of 80 MHz.

Trigger

Online event reconstructions for triggering purposes are implemented using data from the pTC and the LXe due to their fast response. The trigger system is based on the following three criteria:

- Photon energy;
- Time difference between a positron and a photon; and
- Angle between a positron and a photon.

3.3 Expected sensitivity

The detector performance of MEG and MEG II (the latter achieved on the 2021 dataset) are summarized in Table 3.1. The contribution of the US-RDC is not included in Table 3.1.

The expected sensitivity is presented in Figure 3.22. The data-taking period continues until the end

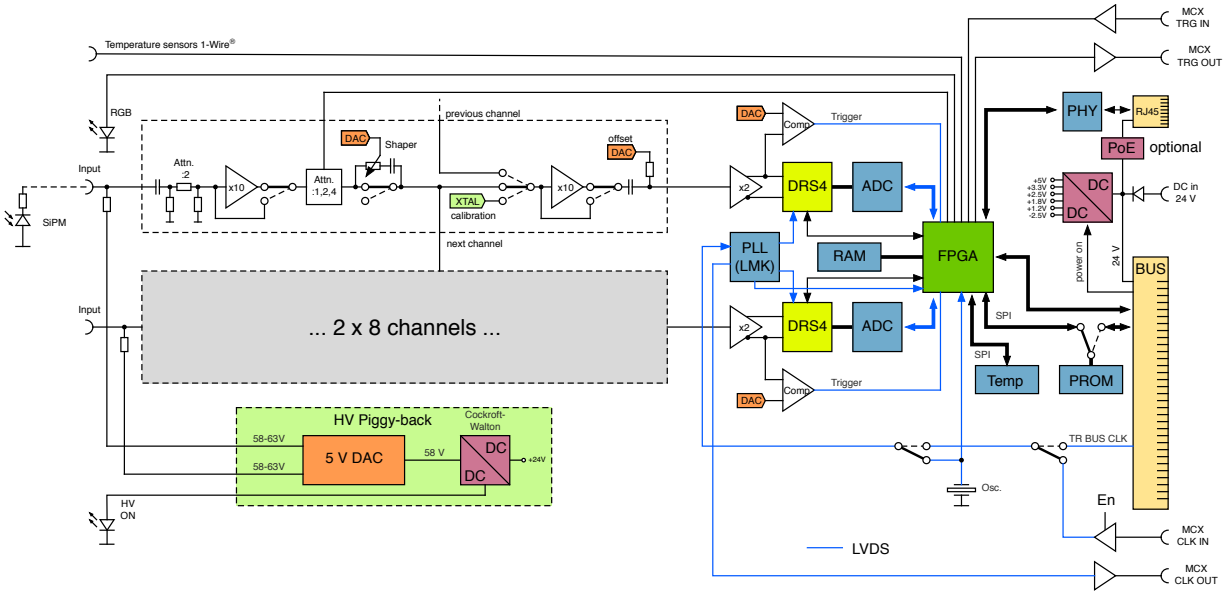

Figure 3.21: The schematics of the WaveDREAM board [15].

Table 3.1: Detector performance [4] [24].

	MEG	MEG II 2021
Positron angular resolution $\sigma_{\theta_{e^+}}$ (mrad)	9.4	7.2
Photon energy resolution σ_{E_γ} (%) $(w < 2\,\mathrm{cm})/(w > 2\,\mathrm{cm})$	2.4/1.7	2.0/1.8
Photon position resolution σ_{x_γ} (mm)	5	2.5
Timing resolution between a positron and a photon $\sigma_{t_{e^+\gamma}}$ (ps)	122	78
Positron detection efficiency ϵ_{e^+} (%)	30	67
Photon detection efficiency ϵ_γ (%)	63	62

of 2026; the total MEG II livetime is expected to be 60 - 80 weeks. Considering improvements in trigger efficiency, which affect the livetime, and the adjustment of the muon beam rate to $4 \times 10^8\ \mu^+/\mathrm{s}$ to maximize sensitivity, expected to reach 6×10^{-14} within 60 weeks of livetime [23].

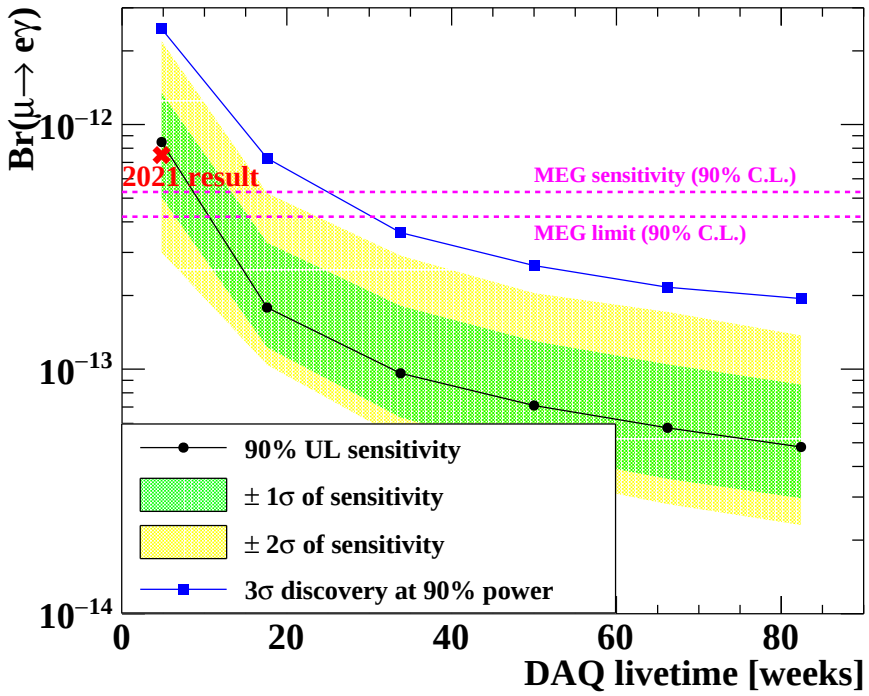

Figure 3.22: Expected sensitivity as a function of the experimental livetime [23].

Chapter 4

Upstream Radiative Decay Counter (US-RDC)

4.1 Requirements for the US-RDC

The upstream RDC (US-RDC) identifies photons from RMDs by detecting the 1–5 MeV positron emitted simultaneously as shown in Figure 3.16. The US-RDC will be installed on the beam axis of a high-intensity and low-momentum muon beam. The hit distributions of the RMD positrons and the muon beam have standard deviations of $\sigma = 2.8\,\mathrm{cm}$ and $\sigma = 2.0\,\mathrm{cm}$, respectively, in the US-RDC as shown in Figure 4.1. Both distributions are centered around the beam axis. Therefore, a detector design with a hole at the center is not suitable for this configuration. To minimize interference with the muon beam, a detector with a low material budget is required.

The requirements for the US-RDC are as follows:

1. Material budget: less than 0.1 % X_0
2. Rate capability: $3\,\mathrm{MHz/cm^2}$
3. Radiation hardness: operation for 20 weeks
4. Detection efficiency: more than 90 % for Minimum Ionizing Particles (MIP)
5. Timing resolution: less than $1\,\mathrm{ns}$
6. Detector size: $16\,\mathrm{cm}$ ϕ.

The US-RDC is designed to measure only the timing, unlike the DS-RDC. It does not measure energy because it would introduce excessive material for energy measurements. Adopting a detector combining SiPM and scintillation fibers was once considered in previous studies. However, it did not meet the requirements in terms of radiation hardness and detection efficiency. Instead, a Resistive Plate Chamber with Diamond-Like Carbon-based electrodes (DLC-RPC) has been chosen as an option and developed as the US-RDC in this study.

4.2 Resistive Plate Chamber

The Resistive Plate Chamber consists of two parallel high-resistivity electrodes and operates by applying high voltage to the gas gap. A one-layer bulk RPC is shown in Figure 4.2. Passing particles ionize the gas, and an avalanche is caused by the electric field. The signal generated by the avalanche is induced to the readout strips through insulators. Electric currents are quenched by the charges remaining on the resistive plate for a while. The detailed operation principle of the RPC detector is described below.

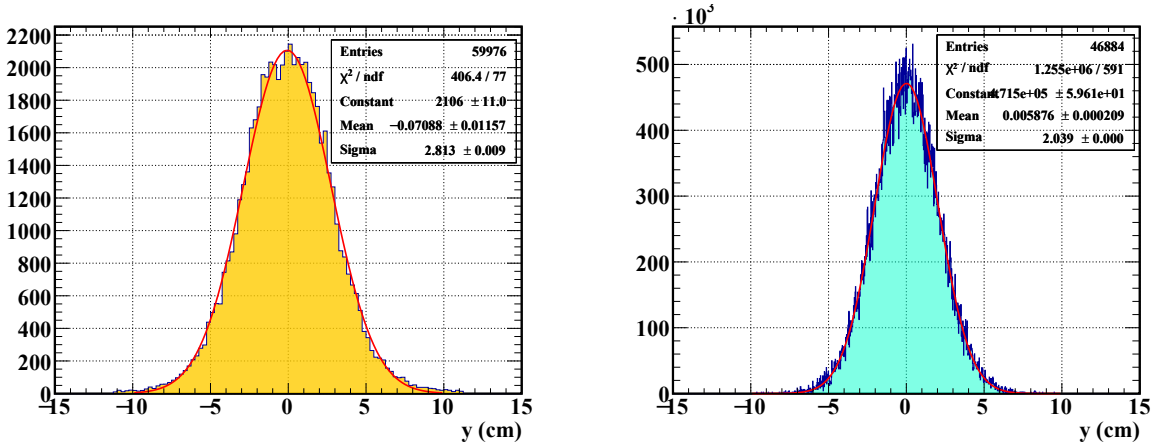

(a) RMD positron. **(b)** Muon beam.

Figure 4.1: Simulation of the hit distributions in the upstream RDC for (a) the positrons from the radiative decay and (b) the muon beam [21].

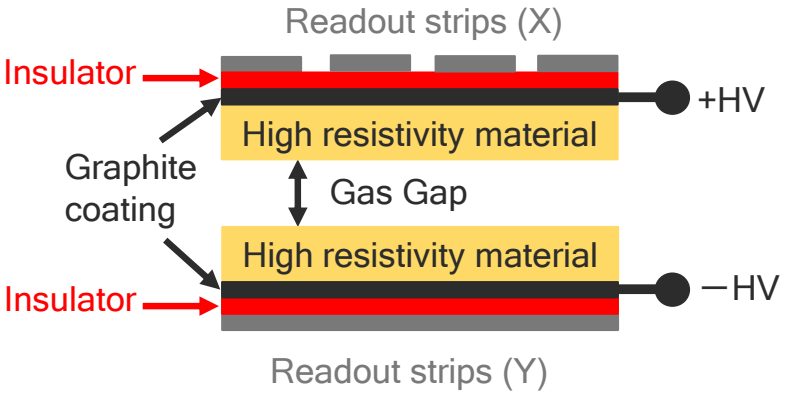

Figure 4.2: A schematic drawing of a single-gap bulk RPC.

4.2.1 Gas amplification process

The avalanche process in RPCs is described in terms of the Townsend coefficient α and the attachment coefficient η. The possibility of having $n+1$ electrons at position $z+\delta z$ is expressed as $n\alpha\delta z$, given that n electrons exist at position z in an avalanche. The possibility of electron attachment forming anions as they are traveling through δz in the gas is $n\eta\delta z$.

The difference between α and η determines the effective amplification possibility. Hence, the avalanche expressed as the number of electrons n is described as

$$\frac{d\bar{n}}{dz} = (\alpha - \eta)\bar{n}. \tag{4.1}$$

The relation between the Townsend and the attachment coefficients and an electric field is calculated using IMONTE gas amplification simulation package. The results are shown in Figure 4.3. This exponential growth is limited by the onset of streamer and the space charge effect, as discussed below.

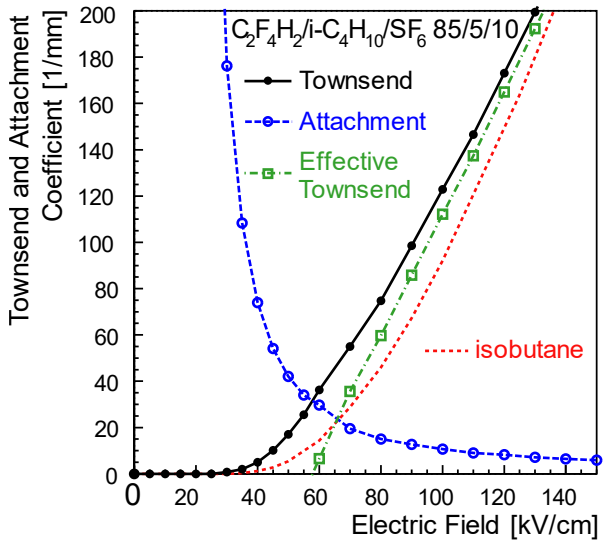

Figure 4.3: An example of calculation of Townsend and attachment coefficients [25] [26] [27].

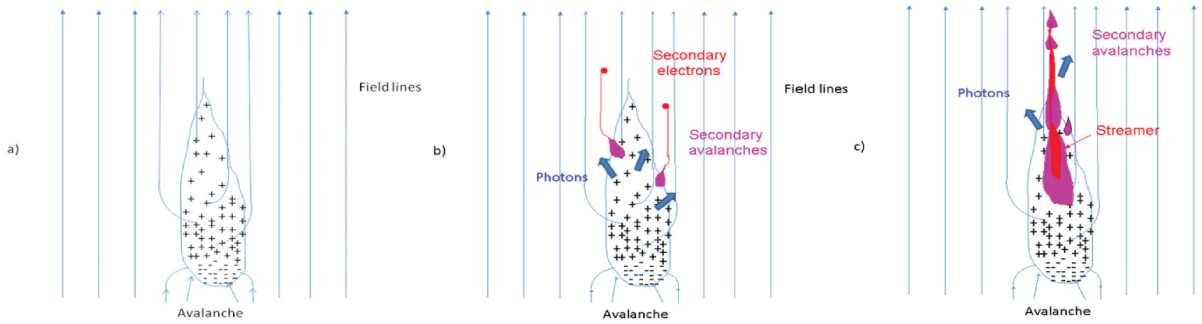

Figure 4.4: Schematic image of streamer development [29]. a) Charge distribution in the gas multiplication stage where a total charge in the avalanche is close to the Raether limit. The electric field is bent toward the primary avalanche. b) Secondary electrons appear near the initial avalanche and travel to the secondary avalanche. c) Secondary avalanches end up with a streamer.

Streamer

At high gas gains, avalanches can be amplified by electrons to streamers. The streamer development process is illustrated in Figure 4.4. The electric field near the initial avalanche bends toward it, and the secondary electrons are generated by ultraviolet photons within the cluster. These electrons move along the electric field, forming secondary avalanches that grow into a streamer. In this case, the number of electrons in the cluster exceeds 10^8. This threshold is known as the Raether limit [28].

Space charge effect

The process of the space charge effect is schematically shown in Figure 4.5. As electrons move toward the anode, the much slower cations drift toward the cathode and linger on it. This creates an opposing electric field E_2 between the electrons and the cations, which reduces the applied electric field E_0. The resulting weakened field decreases the electron amplification. This space charge effect causes amplification saturation just before streamer formation, typically at an amplification factor of 10^7–10^8, enabling operation with fewer streamers. This effect is rarely observed in RPCs with gap sizes of a few millimeters, but becomes significant in RPCs with narrower gaps of a few hundred micrometers.

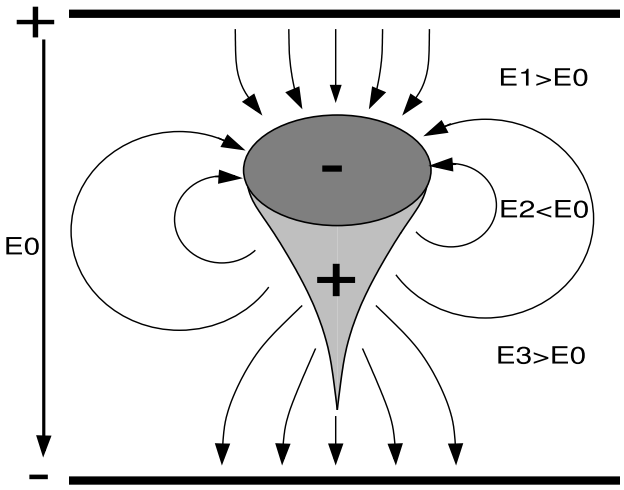

Figure 4.5: A schematic illustration of the space charge effect [27].

4.2.2 The structure of the RPC and the operation

The RPC can be operated in two gas amplification modes:

- Avalanche mode
- Streamer mode.

RPCs were developed in the early 1980s [30] and were initially operated in the streamer mode until the 1990s. In this mode, streamers are intentionally generated in argon (Ar)-based gas, producing ultraviolet photons that result in electron multiplication exceeding 10^8. This leads to its extremely high gas gains, making additional signal amplifiers unnecessary. However, the streamer mode is inferior to the avalanche mode in terms of efficiency and resolution.

In the 1990s, the avalanche mode was introduced for RPC operation. In this mode, Freon (Tetrafluoroethane, $C_2H_2F_4$)-based gas is used to suppress streamers with the addition of isobutane and sulfur hexafluoride (SF_6). Freon and SF_6 stabilize gas amplification due to their high electronegativity. The density of Freon, which is 2.5 times that of Ar, increases ionization, enhancing detection efficiency. The avalanche mode also offers improved timing resolution because electrons move faster compared to the streamer mode. Isobutane acts as a quencher, absorbing ultraviolet photons and further preventing streamer formation.

Gap structure

RPCs are primarily categorized into two types:

- Single-gap RPC in Figure 4.2
- Multi-gap RPC in Figure 4.6.

The single-gap RPC is widely used in high-energy physics experiments due to its simple structure, making it easy to produce. For example, it is used as a trigger detector covering a large area in the ATLAS experiment [31] and the CMS experiment [32]. Its gap size is typically around $2.0\,\mathrm{mm}$, providing detection efficiency of approximately 95 % and timing resolution with a few ns.

The multi-gap RPC consists of alternating layers of high-resistivity materials and gas gaps, typically creating 4 to 10 layers. Each gap size ranges from 200 to 300 $\mu\mathrm{m}$. High voltage is supplied to the outermost layers, resulting in uniform voltage across each gap. For instance, when voltage of $8\,\mathrm{kV}$ is applied to four-gap RDC, that of $2\,\mathrm{kV}$ is applied in each gap. Avalanches occur within each gap, and the induced signals are summed together on readout strips, forming the total signal of the RPC.

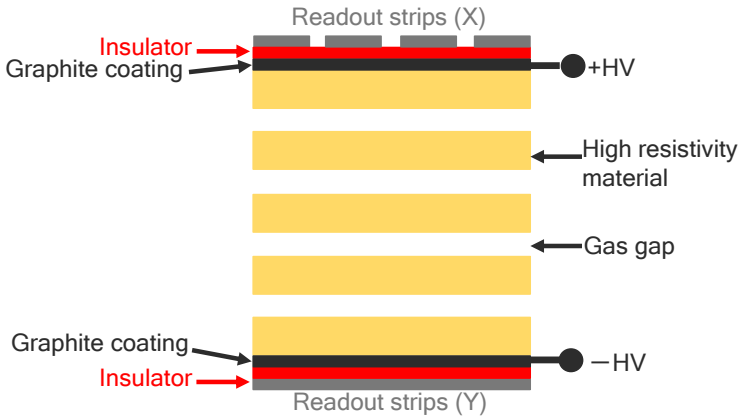

Figure 4.6: A schematic image of a multi-layer RPC detector.

Multi-gap RPCs, also known as "timing RPCs", are used as time-of-flight (TOF) detectors thanks to their excellent timing resolution of less than $100\,\mathrm{ps}$.

4.2.3 Performance of RPCs

Detection efficiency

The detection efficiency of an RPC is determined by its gap size and the number of gaps. A larger gap improves efficiency by allowing a longer drift distance, which facilitates larger gas amplification. Detection efficiencies of 90 to 95 % are achievable with gaps of a few hundred micrometers.

Moreover, multi-gap RPCs enhance efficiency further. The efficiency of an n-layer RPC, ϵ_n, can be approximated with the efficiency of a single layer, ϵ_1, as follows [26].

$$\epsilon_n = 1 - (1 - \epsilon_1)^n \tag{4.2}$$

Timing resolution

The timing resolution of an RPC is improved with smaller gap sizes or an increased number of gaps. The former is attributed to the reduced spread of initial electron generation positions, while the latter is ascribed to a large number of ionizations. To achieve better timing resolution without sacrificing the efficiency, the gap size must be minimized and multiple layers should be stacked to enhance efficiency as described in Eq. 4.2.

Rate capability

The rate capability of RPCs depends on the resistivity of their electrodes. Voltage drops are induced by currents generated from avalanches flowing the electrodes, which reduce the effective electric field in the gap. To improve the rate capability, the electric current must flow quickly to shorten the recovery time of the electric field. This can be realized by using materials with lower resistivity or reducing the distance over which the current must flow, specifically the spacing between the conductors where the high voltage is applied, should be short even though these can give the likelihood of triggering discharges.

The glass-based electrodes of conventional RPCs have a resistivity of $10^{13}\,\Omega\,\mathrm{cm}$, allowing for a rate capability of around $1\,\mathrm{kHz/cm^2}$. By doping the glass with alkaline earth metal oxides, the resistivity can be adjusted to 10^8–$10^9\,\Omega\,\mathrm{cm}$ and improving the rate capability to approximately $100\,\mathrm{kHz/cm^2}$ [33].

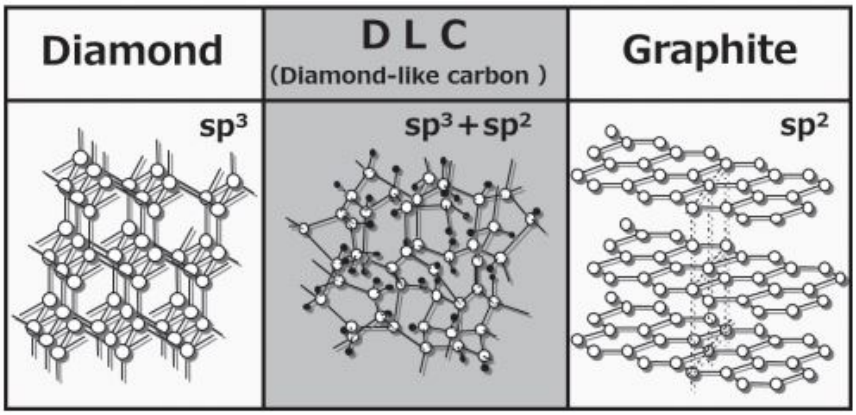

Figure 4.7: Schematic images of the structure of allotropes of carbon [37].

4.3 Developments of the DLC-RPC in past studies

4.3.1 RPC with Diamond-Like Carbon-based electrodes

The RPC with Diamond-Like Carbon (DLC)-based electrodes (DLC-RPC) was developed in the past study [34], where the aim was to increase timing resolution and reduce its material budget.

The schematic image of each allotrope of carbon is shown in Figure 4.7. The structure of DLC is amorphous carbon with sp^2 and sp^3 bonds, each of which corresponds to graphite and diamond structure, respectively. The sp^2 bond provides similar electric conductivity as that for graphite since it contains free electrons. The sp^3 bond renders it as an insulator like a diamond due to the absence of free electrons.

The resistivity of DLC is adjustable from about $10\,\mathrm{k\Omega/sq}$ to $1000\,\mathrm{M\Omega/sq}$ by annealing, changing the thickness, and doping with nitrogen. For example, the resistivity becomes smaller when heat is applied [35], DLC gets thicker [36], and doping nitrogen.

Moreover, thin film DLC can be sputtered on polyimide foils with strong adhesion. Using polyimide foils as insulators and DLC as a high-resistivity material on electrodes, the material budget of RPCs can be much reduced compared to glass or bakelite.

The produced DLC-RPC consists of two parallel DLC-sputtered polyimide electrodes and insulating pillars attached to the DLC to sustain the gap between the two electrodes. The pillars were created by photolithography and made of photoresist.

4.3.2 DLC-RPC for the US-RDC

DLC-RPC is chosen to fulfill the requirements listed in Section 4.1, particularly the requirement on the amount of the material. The development of the DLC-RPC for the US-RDC was started in [5].

Detector design

To realize material budget of less than 0.1 % X_0 for the detector, DLC-sputtered polyimide foils with a thickness of $50\,\mu\mathrm{m}$ are used as high-resistivity electrodes. Thin aluminum films of $100\,\mathrm{nm}$ thick, are used for the readouts. The materials and their material budget are listed in Table 4.1. Up to five polyimide foils, as shown in Figure 4.8 can be stacked without exceeding 0.1 % X_0. The high voltage is applied separately to each of the DLC layers.

In conventional RPCs, nylon fishing lines are typically used to create gaps between electrodes. However, this method is unsuitable for polyimide foils, which are prone to distortion. Therefore,

Table 4.1: Material for the detector and their material mass thickness

Material	Material mass thickness
Polyimide with a 50 µm thickness	0.0175 %X_0
Aluminum with a 30 µm thickness	0.0034 %X_0
Gas in a gap size of 2 cm	0.0034 %X_0

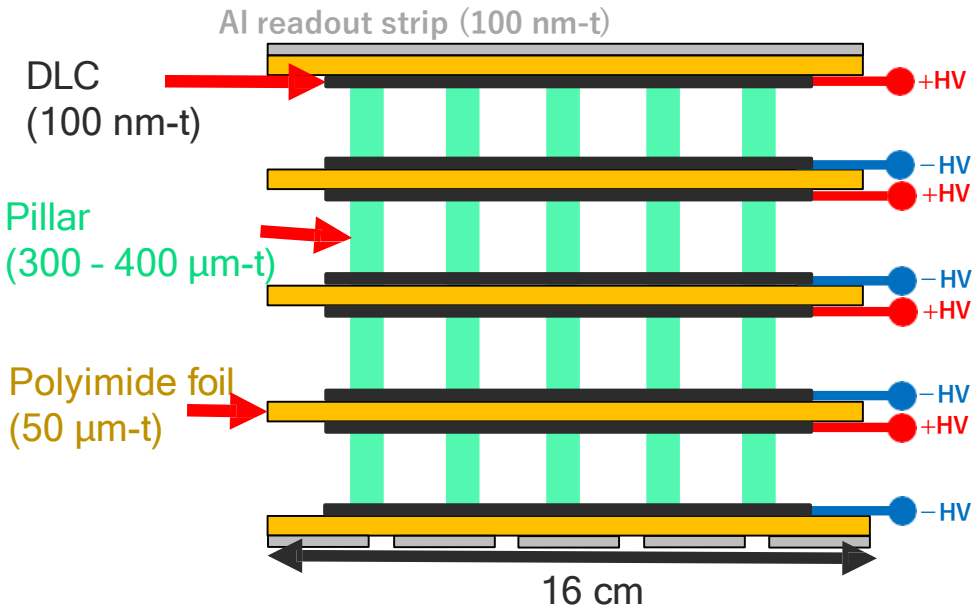

Figure 4.8: A schematic image of the four-layer DLC-RPC for the US-RDC.

as inherited from the study [34], pillars fabricated using photolithography are formed on top of the DLC to maintain the gaps. The pillar formation process is illustrated in Figure 4.9. Each pillar has a thickness of 384 µm, a diameter of approximately 400 µm, and is spaced with a pitch of 2.5 mm, occupying about 2 % of the active region. These pillars, combined with the pressure applied to the electrodes, keep the gap uniform.

Production of prototype electrodes

A small sample electrode with a size of 3 mm × 3 mm, as shown in Figure 4.10, was produced for the 2019 prototype. About 100 nm thick DLC is sputtered on a polyimide foil with a thickness of 50 µm, and then pillars made from photoresist are formed on the DLC. The pillar formation procedure was conducted by Raytech Inc.[*1] [38]. The sputtering procedure of DLC onto Kapton foil manufactured by DuPont [39] was performed by Be-Sputter [40]. The gas mixture used for the DLC-RPC is Freon, SF_6, and isobutane, a flammable gas as a quencher in the ratio 94:1:5.

The 2019 prototype detector achieved performance that satisfies three of the requirements for the US-RDC [5]:

- Material budget: less than 0.1 % X_0
- Detection efficiency: more than 90 % for Minimum Ionizing Particles (MIP), expected with results of a single-layer configuration
- Timing resolution: less than 1 ns.

[*1] The company name was changed to TRENG F Products, Inc. as of the first of July, 2022

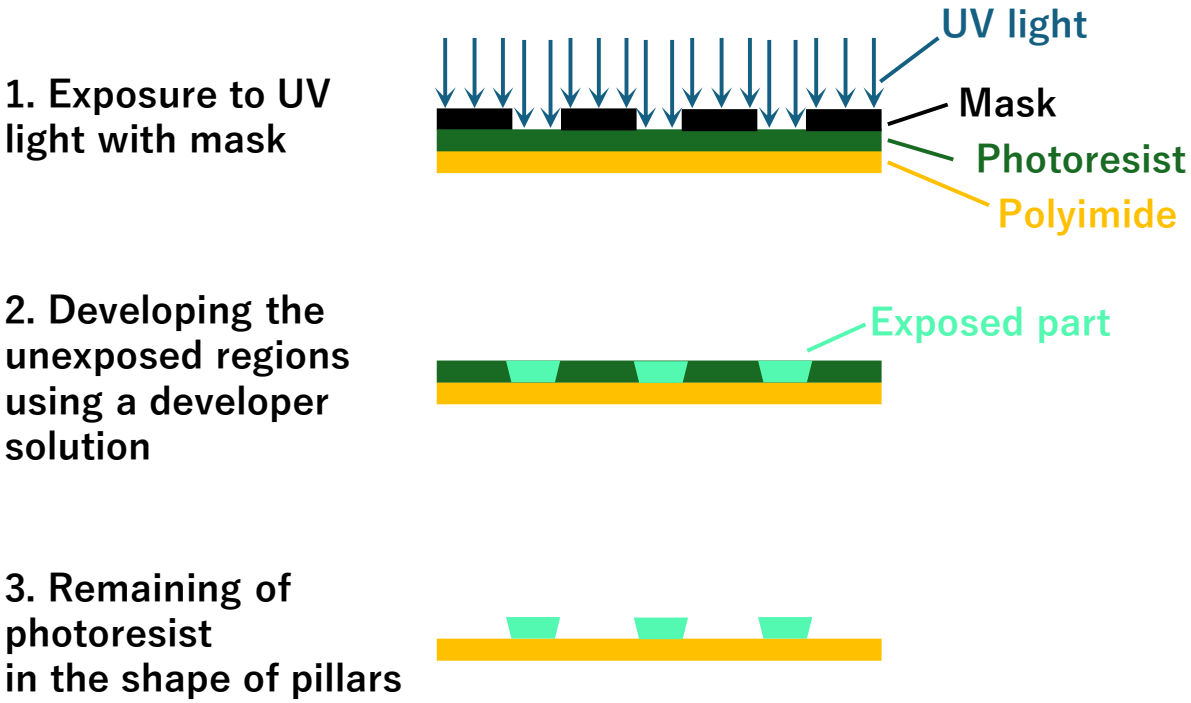

Figure 4.9: A schematic illustration of the pillar formation process. Positive development.

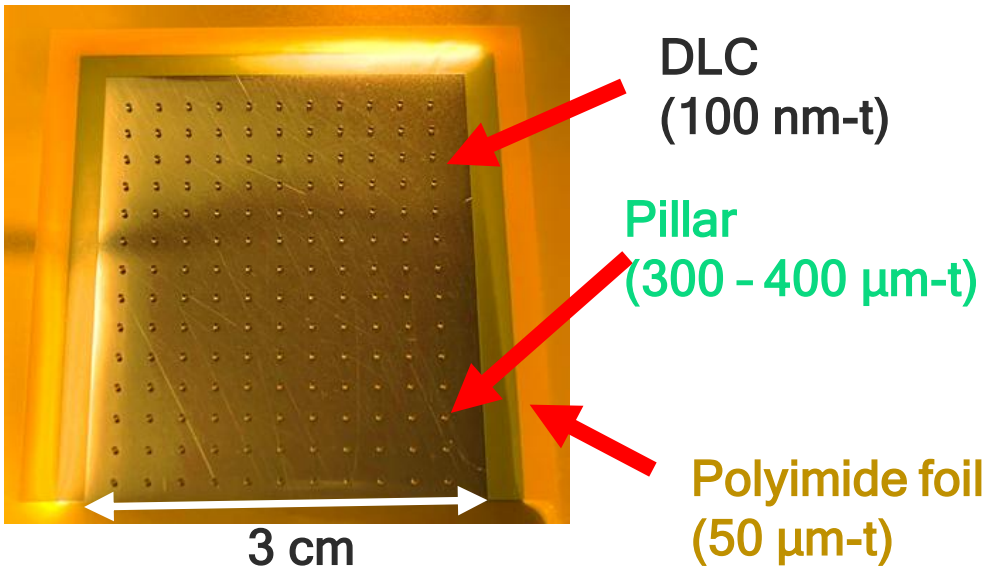

Figure 4.10: A sample of electrodes on the DLC-RPC produced in 2019.

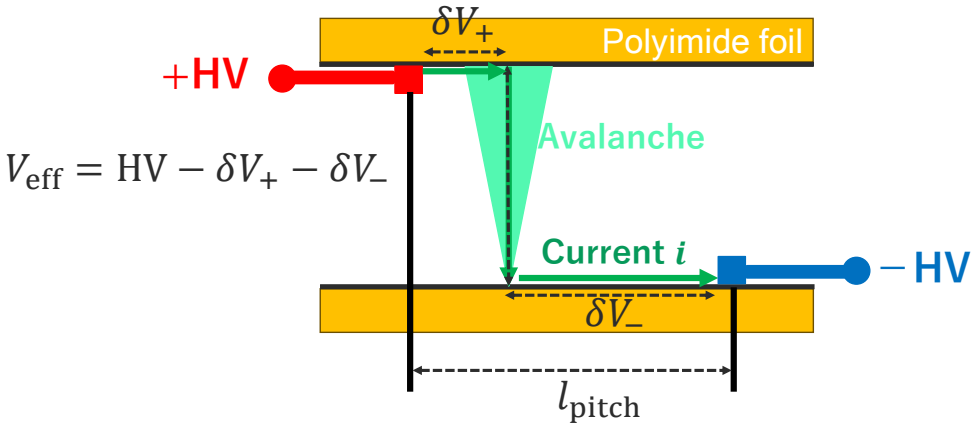

Figure 4.11: A schematic drawing of the voltage drop due to a large current. The voltage drop depends on the distance between the high voltage supply points on the anode and cathode l_{pitch} and surface resistivities. The applied voltage across the gas gap is reduced by the voltage drop.

The performance evaluation had been done using β-rays from ^{90}Sr, with the rate of approximately $20\,\text{kHz/cm}^2$ more than ten times below the required rate of $3\,\text{MHz/cm}^2$.

4.3.3 Rate capability of the DLC-RPC

As discussed in Section 4.2.3, the rate capability of RPCs depends on the resistivity of their electrodes and the spacing between high-voltage supply points. When large electric currents flow through the electrodes, voltage drops are induced in the gap. This results in a decrease in the effective voltage, leading to reduced gas gain, lower detection efficiency, and degraded timing resolution.

To mitigate voltage drops, one potential solution is to reduce the resistivity of the electrodes. However, lowering resistivity increases discharges; achieving an optimal balance between these parameters.

In the case of the DLC-RPC, the high-resistivity material on the electrode is thin, causing the current to flow only on the surface, as illustrated in Figure 4.11. The voltage drop in the DLC-RPC is derived from the equation below [6]:

$$\nabla^2 \delta V(x, y) = q_{\text{mean}}(V_{\text{eff}}) \cdot f(x, y) \cdot \rho_{\text{S}} \tag{4.3}$$

where ∇^2 is the two-dimensional Laplace operator, δV represents the voltage drop, q_{mean} is the average charge from gas amplification caused by muons in the beam, V_{eff} is the effective applied voltage, $f(x, y)$ is the position-dependent muon beam rate, and ρ_{S} is the surface resistivity of the electrode.

4.3.4 Evaluation of rate capability using a high-rate muon beam

In 2020, the performance evaluation tests were conducted at the πE5 beamline at PSI [6]. The tests aimed to investigate the response of the detector to MIP positrons and low-momentum muons, assess the effect of voltage drops, and evaluate how the detection performance for MIP positrons was affected under muon irradiation. The 2019 prototype detector consisting of the electrode shown in Figure 4.10 with a single layer was used in these tests.

Response to MIP positrons

The detector measured MIP positrons from the Michel decay of the muons. Pulse-height spectra for the MIP positrons are shown in Figure 4.12. The MIP positrons entered a trigger counter after passing through the DLC-RPC. Signals were searched for within the time window before the detection time in

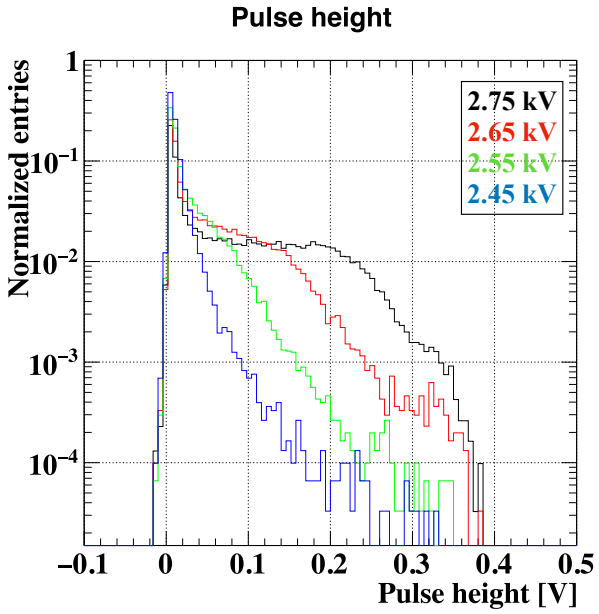

Figure 4.12: Pulse-height spectra for MIP positrons at different voltages [6].

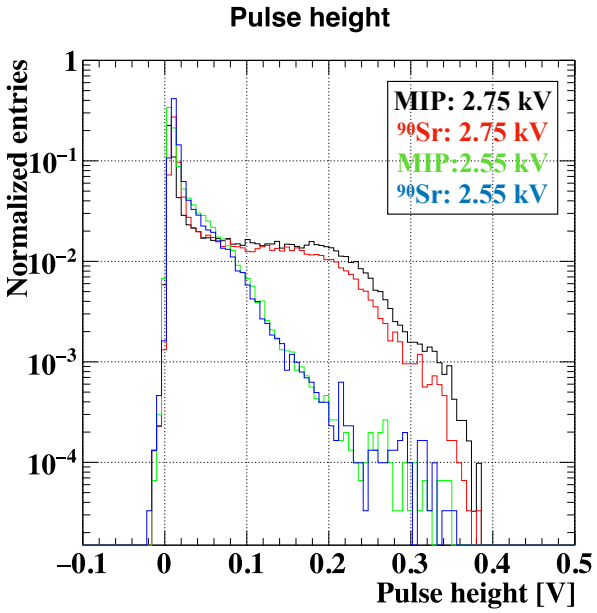

Figure 4.13: Pulse-height spectra for MIP positrons and β-rays [6].

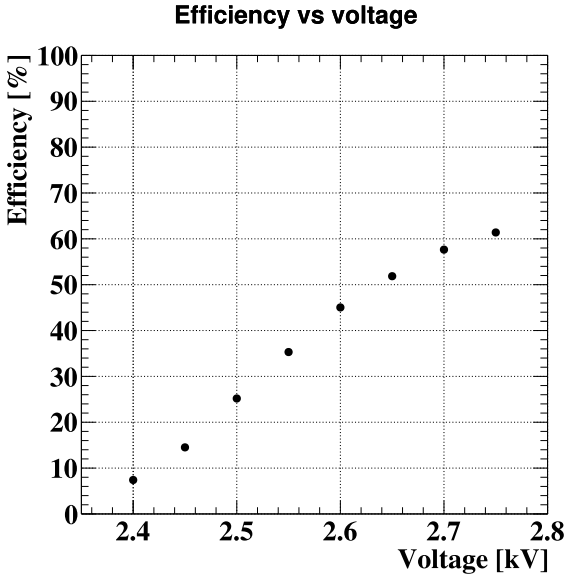

Figure 4.14: Detection efficiency for MIP positrons as a function of the applied high voltage for the 2019 prototype detector [6].

the trigger counter. As the applied voltage increased, the number of signals with higher pulse heights also increased. Before measuring MIP positrons, the detector operation was verified using β-rays from ^{90}Sr. A comparison between spectra of the MIP positrons and the β-rays is shown in Figure 4.13. The detection efficiency, defined as the ratio of signals more than $20\,\mathrm{mV}$ in the total analyzed events, is shown in Figure 4.14. It demonstrates that the detector achieved efficiency above 60 %. The β-ray test revealed no significant differences in the detector response from the test using the decay positrons, confirming that β-rays from ^{90}Sr can be substituted for MIP positrons for performance evaluation.

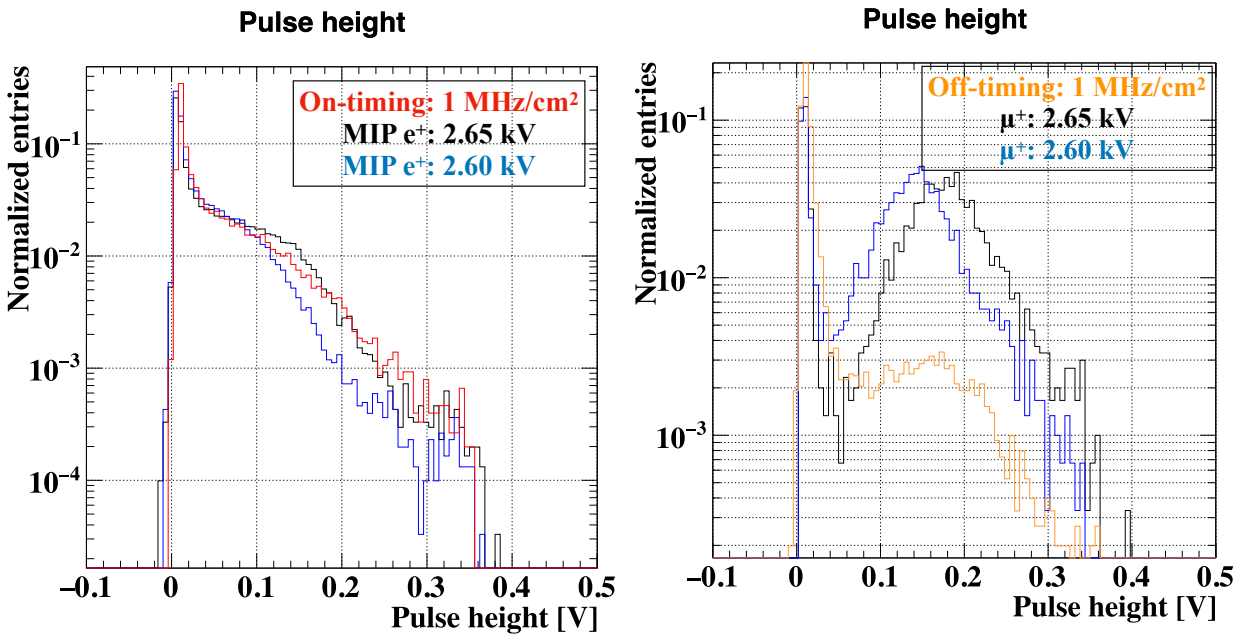

(a) On timing **(b)** Off timing

Figure 4.15: Pulse-height spectra for the muon beam with the beam rate of $1\,\mathrm{MHz/cm^2}$ at the center and for those of MIP positrons and muons [6]. The spectra under the high-rate muon beam were measured at the applied voltage of 2750 V. (a) On timing; the on-timing spectrum is compared with spectra for MIP positrons. (b) Off timing; the off-timing spectrum is compared with spectra for muons.

Response to high-rate muons and the rate capability

The rate capability for the high-rate muon beam was investigated. The magnitude of the voltage drop was estimated by comparing pulse-height spectra for the high-rate muon beam and each pulse-height spectrum of the MIP positrons and muons. The spectra for the muon beam with the beam rate of $1\,\mathrm{MHz/cm^2}$ at the center at the applied voltage of 2750 V and those of MIP positrons and muons are shown in Figure 4.15.

The analysis implied a voltage drop was 100–150 V. Despite the voltage drop, the detection efficiency reached 50 % according to Figure 4.14. Using Equation 4.2, the overall efficiency for a four-layer detector configuration is estimated to be beyond 90 %. This result demonstrates that the 2019 prototype detector possesses a rate capability of $1\,\mathrm{MHz/cm^2}$.

4.3.5 Radiation hardness of the DLC-RPC

As mentioned in Section 4.1, the US-RPC is required to operate for 20 weeks in the MEG II physics run. The irradiation dose Q_{μ^+} by the muon beam in the πE5 beamline is calculated using the beam rate, $3\,\mathrm{MHz/cm^2}$ and the period of 20 weeks. The average charge per avalanche, q_{mean} was estimated as about 3 pC when a voltage drop of 100 V is considered using the muon beam in the πE5 beamline in the study [6]. Therefore,

$$Q_{\mu^+} = 3\,\mathrm{pC} \times 3\,\mathrm{MHz/cm^2} \times 20\ \mathrm{weeks} \sim 109\,\mathrm{C/cm^2}. \tag{4.4}$$

For conventional RPCs, aging from irradiation has been reported in the CBM [41], the CMS [42], and the ALICE experiment [43]. The main effects are deposits on the surface of electrodes and an increase of dark current due to contamination in the gas. In particular, it is considered that

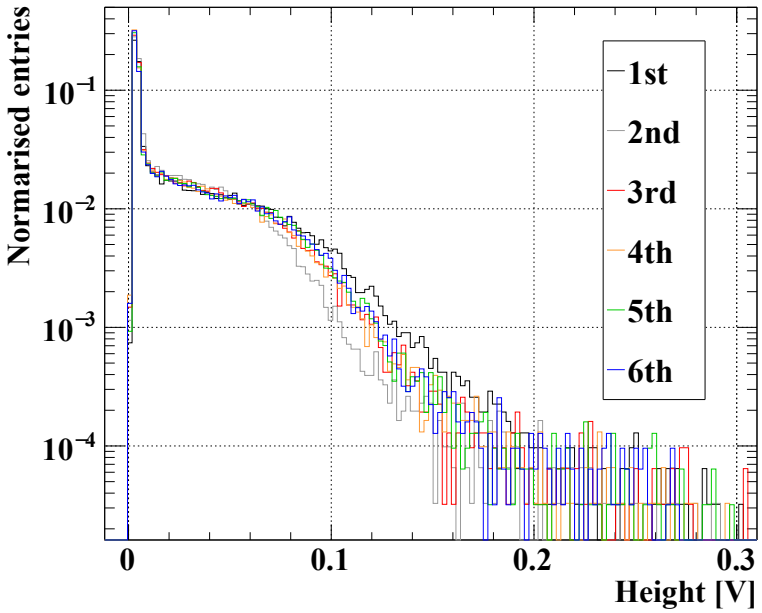

Figure 4.16: Pulse-height spectra for the β rays in intervals of the test [7].

radiation ionizes SF_6 if it is used as a part of gas mixture, causing the creation of fluorine in the gas amplification [7] through Eq. 4.5 and 4.6 [44].

$$SF_6 + e^- \longrightarrow {SF_6}^{-*} \tag{4.5}$$

$${SF_6}^{-*} \longrightarrow {SF_5}^- + F \tag{4.6}$$

Since aging tests on the DLC-RPC had never been carried out before the study [7], the investigation was needed to figure out whether the same phenomena would occur.

4.3.6 Fast neutron irradiation test

In 2022, an aging test on the DLC-RPC was carried out using fast neutrons of the Tandem electrostatic accelerator in Faculty of Maritime Sciences, Kobe university [7].

Response to fast neutrons

The total irradiation dose was $162\,\mathrm{mC/cm^2}$, which is about one-thousandth of the MEG II irradiation dose. The performance evaluation using β-ray from ^{90}Sr was conducted six times in intervals of the test to investigate the change in pulse-height spectra. The pulse-height spectra for β-rays are shown in Figure 4.16. The degradation of its performance was not observed with the irradiation dose.

The results of an analysis of the elemental composition on the electrode surface using X-ray Photoelectron Spectroscopy (XPS) are shown in Table 4.2, indicating that fluorine compounds were formed in the active region. The details of the XPS instruments used for the test are explained in Section 5.2.2.

Table 4.2: The elemental composition of each position on the electrode used in the fast-neutron irradiation test in 2022 [7].

Position	C1s [%]	N1s [%]	O1s [%]	F1s [%]	Si2p [%]
(Non-irradiated area)	79.03	3.19	17.78	-	-
(Neutron-irradiated area on the active region)	76.06	-	15.22	7.37	1.35
(Neutron-irradiated area on the inactive region)	72.82	3.02	19.72	1.53	2.91

4.3.7 X-ray irradiation test in 2022

An aging test with X-rays was also conducted using facilities provided by the Platform-C, [*2] KEK in Tsukuba after the fast neutron irradiation [7]. The detail of the X-ray generator at the Platform-C is given in Section 5.1.

Response to X-rays

The irradiation dose during this test reached $272\,\mathrm{mC/cm^2}$. The comparison between each pulse-height spectrum for the β-ray before and after the aging test at KEK is shown in Figure 4.17. The performance deterioration was not observed after the ionization dose either. A decrease in the detector current was observed during the irradiation. However, this decrease was considered due to gas gain degradation, however, it could not be distinguished from fluctuations in the X-ray intensity, as the intensity was unknown.

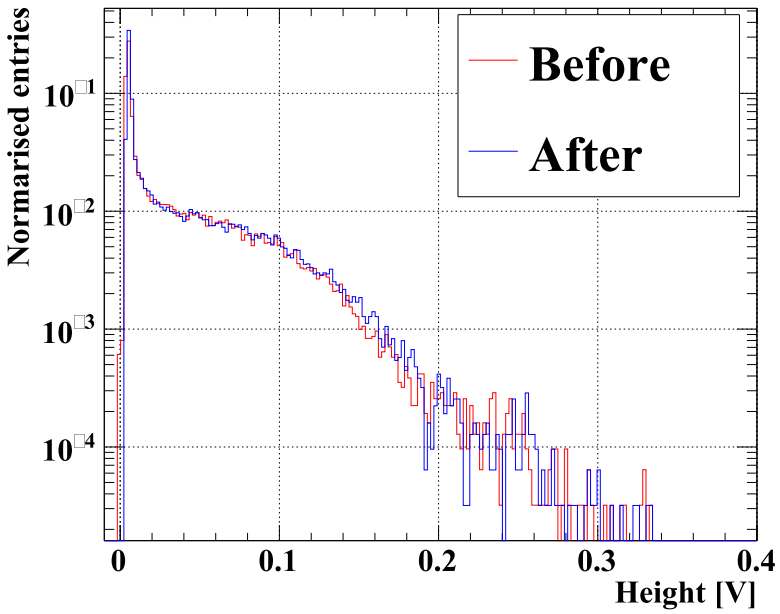

Figure 4.17: Pulse-height spectra before and after the X-ray irradiation test [7].

Investigation on deposits on the surface was also conducted after this test. The results are shown in Table 4.3, showing Fluorine was also created by the ionization dose.

[*2] The Platform-C is a consortium for developing semiconductor detectors and organized at the the Instrumentation Technology Development Center at KEK.

Table 4.3: The elemental composition of each position on the electrode used in the X-ray irradiation test in 2022 [7].

Position	C1s [%]	N1s [%]	O1s [%]	F1s [%]	Si2p [%]
(Non-irradiated area)	79.03	3.19	17.78	-	-
(Discharge point on the anode)	67.63	-	15.22	14.51	2.35

4.3.8 Designing the 2022 prototype for high-rate capability

Electrode design for the 2022 prototype

The optimization of electrode structure to improve their rate capability has been investigated [6] [7]. As discussed in Section 4.3.4, a voltage drop of about 100 V is acceptable for achieving efficiency exceeding 90 % with four layers.

To limit the magnitude of the voltage drop δV, the pitch of the high voltage supply conductors l_{pitch} should be reduced such that δV would be around 100 V assuming the surface resistivity of about $10\,\mathrm{M\Omega/sq}$. This configuration gives that $l_{\text{pitch}} \sim 1\,\mathrm{cm}$; this can be achieved by repeating the alternating conductive strip structure, allowing for the detector to be scaled up to a size $16\,\mathrm{cm}\phi$. A schematic view of the conductive strips for high-voltage supply on the electrode is shown in Figure 4.18. The high-voltage supply conductors are strip-shaped to maintain the constant l_{pitch} of $1\,\mathrm{cm}$, enabling the enlargement of the detector.

For the conductive strip materials, chromium (Cr) was selected for its adhesion to DLC. Copper (Cu) is also used for its good conductivity. Cr is sputtered onto the DLC layer, and then Cu is also sputtered onto the layer Cr in the shape of a strip. Besides, to prevent discharges near the strips, the protective covers made of photoresist are overlaid, as shown in Figure 4.19. The width of the conductive strip was set to $50\,\mu\mathrm{m}$, and the protective cover with the width of $200\,\mu\mathrm{m}$, is chosen to minimize the inactive region. These parameters of the strips need to be tested.

The fabrication procedure for the 2022 prototype production [7] is outlined below:

- Sputter DLC onto a polyimide foil with a thickness of $50\,\mu\mathrm{m}$
- Attach conductive strips by sputtering Cr onto the DLC and Cu onto the Cr
- Overlay protective covers at the boundary between the DLC, polyimide, and conductive strips
- Create pillars on the DLC.

A schematic representation of the procedure is shown in Figure 4.20.

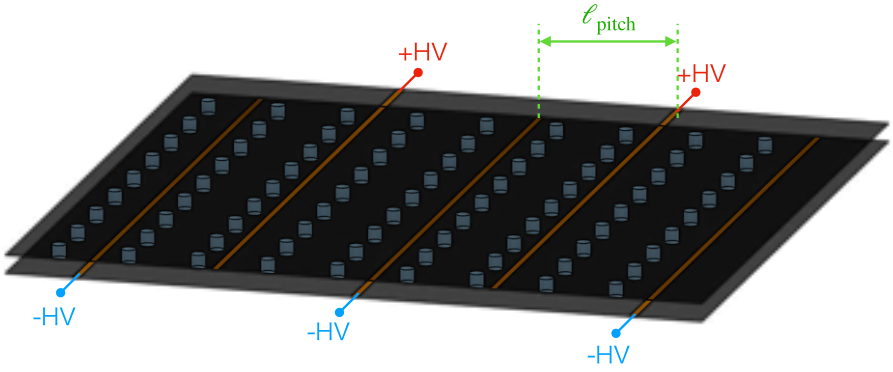

Figure 4.18: A schematic view of strip-shaped high voltage supply [6].

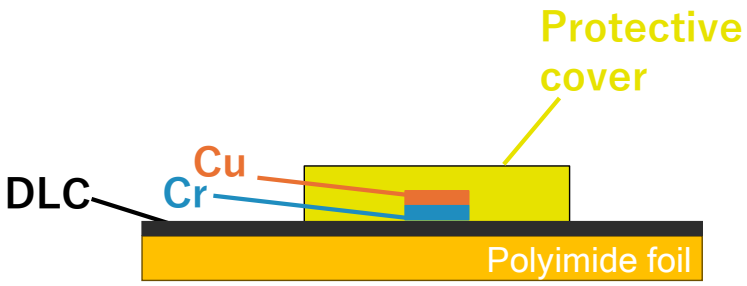

Figure 4.19: A cross-sectional view of the conductive strip and protective cover.

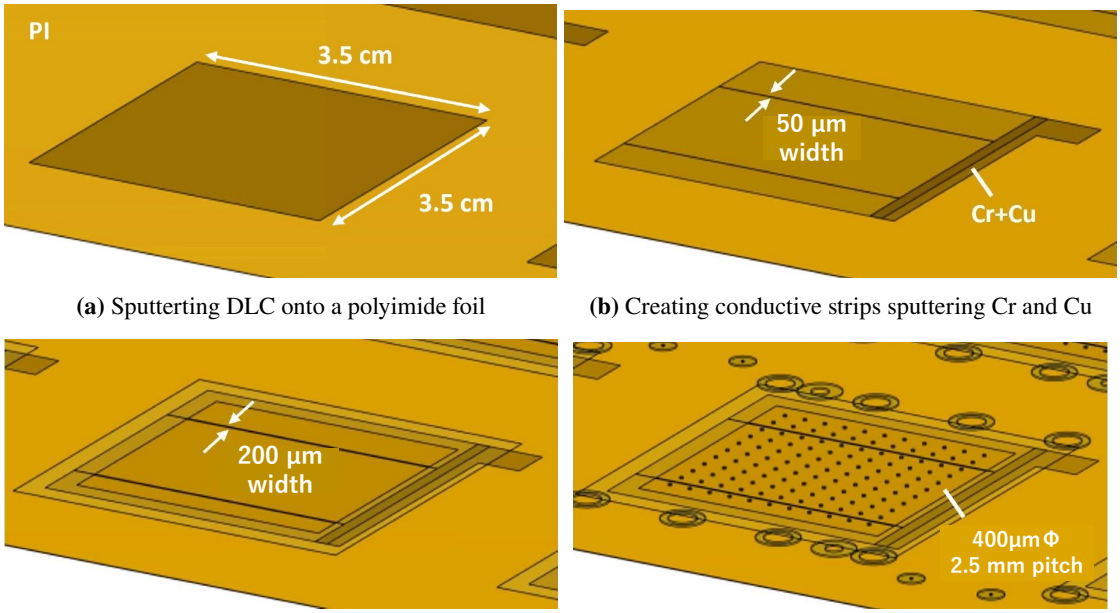

(a) Sputtering DLC onto a polyimide foil

(b) Creating conductive strips sputtering Cr and Cu

(c) Overlaying the protective covers

(d) Attaching pillars onto the DLC

Figure 4.20: The processes of the electrode production. Modified [7].

Issues in the production

However, unlike the electrode of the 2019 prototype, pillars with a thickness of only about 160 µm were fabricated. The dryresist material, Pyralux from DuPont [39] had been discontinued, necessitating the selection of an alternative material. Although a different type of solder resist was chosen, pillars with a thickness of exceeding 300 µm could not be formed.

In addition, as shown in Figure 4.21, slanted pillars were formed due to the excessive development. Figure 4.23 shows how the pillar was distorted compared to a cylindrical pillar on a 2019 prototype electrode, as shown in Figure 4.22. The variation in pillar thickness was approximately 20 µm. As discussed in the next, this led to non-uniform gaps, resulting in unstable operation.

4.3.9 Performance of the 2022 prototype

An electrode sample of the 2022 prototype was fabricated [7], shown in Figure 4.24. A gas gap of 300–400 µm is required to achieve sufficient detection efficiency. To address this requirement, the lower pillars in the 2022 prototype were faced each other and aligned precisely with alignment pins, ensuring the gas gap size, as shown in Figure 4.25.

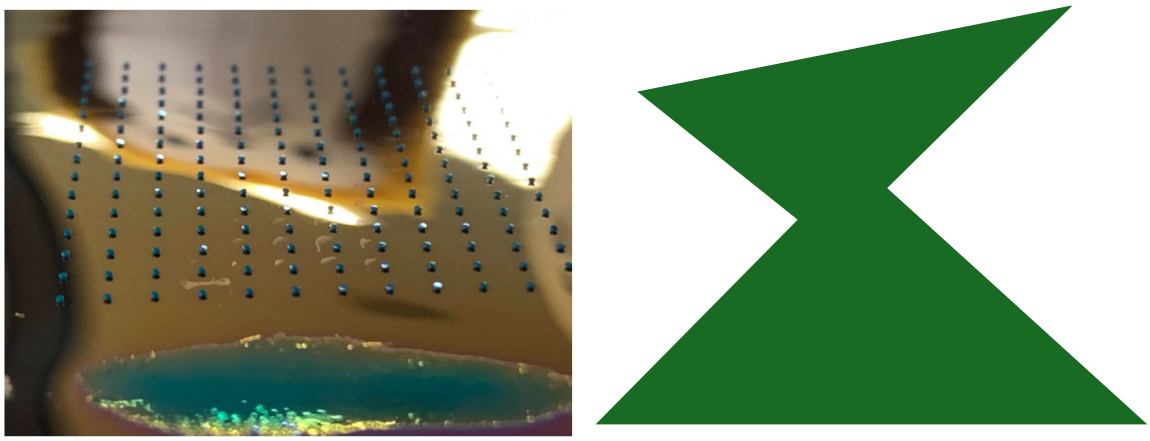

(a) Light is reflected on the slanted top surface. **(b)** Shape of the slanted pillar. The sides became narrower.

Figure 4.21: Slanted pillars

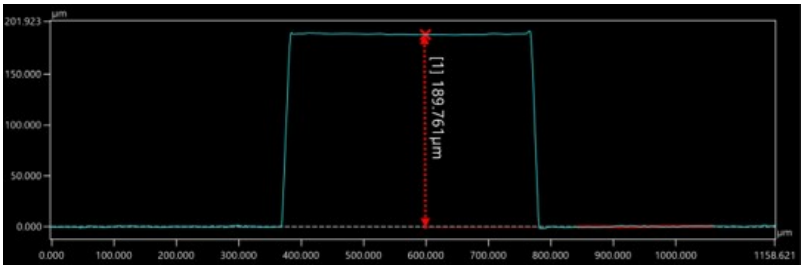

Figure 4.22: Shape of a cylindrical pillar using the same material as a pillar on a 2019 prototype electrode.

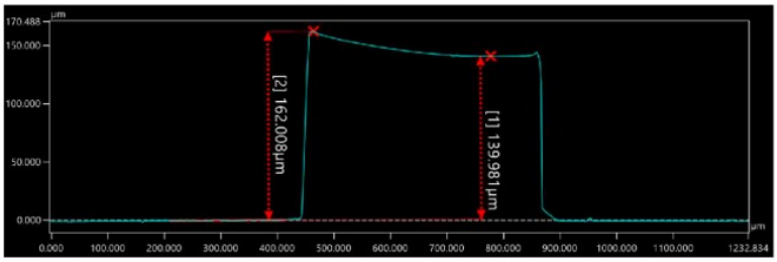

Figure 4.23: Shape of a distorted pillar measured by a laser microscope.

The 2022 prototype, assembled in a frame with a diameter of $29.8\,\mathrm{cm}$, [*3] is shown in Figure 4.26. The module consisted of five stacked electrodes, forming four layers. High-voltage (HV) lines and signal readouts were routed through the inside of the multi-layer substrate from the edges of the module.

The operation of the 2022 prototype was hindered by discharges. Facing distorted pillars made non-uniform gaps. This may have distorted the electric field. Localized enhancement of the electric field can lead to larger avalanches, which may trigger discharges and induce breakdown. Facing distorted pillars made non-uniform gaps, distorting the electric field. Therefore, the distorted electric field prevented the 2022 prototype from operating.

Additionally, discharges along the conductive strips were observed. Those discharges could be caused by the insufficient quenching capability of the protective covers. Discharges can happen from

[*3] As of 2022, the detector size had not been fully optimized and was considered to be larger than in 2024.

the edge of the cover since avalanches do not occur above the covers due to the absence of an electric field. As the width of the cover decreases, the resistance of the current path also decreases, allowing larger currents to flow. Consequently, narrow covers can lead to shorter current paths, increasing the risk of fatal discharges. Figure 4.27 shows a discharge mark on a cover. The damage was severe enough to cause the cover to detach, allowing the breakdown.

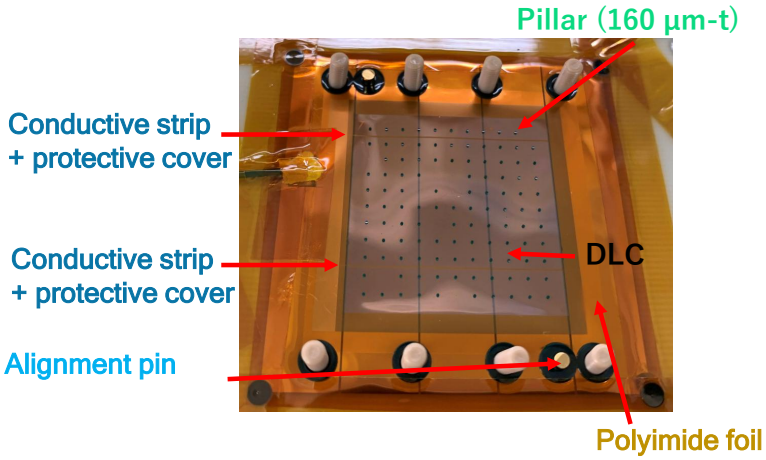

Figure 4.24: A sample of the electrodes fabricated in 2022.

4.3.10 Summary of previous studies

Designing and verification of the performance were carried out with the 2019 prototype and demonstrated that the DLC-RPC could meet three of the six requirements for the US-RDC [5].

- Material budget: less than 0.1 % X_0
- Detection efficiency: more than 90 % for Minimum Ionizing Particles (MIP), expected with results of a single-layer configuration
- Timing resolution: less than 1 ns.

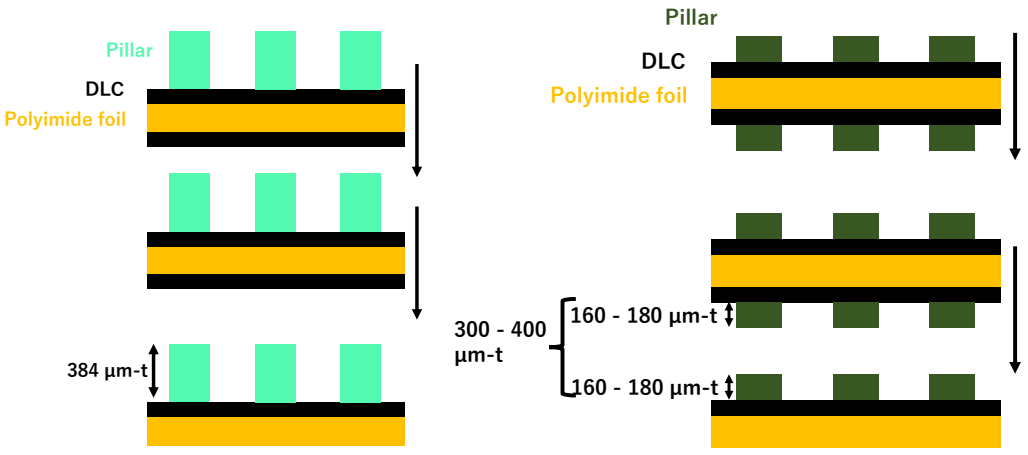

(a) Stacking with high pillars. **(b)** Stacking electrodes with low pillars in 2022.

Figure 4.25: Schematic drawings of electrode structures between high pillar and low pillar schemes.

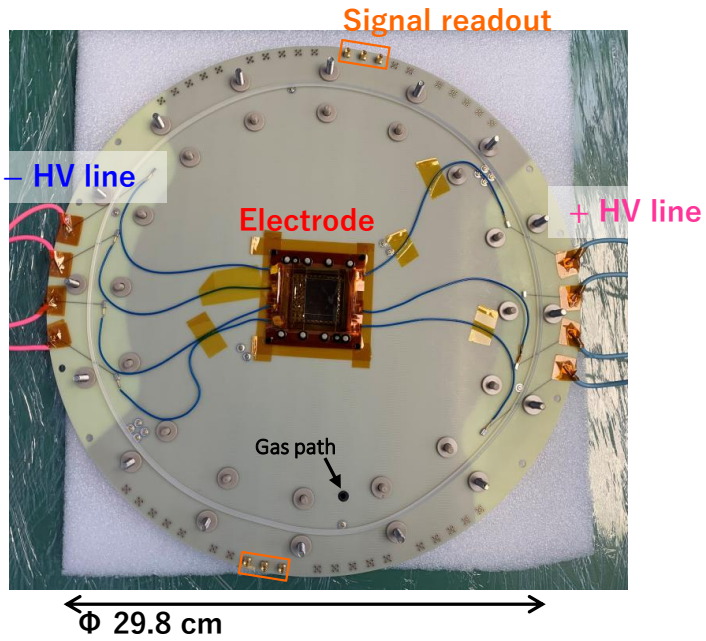

Figure 4.26: The 2022 prototype.The frame, readouts and HV lines were designed to verify the structure for a fullscale detector.

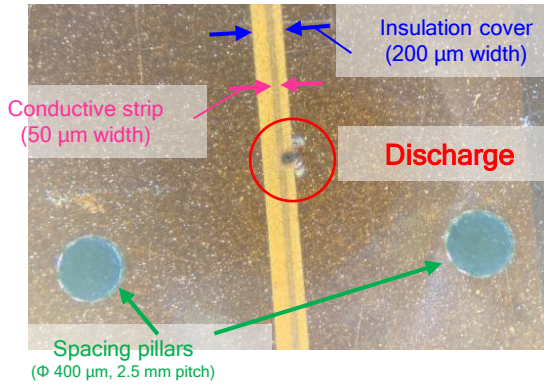

Figure 4.27: Defects of the protective cover due to a discharge.

The evaluation of the rate capability was conducted in 2020 [6]. The electrode to improve the rate capability was designed.

Investigations on the radiation hardness using both fast neutrons and X-rays were carried out with the 2019 prototype in 2022 [7]. However, the effect of aging was not observed due to the limited irradiation dose.

The production of the 2022 prototype and its test on the 2022 prototype were conducted [7]. The distorted electric field induced discharges on the electrode and prevented the operation.

4.4 Aims in this study

Since changes in the performance were not observed with the irradiation dose in the two aging tests conducted in 2022, an additional aging test is required. In particular, the X-ray intensity was unknown, making it impossible to determine the cause of the current decrease during the X-ray irradiation test. Therefore, monitoring the X-ray intensity is necessary for clarification. Additionally, the X-ray profile was unknown, making the estimation of the irradiation dose imprecise. The first aim of this study is to solve these problems. For that, a new aging test with X-rays was taken place in 2023, described in Chapter 5.

A new set of DLC-RPC prototypes should be made with solid pillar structure. The second aim is to produce improved electrodes for stable operation. In addition, the protective cover for the HV conductive strip is to be optimized. The third aim is to implement covers with various widths to the improved electrodes to find out the condition making the detector operation stable. A new fabrication of the electrodes using a new solder resist material was carried out in 2023-2024. The test result of the 2023 and 2024 electrodes is described in Chapter 6.

Chapter 5

Aging test of the DLC-RPC

As discussed in Section 4.3.5, the US-RDC is required to operate for 20 weeks during the MEG II physics run, with an expected irradiation dose of $109\,\mathrm{C/cm^2}$. To evaluate the radiation hardness of the DLC-RPC, two studies were conducted in 2022, as detailed in Section 4.3.6 and 4.3.7. No performance degradations were observed in either study within a limited amount of irradiation dose accumulated in one week. Following the 2022 aging test at KEK (described in Section 4.3.7), an additional aging test was carried out in the same facility using the same X-ray generator for two weeks in 2023. The X-ray intensity and its profile in the 2022 study were unknown, leading to difficulties in distinguishing the causes of the current decrease and estimating the precise irradiation dose. To solve these issues, an ionization chamber (IC) was developed as an X-ray intensity monitoring device. The measurement of the X-ray profile was also taken place to calculate the irradiation dose precisely.

5.1 Experimental setups

X-ray generator at the Platform-C, KEK

The X-ray generator, SA-HFM3 3 kW XG, manufactured by RIGAKU [45], was used for the aging test. Its specifications are listed in Table 5.1. The X-ray is generated by the collision of accelerated electrons with a target. In the X-ray generator, electrons (tube current) are accelerated by the applied voltage (Tube voltage) between the anode and cathode. Generally, the X-ray intensity is proportional to the tube current. During the aging test, the tube current was set to $30\,\mathrm{mA}$, and the tube voltage was set to $50\,\mathrm{kV}$. The characteristic X-ray of copper, whose energy is $8\,\mathrm{keV}$, was available through a $1\,\mathrm{cm}\phi$ collimator after filtering through a monochromator.

The setup for the DLC-RPC in the gas package is shown in Figure 5.2. A 2019 prototype electrode is used as the anode connected to positive high voltage. The grounded cathode made of a DLC-sputtered polyimide foil is stretched on the gas package window. The gas flows through the gas package.

Measurements using β-rays from ^{90}Sr are performed for verification of the operation both before and after the aging test. The β-rays, whose intensity is equal to or larger than the high-rate muon beam, irradiated a part of the active region. The induced signal of the DLC-RPC was sent to the waveform digitizer (DRS4 [22]) through a Al readout strip with a size of $10\,\mathrm{mm} \times 40\,\mathrm{mm}$. The waveform analysis is done by searching the detector signal with information of a hit in the trigger counter made of a scintillator with a thickness of $5\,\mathrm{mm}$ and an MPPC. The detection efficiency is defined as the ratio of signals more than $20\,\mathrm{mV}$ in the total analyzed events, with $20\,\mathrm{mV}$ set as the

Table 5.1: Specification of the X-ray generator used in this irradiation test

Target	Copper
Tube voltage	20–60 kV
Tube current	2–30 mA

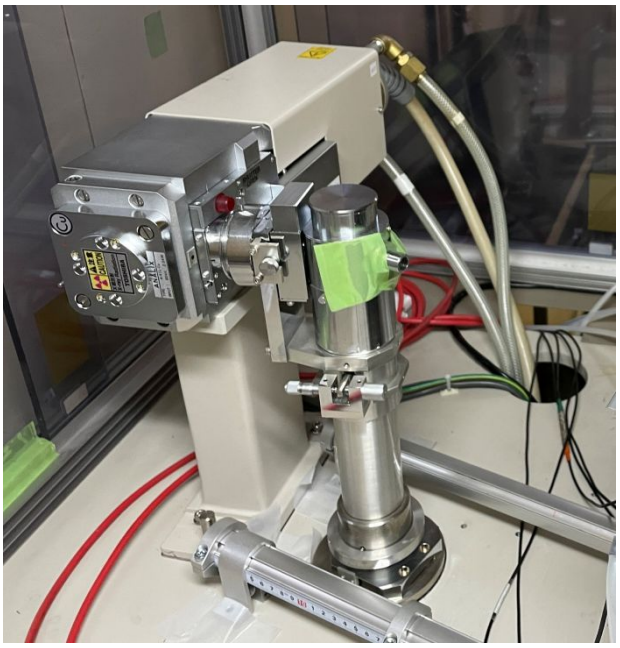

Figure 5.1: X-ray generator at the Platform C, KEK.

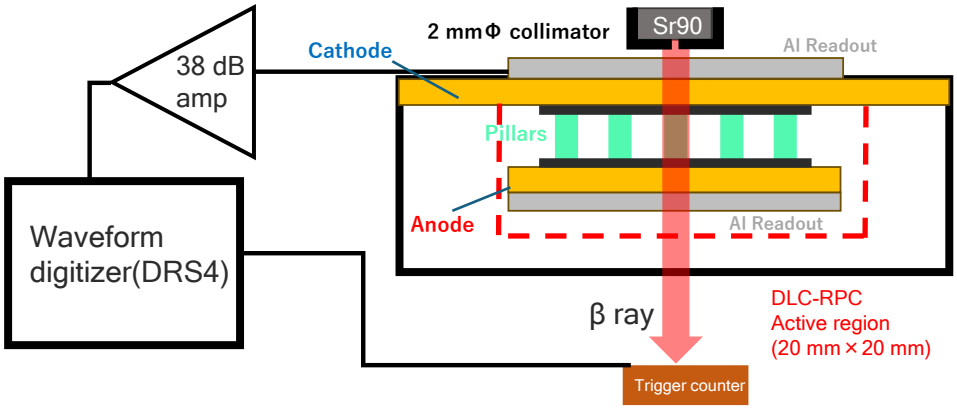

Figure 5.2: A schematic view of a setup for the measurements using β-rays.

analysis threshold, as signals below this level are regarded as noise.

The experimental setup during the X-ray irradiation is shown in Figure 5.3. The active region of the detector was positioned as close as possible to the irradiation hole of the X-ray generator in order to increase the dose. The ionization chamber, monitoring the X-ray outputs, was placed behind the DLC-RPC.

Before commencing the aging test, the X-ray intensity was 5.99×10^8 photon/s as measured using the ionization chamber. After the aging test, the X-ray profile shown in Figure 5.4 was also analyzed, revealing that the intensity was localized to an area of $1\,\mathrm{mm} \times 3\,\mathrm{mm}$. The reason why it was much smaller than the collimator aperture is unknown. A possible explanation is given in Appendix A.

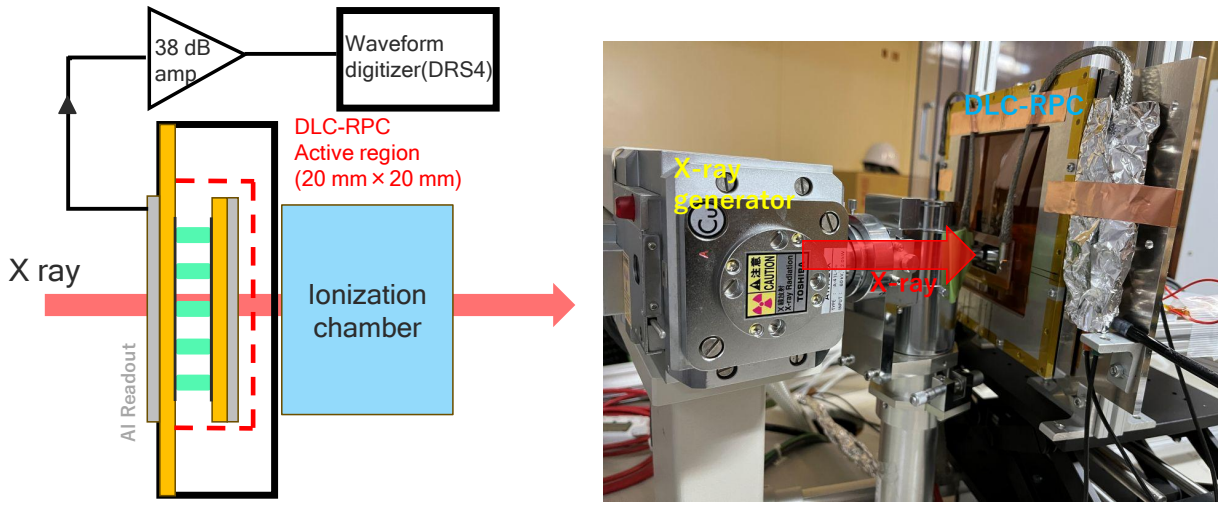

(a) Schematic view of the setup.

(b) Photograph of the setup.

Figure 5.3: Setup for the X-ray irradiation test in 2023.

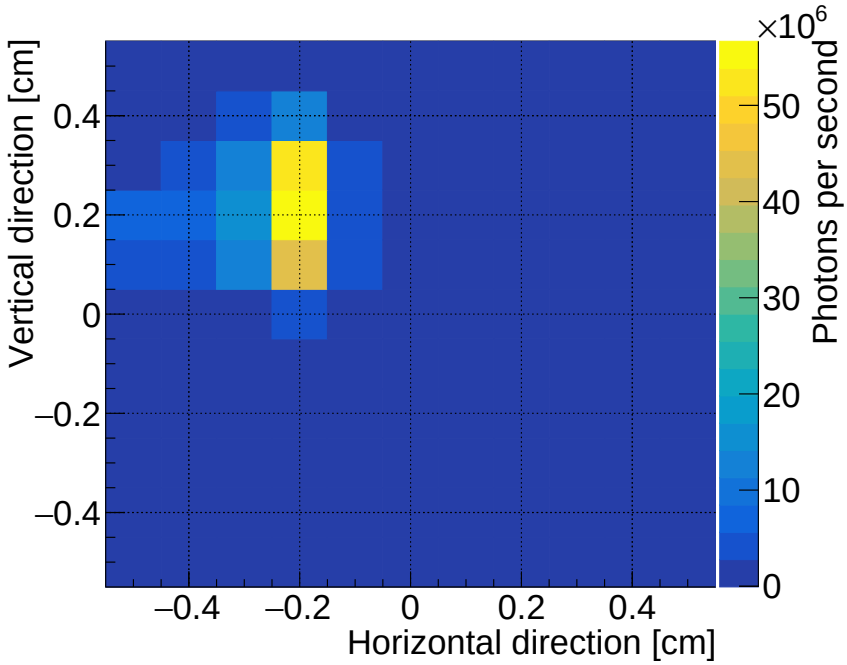

Figure 5.4: X-ray profile measured by the ionization chamber [46].

5.2 Result

5.2.1 X-ray irradiation

The 2019 prototype detector operated at the applied voltage of $2.8\,\mathrm{kV}$ during the aging test. The current history is shown in Figure 5.5. Cleaning and conditioning were carried out during periods when the voltage was not applied. As shown in Figure 5.6, the total irradiation dose reached $54\,\mathrm{C/cm^2}$, which is approximately half of the expected dose in MEG II. The current of the detector gradually decreased during the irradiation, implying that a degradation in gas gain occurred, as the current in the DLC-RPC is proportional to it. The current of the ionization chamber is shown in Figure 5.7. Although a decrease in the IC current was observed, the fraction of the IC current drop was much smaller than that for the RPC current; it was attributed to the baseline reduction when the X-ray was off. Since the ionization chamber showed approximately constant current values, the X-ray output can also be regarded as constant. Therefore, the observed decrease in the DLC-RPC current was primarily attributed to a reduction in gas gain rather than fluctuations in the X-ray intensity.

Figure 5.8 shows the changes in pulse-height spectra for β-rays. Following the X-ray irradiation, the pulse height for β-rays at $2.8\,\mathrm{kV}$ was decreased, corresponding to a performance equivalent to operation at the applied voltage 50–100 V lower than before irradiation.

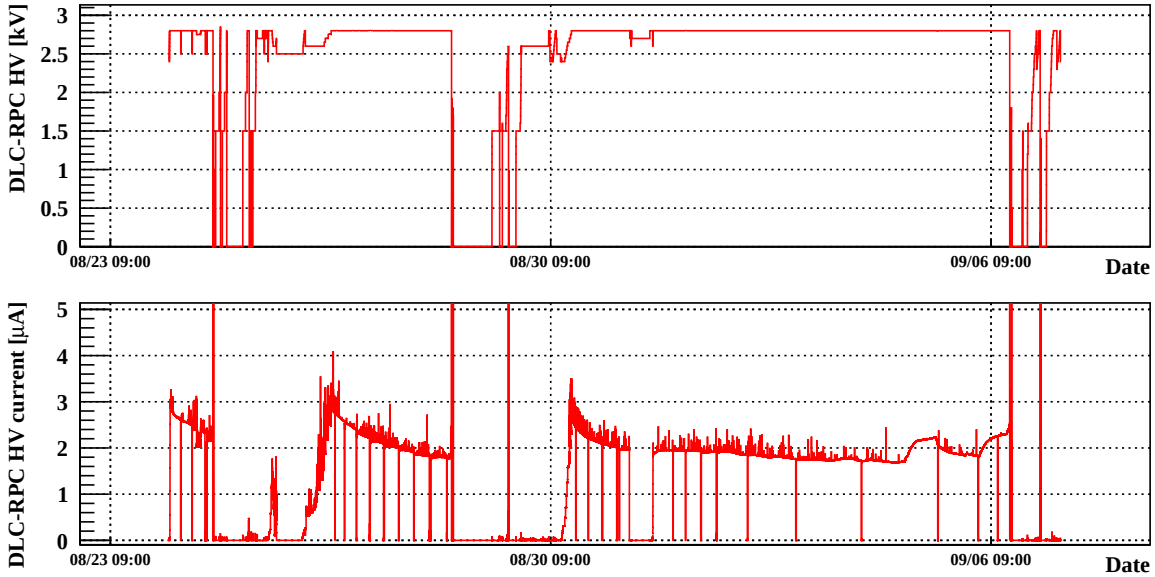

Figure 5.5: Voltage and current histories of the DLC-RPC during the aging test. Horizontal axis: date. The dropped current periods represent recovery phases following discharges that interrupted the operation.

5.2.2 Analysis on the electrode surface by X-ray Photoelectron Spectroscopy

After the X-ray irradiation, deposits were observed on both the anode and cathode, as shown in Figure 5.10 and 5.11. A DLC layer, approximately $2.5 \times 2.5\,\mathrm{mm^2}$ in size, was partially removed from the anode unintentionally when a cleaning procedure was done at the beginning of the second dropped current period. This was likely due to the generated fluorine weakening the bonds of the DLC, leading to its detachment. During the test, the irradiation position was shifted because the irradiated area became inactive. Deposits also formed in this area as shown in Figure 5.10. The resistivity of the DLC

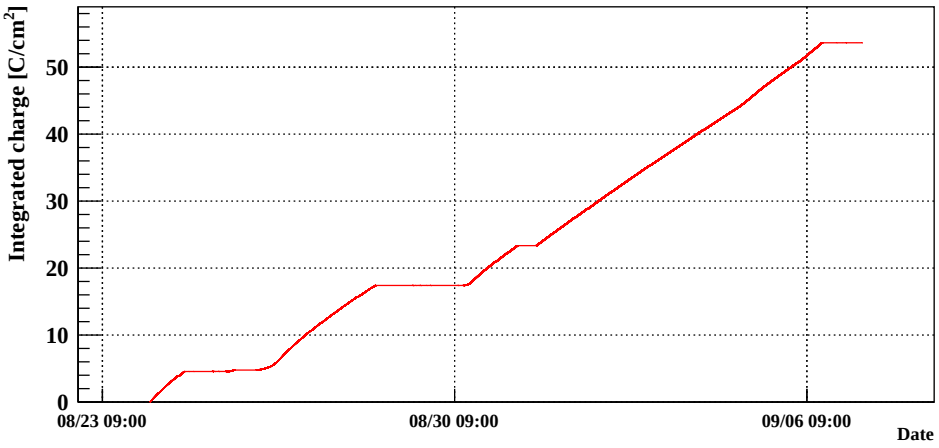

Figure 5.6: Total integrated charge calculated as the product of the current flowing through the DLC-RPC and the time, divided by the irradiation area of $1\,\mathrm{mm} \times 3\,\mathrm{mm}$.

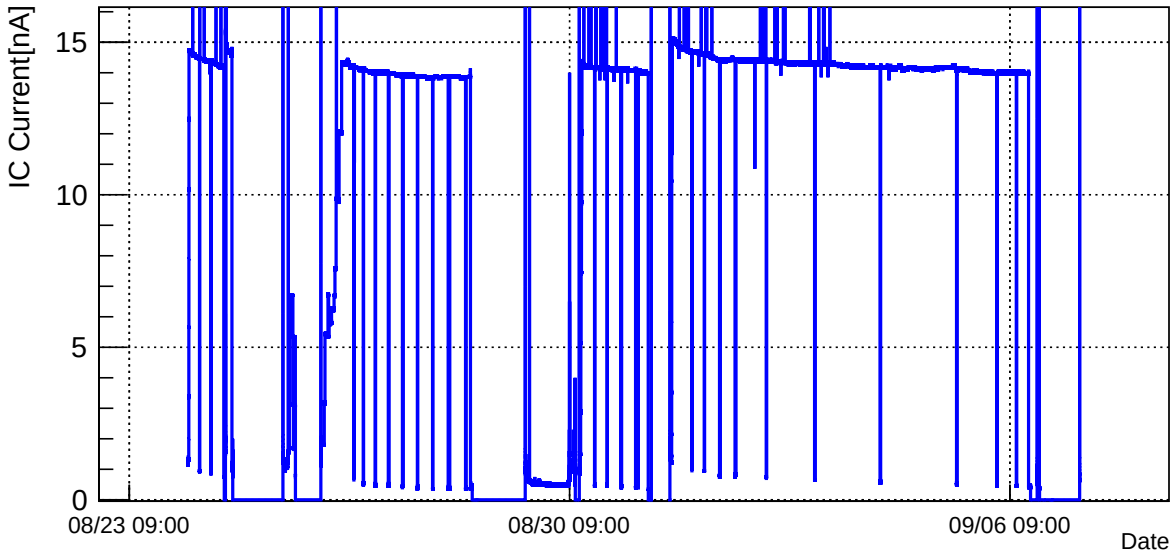

Figure 5.7: Current history of the ionization chamber during the aging test. Horizontal axis: date. When the IC current drops, the X-ray is not output.

on this deposited region was increased from approximately $40\,\mathrm{M\Omega/sq}$ to over $500\,\mathrm{M\Omega/sq}$. However, after cleaning deposits with alcohol, both the resistivity and gas gain recovered.

The elemental composition on the electrode surface was analyzed to investigate deposits, which may be accumulated through the mechanism as described in Section 4.3.5. An investigation using XPS, PHI X-tool produced (ULVAC-PHI, INCORPORATED [47]) was performed.
Measurements were taken at three points, indicated in Figure 5.12 as points 1 (Irradiated area), 2 (Non-irradiated area on the active region), and 3 (Non-irradiated area on the inactive region). The corresponding results are shown in Figure 5.13 and Table 5.2. As observed in past aging tests, fluorine was detected in the active region, particularly at measurement point 1. This suggested a possibility that the chemical reactions described in Eq. 4.5 and 4.6 took place.

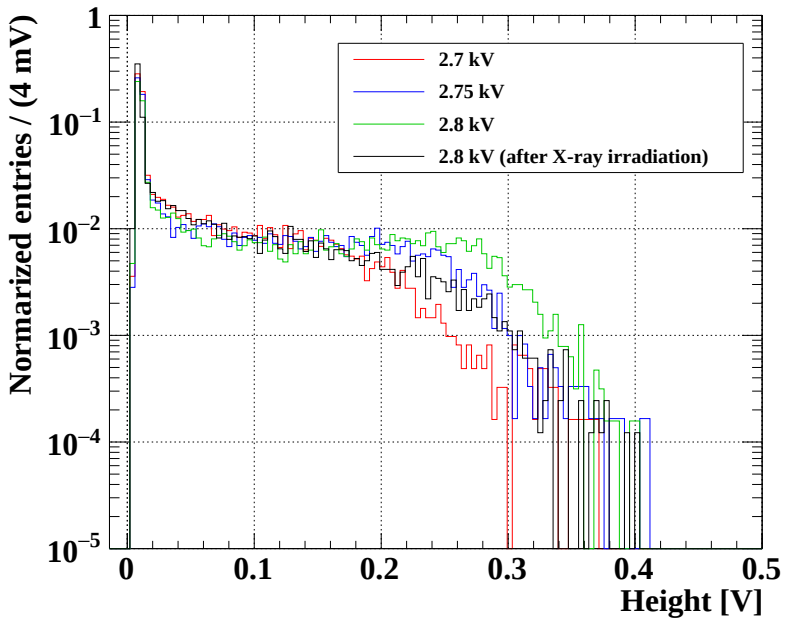

Figure 5.8: Pulse-height spectra for the β-ray [46] before (red, blue, green) and after (black) the X-ray irradiation in different voltages. The black spectrum decreased compared to the green spectrum.

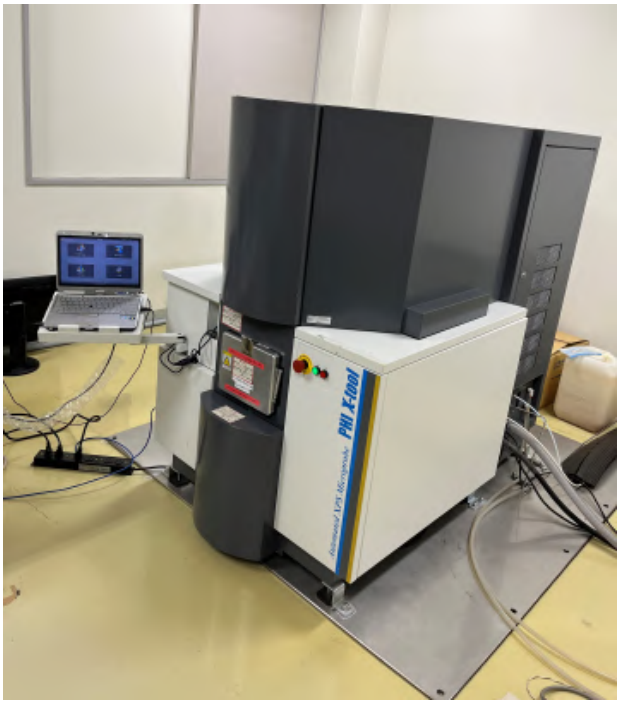

Figure 5.9: XPS, PHI X-tool produced in ULVAC-PHI, INCORPORATED.[47] [7].

Table 5.2: The elemental composition of each position on the electrode used in the aging test in 2023.

Position	C1s [%]	O1s [%]	F1s [%]
1 (Irradiated area)	62.59	11.13	26.28
2 (Non-irradiated area on the active region)	71.70	19.63	8.67
3 (Non-irradiated area on the inactive region)	84.93	15.07	-

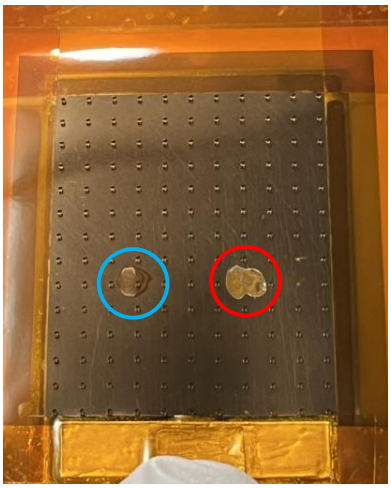

Figure 5.10: Deposits and the discolored DLC.
Red: The first X-ray irradiated point,
Blue: The shifted X-ray irradiated position.

Figure 5.11: A deposit formed in the shifted irradiated position on the cathode. The other deposit in the first position had been removed.

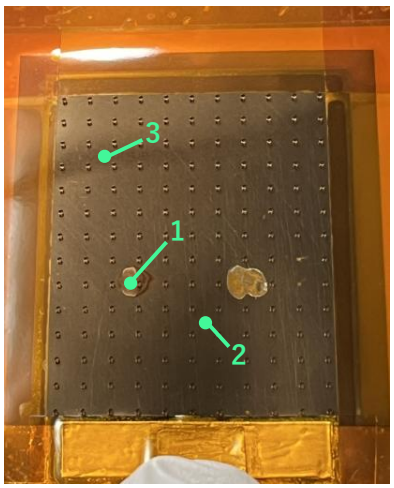

Figure 5.12: Measurement points for XPS. 1: Irradiated area, 2: Non-irradiated area on the active region, 3: Non-irradiated area on the inactive region.

5.3 Summary

The aging test using X-ray was performed in 2023, reaching a total dose of $54\,\mathrm{C/cm^2}$, which is approximately half of the expected dose in MEG II. Gas gain degradation was observed during the irradiation, and fluorine deposits formed on the electrodes, rendering the affected region inactive. To mitigate fluorine formation, faster gas replacement is necessary [41] with optimization of the gas flow structure.

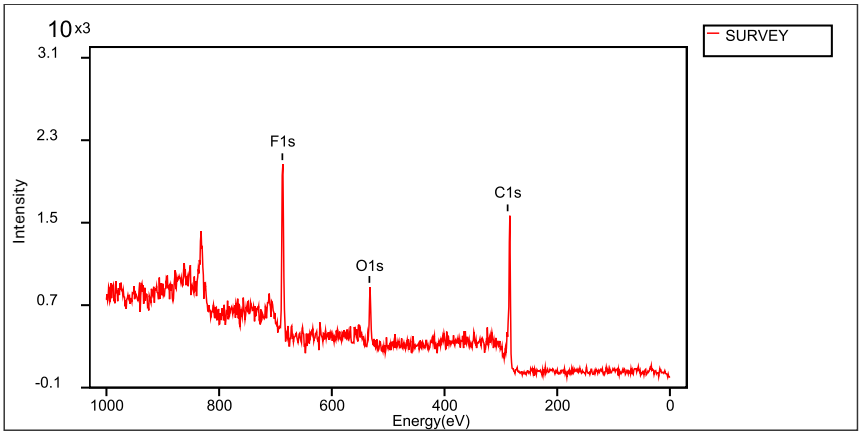

(a) Measurement point 1 (Irradiated area).

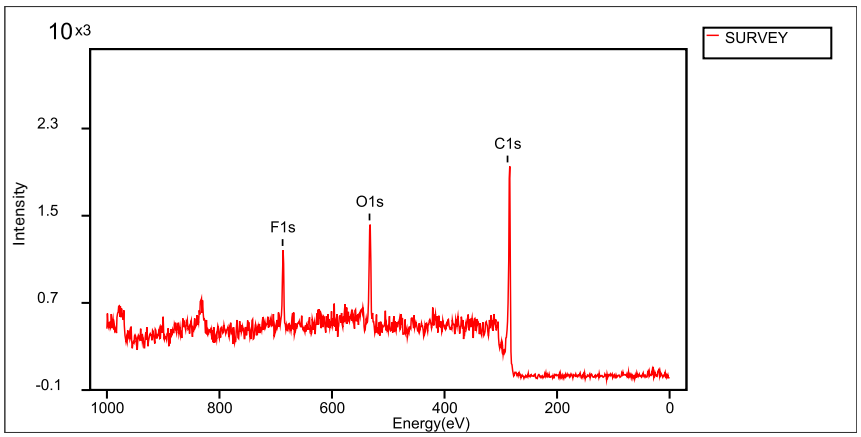

(b) Measurement point 2 (Non-irradiated area on the active region).

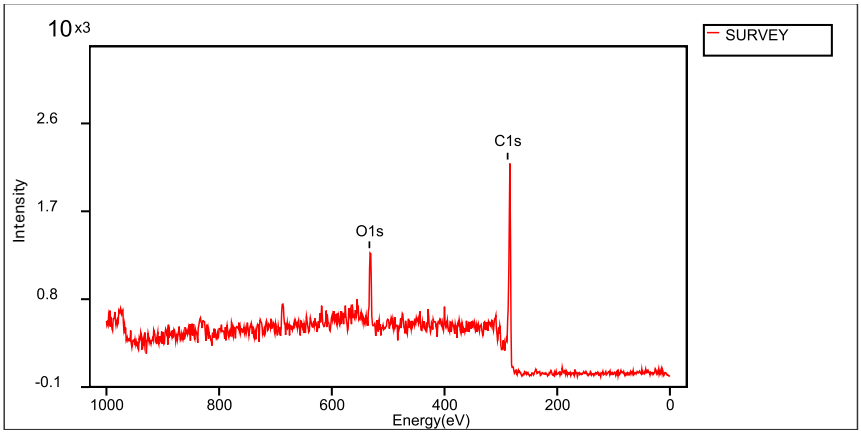

(c) Measurement point 3 (Non-irradiated area on the inactive region).

Figure 5.13: Results of the X-ray photoelectron spectroscopy.

Chapter 6

Improvement of the electrode structure and its performance

6.1 Issues on the 2022 prototype

As discussed in Sections 4.3.8 and 4.3.9, The electrode structure hindered stable operation. This issue was primarily attributed to the quality of the pillars: facing low and distorted pillars led to non-uniform gaps and distorted electric field, increasing the likelihood of discharges.

6.2 Production of new electrodes

6.2.1 2023 electrodes

High pillars with a thickness of above $300\,\mu\mathrm{m}$ were successfully fabricated using a solder resist (Dynamask, Eternal Technology Corporation [48].) by the Micro-Pattern Technology (MPT) workshop at CERN. Processes of pillar formation are shown in Figure 6.1. The pillars on the 2019 prototype electrode were formed by exposing laminated five layers of photoresist to UV lights in one shot, as shown in Figure 6.1a. However, this approach was not feasible, as UV lights cannot penetrate a solder resist with a thickness of above $300\,\mu\mathrm{m}$. To overcome this limitation, exposure and laminating are performed alternately for each layer with a thickness of about $75\,\mu\mathrm{m}$, as shown in Figure 6.1b. Consequently, pillars with a thickness of $330\,\mu\mathrm{m}$–$360\,\mu\mathrm{m}$, depending on diameters were formed.

Figure 6.2 shows the newly produced electrodes with different diameters in 2023. The corresponding thicknesses are listed in Table 6.1. These samples with various diameters were produced to investigate the dependence of the adhesion between the DLC layer and the pillars on the diameter. The thickness tends to be larger with a large diameter. This is because polymerization does not progress efficiently inside during the exposure process as the diameter increases. However, the adhesion to the DLC was not good in $400\,\mu\mathrm{m}\phi$ and $500\,\mu\mathrm{m}\phi$ samples. Pillars were peeled off easily with some force to the side of the samples. For $600\,\mu\mathrm{m}\phi$ samples, on the other hand, the condition was better. In addition, there was an issue with the alignment of pillar layers for every diameter sample, as shown in Figure 6.3 and 6.4. Steps-like structure was seen between the layers. This issue was to be solved for the next production (The 2024 prototype).

The electrodes were stacked originally as illustrated in Figure 4.25a. By attaching pillars to only one side of the electrode, direct pillar-to-pillar contact was eliminated. Furthermore, the thickness variation was significantly improved. It was reduced to less than $10\,\mu\mathrm{m}$, compared to $20\,\mu\mathrm{m}$ in the 2022 prototype, ensuring uniform gaps.

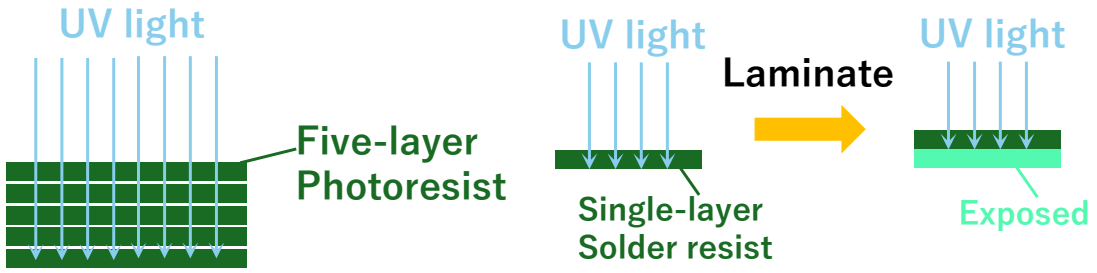

(a) 2019 **(b)** 2023

Figure 6.1: Schematic images of processes on pillar formation.

Table 6.1: Thickness of pillars for different diameters.

Diameter	Thickness
400 µm	333 ± 5 µm
500 µm	343 ± 5 µm
600 µm	355 ± 6 µm

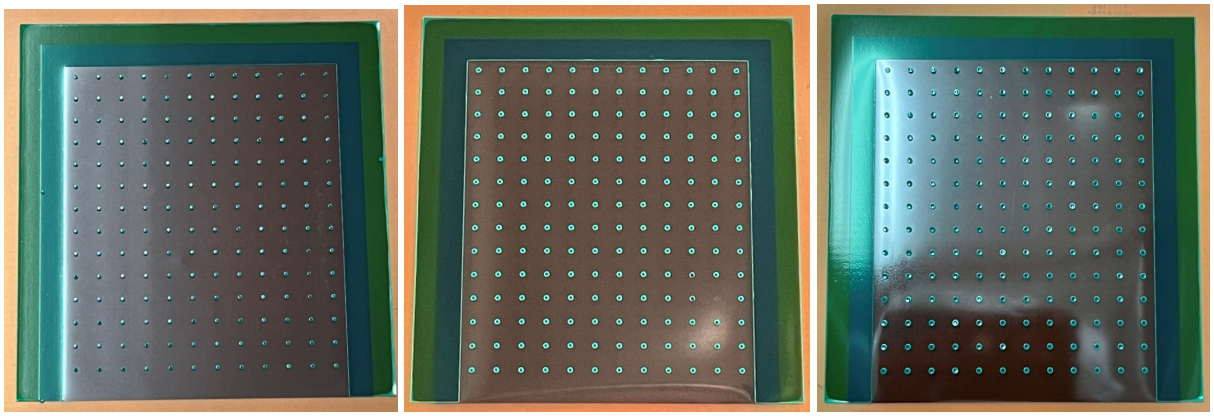

(a) 400 µm sample **(b)** 500 µm sample **(c)** 600 µm sample

Figure 6.2: Electrode samples produced at CERN in 2023. Active region: 30 mm × 37 mm.

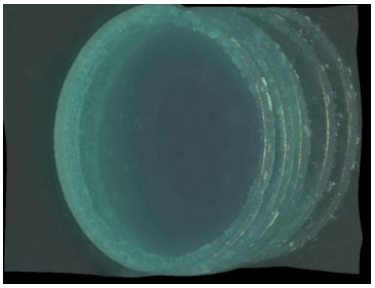

Figure 6.3: Oblique view of the pillar on a 2023 600 µmϕ electrode.

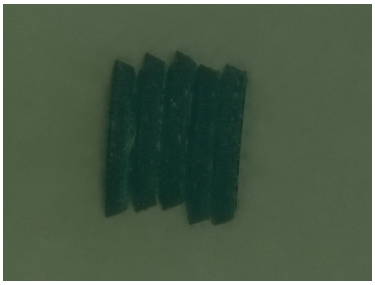

Figure 6.4: Lateral view of the pillar on a 2023 600 µmϕ electrode.

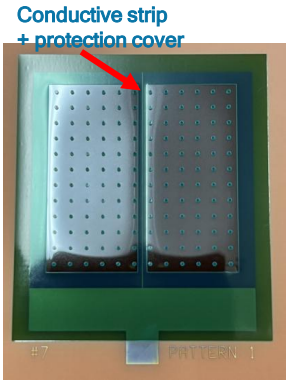

Figure 6.5: Electrode samples produced at CERN in 2024.

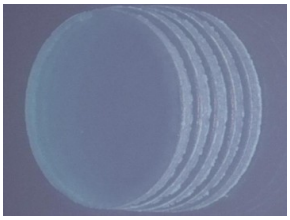

Figure 6.6: Oblique view of the pillar on the 2024 electrode.

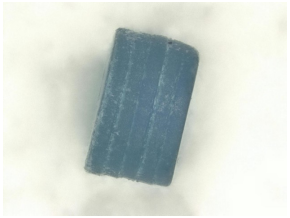

Figure 6.7: Lateral view of the pillar on the 2024 electrode.

6.2.2 2024 electrodes

With the improved quality of the pillar, electrodes featuring both pillars and a conductive strip were produced at CERN. A sample is shown in Figure 6.5. Pillars with a diameter of $600\,\mu\mathrm{m}$ are selected due to their good adhesion to the DLC layer on the anode side. Furthermore, as shown in Figure 6.6 and 6.7, the alignment of each layer of pillars was improved. Compared to a pillar on the 2023 electrode shown in Figure 6.3, each layer in the 2024 electrode is stacked precisely at the center of the pillar. The thickness measured at $372 \pm 2\,\mu\mathrm{m}$. Additionally, a conductive strip and a protective cover on top of the strip are placed at the center of the electrode. The process of the fabrication is the same as the 2022 prototype as shown in Figure 4.20, but in the 2024 electrodes, the width of the conductive strips and the diameter of the pillars are $0.1\,\mathrm{mm}$ and $600\,\mu\mathrm{m}$, respectively.

6.3 Signal detection performance of the prototypes

The setup for measuring the response to β-rays is the same as in Figure 5.2 in Section 5.1. A 2023 electrode is used as the anode. A notable difference from the setup in Figure 5.2 is that the active region is $30\,\mathrm{mm} \times 37\,\mathrm{mm}$. β-rays are irradiated to a part of the active region through a $2\,\mathrm{mm}\phi$ aluminum (Al) collimator.

6.3.1 Signal detection performance with 2023 electrodes

The pulse height spectra of the signal from the setup using a 2023 electrode are shown in Figure 6.8 for four values of HVs. The analysis threshold of the signal was set to $20\,\mathrm{mV}$, and the detection efficiencies are determined, as indicated in Figure 6.8. The average signal height increases with the applied HV.

The relation between efficiency and the applied voltage is depicted in Figure 6.9. The detector achieved the detection efficiency of 45 % or above, expecting 90 % for a four-layer detector estimated from Eq. 4.2.

The operation remained stable for a few hours at voltages up to $2.65\,\mathrm{kV}$, where efficiency is more than 45 %, ensuring sufficient performance. Discharges causing breakdown were less likely to happen than with the 2022 prototype. Therefore, the uniform pillar of the 2023 electrode, providing the stable structure, led to stable operation for at least a few hours, and this type of the pillar was chosen for the prototypes hereafter.

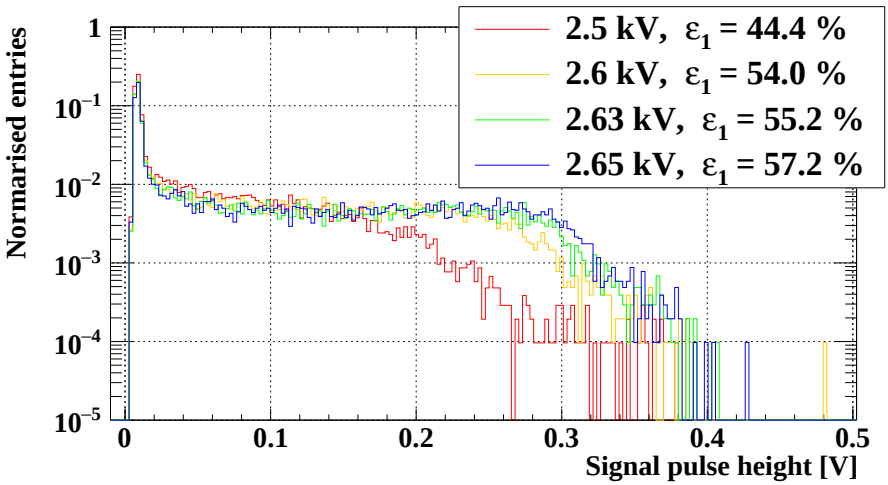

Figure 6.8: Pulse-height spectra of β rays with a 2023 electrode.

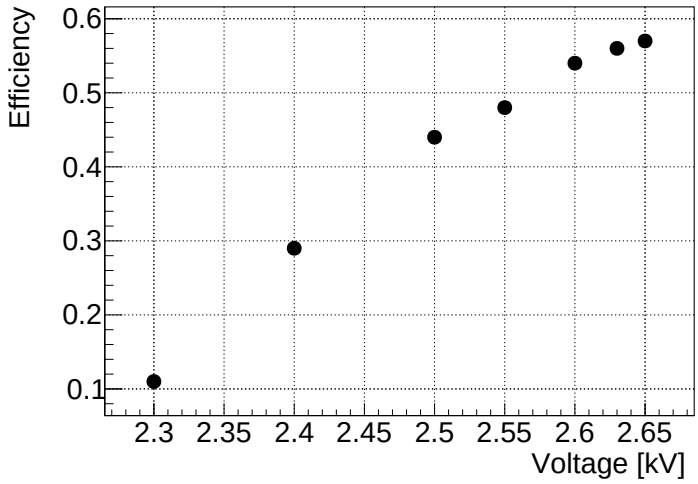

Figure 6.9: Detection efficiencies for β-rays.

6.3.2 Signal detection performance with 2024 electrodes

The pulse height distributions of the signal with the 2024 electrode are shown in Figure 6.10. Efficiency of 45 % at more than 2.5 kV and above was also obtained with the 2024 electrode, as shown in Figure 6.11.

6.4 Investigation on the conductive strip

On the DLC-RPC electrodes, conductive strips are overlaid with protective covers to prevent discharges above them. Figure 6.12 shows the quenching process of a current on the DLC-RPC. The current flows on the surface of the electrode and the gas amplification process is quenched. Quenching capability is determined by the effective resistances, Ω_{effA} and Ω_{effC}, corresponding to the anode and cathode, respectively. Equation 6.1 gives the relation between Ω_{effA} and the width of the cover w.

$$\Omega_{\mathrm{effA}} = \rho_{\mathrm{sA}} \cdot \frac{w - 0.1\,\mathrm{mm}}{2 \cdot k} \tag{6.1}$$

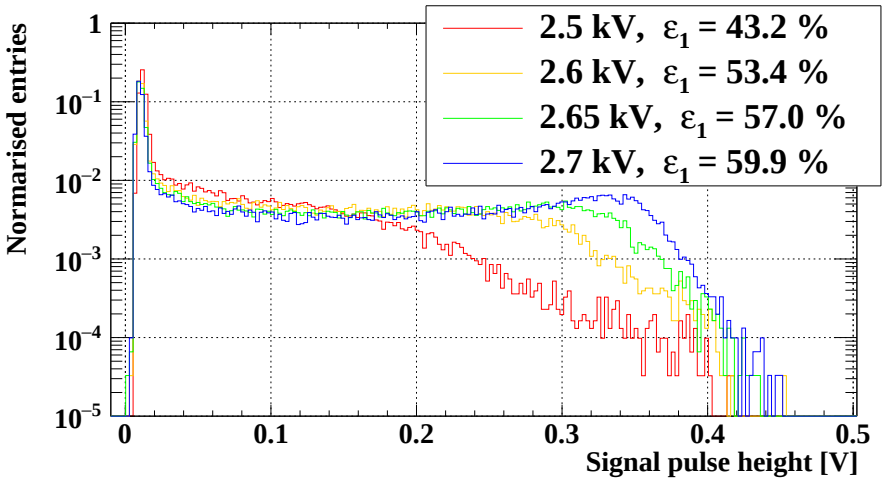

Figure 6.10: Pulse-height spectra of β rays with the 2024 electrode.

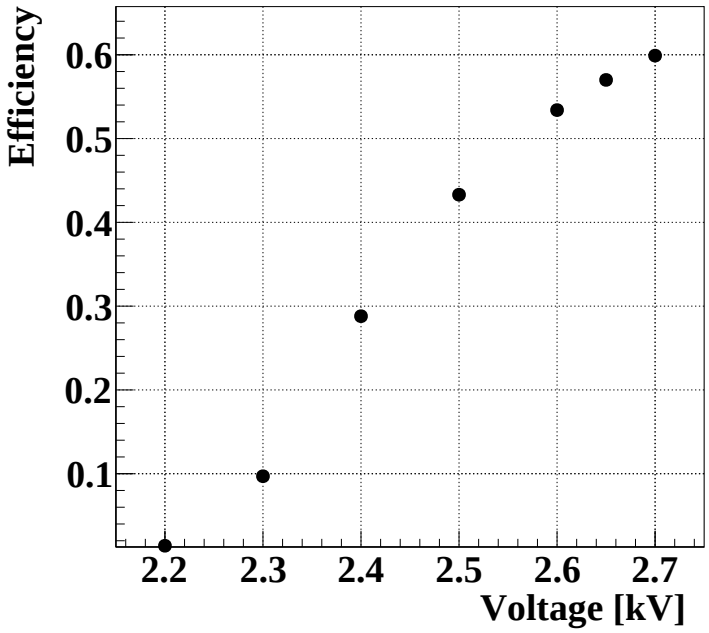

Figure 6.11: Detection efficiencies for β-rays.

where k is the length of the strip: $30\,\mathrm{mm}$ for the 2024 prototype electrodes. ρ_{sA} is the surface resistivity of the anode. As w gets larger, Ω_{eff} also becomes larger, giving stronger quench capability. However, a large w reduces the active region. To balance the two aspects, w must be optimized. Same as increasing w, stronger quench capability will be improved by increasing the surface resistivity, but the rate capability will get lower.

6.4.1 Measurements

Protective covers on the 2024 electrodes with widths of $0.2\,\mathrm{mm}$, $0.3\,\mathrm{mm}$, $0.4\,\mathrm{mm}$, $0.6\,\mathrm{mm}$, $0.8\,\mathrm{mm}$, and $1.0\,\mathrm{mm}$ were fabricated and the investigation was conducted on the widths. The current behavior is measured by applying β-rays with the rate of $\mathcal{O}(1\,\mathrm{MHz/cm^2})$ to it at the target voltage V_{T}. The setup is shown in Figure 6.13. The conductors (copper tapes) are on the cathode at a pitch of $2l_{\mathrm{pitch}}$.

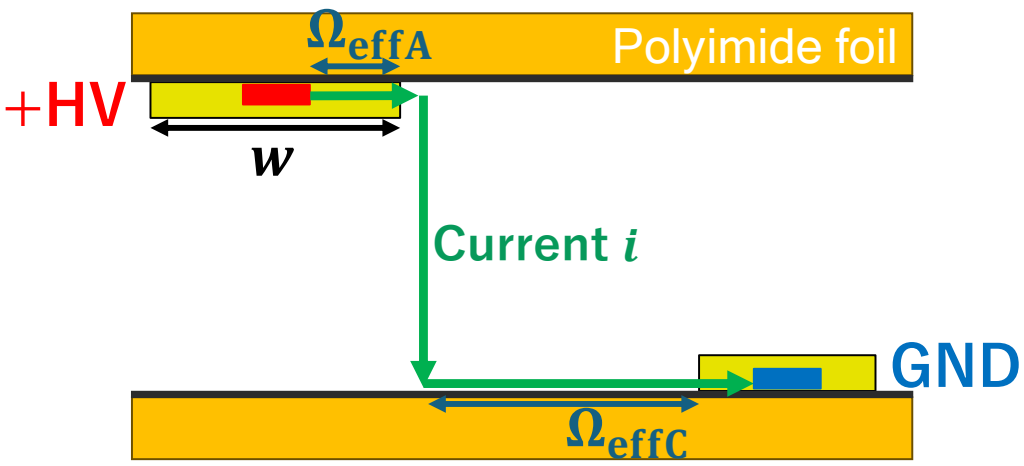

Figure 6.12: Schematic view of the current quenching process.

The value of l_{pitch}, 14 mm in this case, is chosen to provide large enough δV (see section 4.3.4) so that the δV exceeds 100 V for the resistive electrodes with their surface resistivity of 10 MΩ/sq or above. V_{T} is determined by adding δV to the voltage, V_{45}, i.e.$V_{\text{T}} = \delta V + V_{45}$ where efficiency is 45 % for β-rays, taking into account the voltage drop δV at the full rate of the muon beam during the actual experimental operation. The total voltage drop δV is calculated by integrating voltage drops at positions between the two strips, based on Eq. 4.3; an example of the result of the calculation is shown in Figure 6.14.

6.4.2 Results

Table 6.2 summarizes the test conditions and operation duration for various w and l_{pitch}. Ω_{effC}, the resistance between the current position and the ground strip as given in Figure 6.12, is defined as

$$\Omega_{\text{effC}} = \rho_{\text{sC}} \cdot \frac{2l_{\text{pitch}} - (w - 0.1\,\text{mm})}{2 \cdot k}. \tag{6.2}$$

It was likely to be unstable with a narrower cover, providing low Ω_{effA}. For Measurements 1 and 3, they could not reach the target voltage. For these runs, it was concluded that it is ascribed to low Ω_{effA}, which is not enough to quench the current. In contrast, the tests with higher resistivity, therefore Ω_{effA}, resulted in stable operation for at least one hour.

Focusing Measurements 4 to 6, the operation was stable enough to reach the target voltage and run for 2 hours with Ω_{effA} of 0.07 to 0.15MΩ, at the operating voltage equal to V_{T}. To minimize the inactive region, the effective resistance of 0.07 MΩ or above is chosen as a criterion for Ω_{effA} from the results, taking an optimal balance between its efficiency and quenching capability. No correlation with the stability was observed for Ω_{effC}.

The current behavior recorded for the operating voltage below V_{T} was investigated. The history of Measurement 6 is shown in Figure 6.15. The detector run at two voltages, 2530 V and 2580 V during this measurement. As shown in Table 6.2, more stable operation was seen at 2530 V, for it lasted for 2 hours compared to the 1-hour operation at 2580 V. It is considered that discharges, which cause breakdowns, are less likely to occur due to the weak electric field. Lower voltages may be a possible compromise as the minimum operation voltage for the long-term operation.

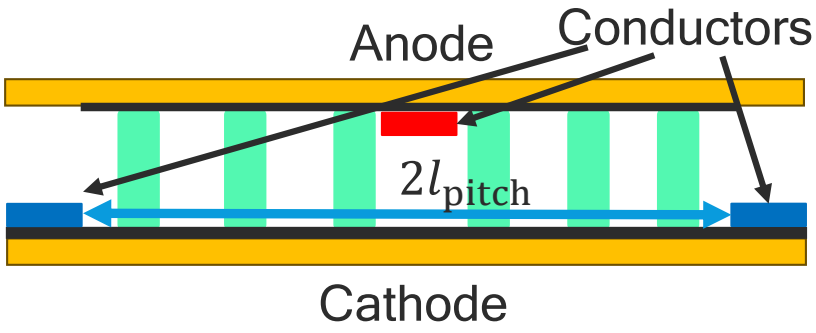

(a) Schematic image of the setup.

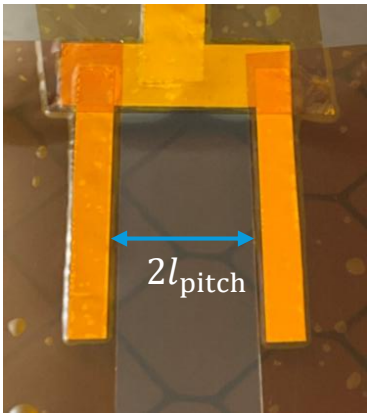

(b) Copper tapes on the cathode.

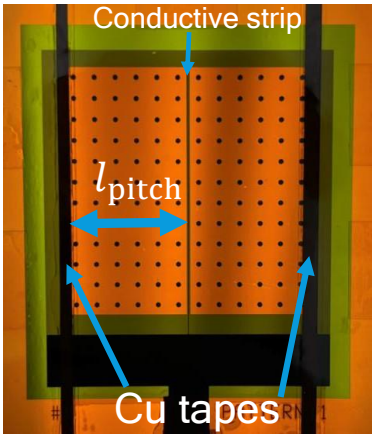

(c) Conductive strips and cu tapes.

Figure 6.13: Setup with conductors (Copper taps) on the cathode.

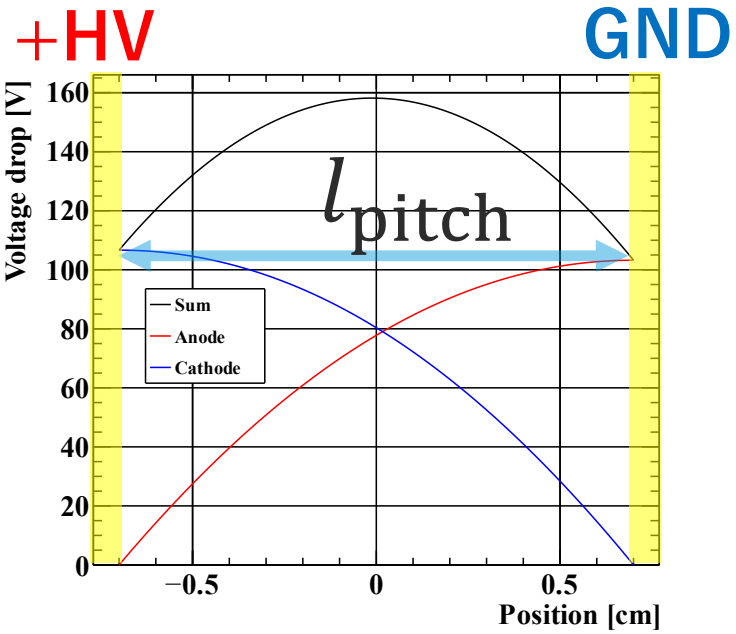

Figure 6.14: The calculation of the voltage drop. The origin of the position is taken as the middle point of the +HV and GND.

Table 6.2: Test conditions and operation duration with different cover widths. See text for details.

Measurement	w [mm]	ρ_{sA} [MΩ/sq.]	Ω_{effA} [MΩ]	ρ_{sC} [MΩ/sq.]	Ω_{effC} [MΩ]	l_{pitch} [mm]	δV [V]	V_{45} [V]	V_T [V]	Results
1	0.2	11.8	0.02	11.0	4.6	12.5	100	2540	2640	Unstable at 2570 V
2	0.3	13.5	0.05	11.0	4.5	12.5	105	2580	2680	Unstable at 2570 V
3	0.2	11.8	0.02	14.0	6.5	14.0	140	2480	2620	Unstable at 2570 V
4	0.4	14.5	0.07	14.0	6.5	14.0	155	2480	2630	Stable at 2630 V for 1.5 h
5	0.6	11.0	0.09	14.0	6.4	14.0	135	2480	2600	Stable at 2600 V for 2 h
6	1.0	10.0	0.15	11.0	5.2	14.5	120	2460	2580	Stable at 2580 V for 1 h

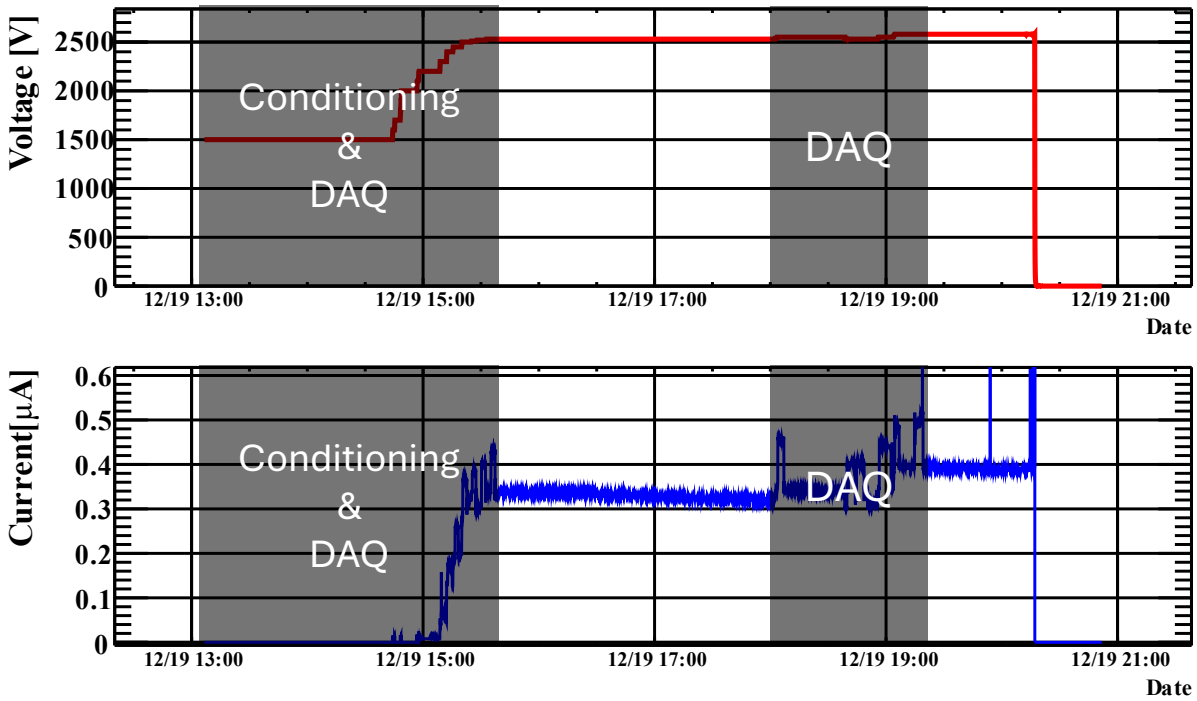

Figure 6.15: An example of the detector behavior for the measurement 6. Red: voltage, Blue: current, Horizontal axis: date.

6.5 Long-term operation of the 2024 electrodes

As discussed in Chapter 4, stable operation for 20 weeks is required for the US-RDC. However, discharges on the DLC-RPC have prevented the operation in the past irradiation tests. Tests were carried out to investigate the long-term stability of the RPC detector using the 2024 electrodes.

6.5.1 Measurements

The operating voltage was determined by the gas gain and the detection efficiency. As remarked in Section 4.3.4, the DLC-RPC is designed, assuming the voltage drop, δV, of about 100 V in the high-rate muon beam. Consequently, the applied voltage between the anode and cathode planes is reduced. Therefore, the operating voltage should be set 100 V higher than the threshold voltage value V_{45}, where the detection efficiency is 45 %. For example, the operating voltage of 2600 V was chosen for the case where the 45 % efficiency points given by $V_{45} = 2500$ V from Figure 6.11 in these tests.

β-rays with two different rates were irradiated to the detector, and the detector operated until the

overcurrent flows for more than one second. The irradiation tests at the rate of about $300\,\mathrm{kHz}$ and $\mathcal{O}(10\,\mathrm{kHz})$ were performed. The rate was adjusted by changing the distance between the detector and the β-ray source.

6.5.2 Results

The voltage and current histories of a long-term irradiation test at the high rate are shown in Figure 6.16. The operation lasted for 8 hours. Some current spikes were observed during the operation. Finally, large currents terminated the operation. A few operations continued for 20 to 30 hours, but the majority of the operations done at the high rate had to be terminated in several hours.

An example of the histories of a long-term irradiation test at the low rate are shown in Figure 6.17. Contrary to the high rate, it lasted for 60 hours at $2600\,\mathrm{V}$ and 48 hours at $2625\,\mathrm{V}$. The frequency of current spikes increased at $2625\,\mathrm{V}$. Current fluctuation seen in Figure 6.17 was due to variations of the atmospheric conditions, as shown in Figure 6.18, and imprecise positioning of the β-ray source.

Waveform data were recorded six times at each voltage. The pulse-height spectra at two voltages are shown in Figure 6.19. No significant changes in the pulse-height spectra were seen between each period of the data taken at the same high voltage with an agreement within 6.7 % and 15 %, respectively. This implies that consistent performance was observed for these two high-voltage values in terms of the detector response to β-rays.

The results of the long-term operation show that the DLC-RPC is not yet capable of operating for 20 weeks. Discharges, which terminate the operation, can happen even at a low rate. Moreover, discharges have mainly been observed on pillars and strips, as shown in Figure 6.20 and Figure 6.21, for example. It is thought that pillars and strips are weak points, where large avalanches are likely to happen. Currently, the causes of such discharges are not understood clearly.

6.6 Summary

To solve the issues in the 2022 prototype, the 2023 electrodes were fabricated using the new material for the formation of pillars in 2023. As a result, the distortion of the electric field was eliminated, and better operation was provided than the 2022 prototype.

The conductive strips and protective covers were attached to electrodes in 2024. The efficiency for β-rays for the 2024 prototype was as high as that for the 2023 prototype. Its stabilities in terms of long-term operation and quenching capability dependence on the protective cover widths were investigated. $\Omega_{\mathrm{effA}} = 0.07\,\mathrm{M\Omega}$ or above allowed to raise HV beyond the operation point estimated from the HV value where efficiency exceeds 45 % for β-rays, and estimated voltage drop calculated from the surface resistivity and the muon rate. However, there are still issues with the long-term operation. Discharges halt the operation occurring at a certain point. The marks were mainly seen on the pillars and the covers, which are considered to be weak points on the detector.

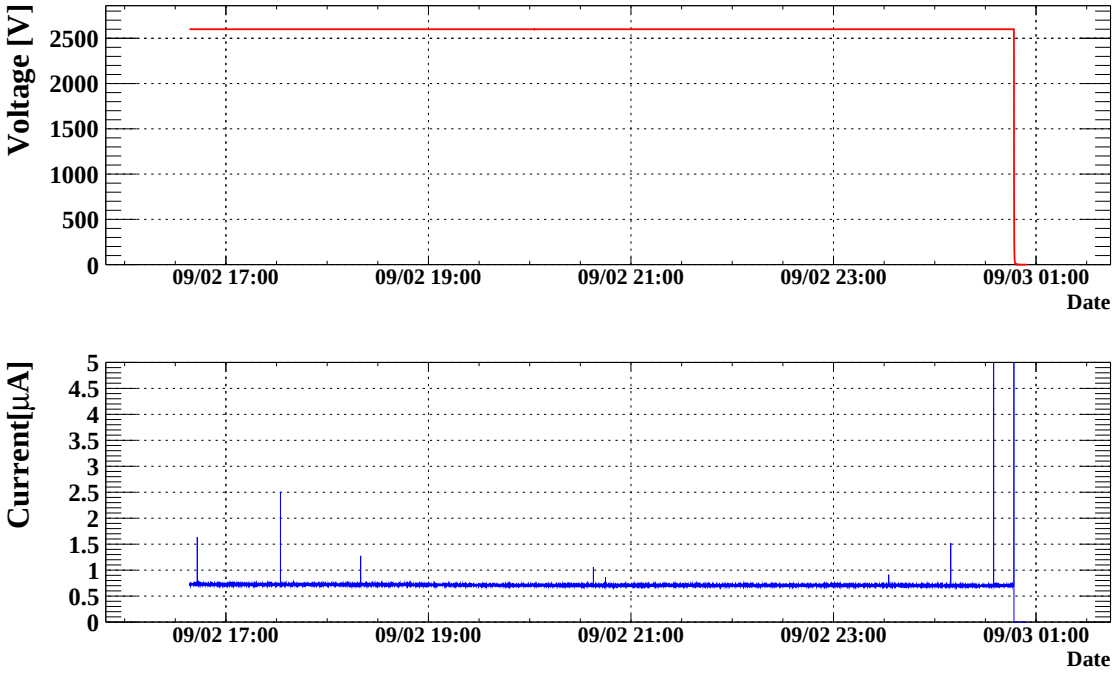

Figure 6.16: Long-term operation with high rate of about 300 kHz. Red: Voltage, Blue: Current, Horizontal axis: date.

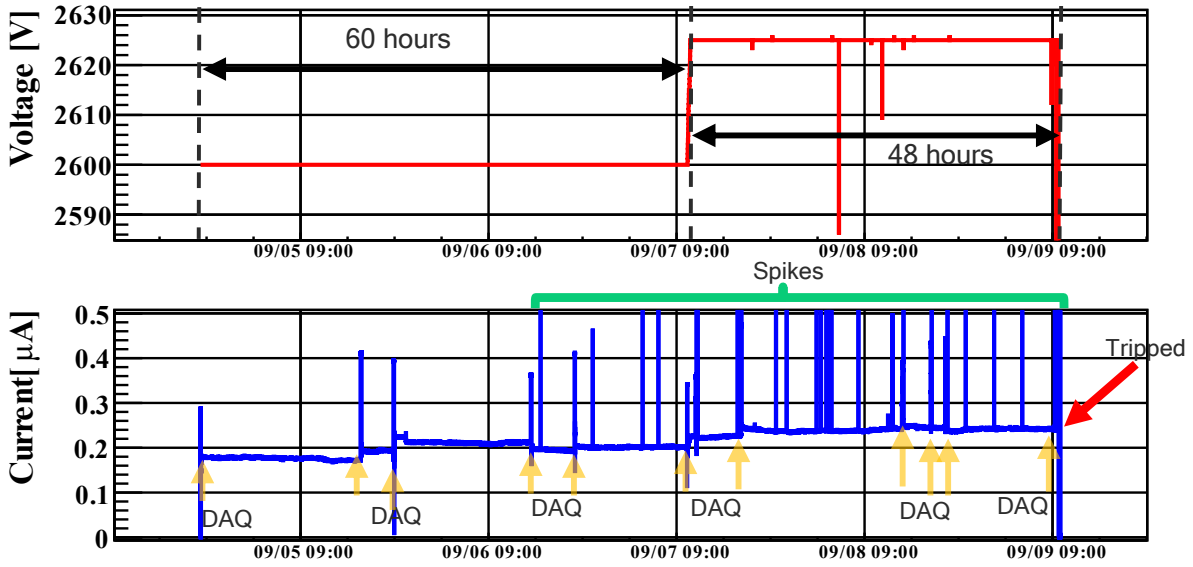

Figure 6.17: Long-term operation with low rate of $\mathcal{O}(10\,\mathrm{kHz})$. Red: voltage, Blue: current, Horizontal axis: date.

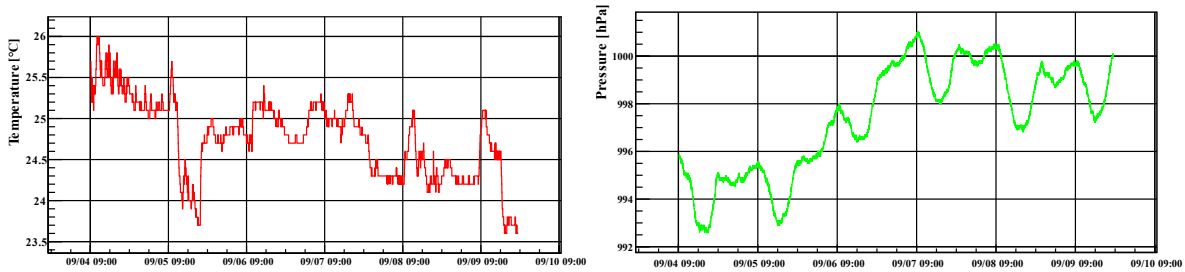

(a) Temperature, horizontal axis: date.

(b) Atmospheric pressure, horizontal axis: date.

Figure 6.18: Changes in the atmospheric conditions during the long-term operation.

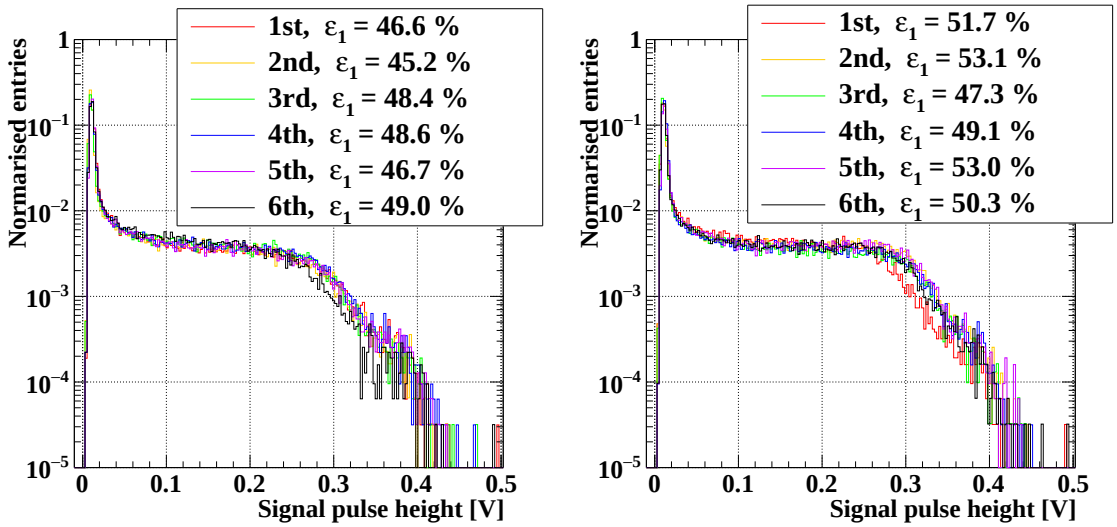

(a) 2600 V.

(b) 2625 V.

Figure 6.19: The pulse-height spectra at 2600 V and 2625 V during the long-term operation.

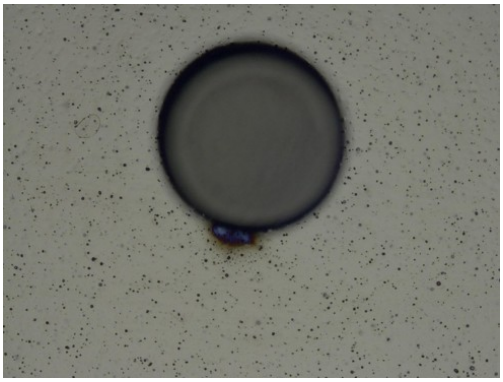

Figure 6.20: A discharge on a pillar.

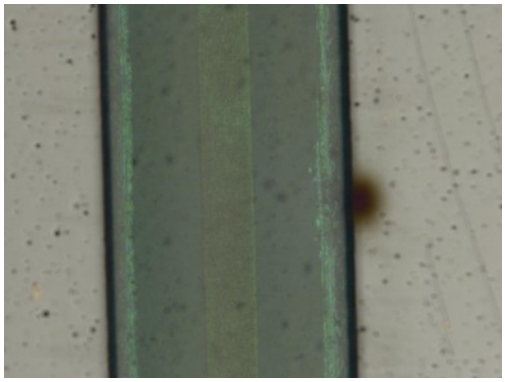

Figure 6.21: A discharge on a protective cover.

Chapter 7

Conclusion

The aging test and development and performance evaluation of the electrodes were conducted to address issues identified in previous studies for the DLC-RPC developed for the upstream RDC for the MEG II experiment.

The aging test was performed using X-rays to investigate the effect of aging at KEK in 2023. The total irradiation dose reached $54\,\mathrm{C/cm^2}$, which is more than 100 times larger than the previous study in 2022 and reaches approximately half the dose expected in MEG II. The degradation of the gas gain was observed, equivalent to operating at 50–$100\,\mathrm{V}$ lower voltage. Fluorine formed during the irradiation and rendered the affected region inactive.

New electrodes with higher pillars made from the new material were fabricated by the MPT workshop at CERN in 2023, providing a structure with uniform gas gaps for homogeneous electric fields. Stable operation was observed, and the detection efficiency of 45 % for β-rays with a single layer was achieved, expecting the efficiency of 90 % for a four-layer detector. In 2024, the 2024 electrodes incorporating new pillars, conductive strips, and protective covers for the strips were produced, and their performance was evaluated, demonstrating the same performance as the 2023 electrodes. The protective cover width and the arrangement of conductors on the cathode for improving the rate capability were investigated. By monitoring the current behavior and the stability at the target voltage, $\Omega_{\mathrm{effA}} = 0.07\,\mathrm{M\Omega}$ or above is determined as the condition for stable operation.

However, the operation of the detector lasts no more than several hours due to the discharges. Long-term operation tests showed that the detector could function for several hours at high rates. The discharges, also preventing the long-term operation, caused damage primarily to the pillars and protective covers. The causes of them must be clarified and measures against them are needed.

The formation of fluorine induces the inactive region, which results in the degradation of the gas gain. To overcome this issue, the gas should be replaced faster to operate with cleaner gas, and the optimization of the gas flow is required. In order to suppress discharges preventing stable long-term operation, a possible solution is to lower the operating voltages, although this causes a drop in the positron detection efficiency. Besides, the stable operation should be realized by taking into account other parameters, such as increasing the resistivity for better quenching capability and higher pillars to increase the gas gap for larger ionization to improve the efficiency, which may allow the operating voltage to be lowered.

These improvements should be incorporated into the design of the full-scale prototype module, scheduled for fabrication in 2025. Its performance will be evaluated using a high-rate muon beam. The detector may be installed for the MEG II physics run in 2026 if the full-scale prototype satisfies all requirements.

Appendix

A X-ray intensity measurement

To measure an X-ray intensity, an ionization chamber was made for the aging test in 2023.

A.1 Operation principle of the ionization chamber

The ionization chamber consists of two electrodes, with a high voltage applied across a gas gap. When particles enter this gap, they ionize the gas molecules, generating electrons and anions, as shown in Figure A.1. As a result, the ionized electrons drift toward the anode, creating a current flowing through the chamber.

Figure A.2 shows the relation between the number of ionized electrons and applied voltages. The ionization chamber operates in the region (2) as indicated in Figure A.2. In this region, the number of ionized electrons remains constant; gas amplification does not occur. Therefore, a response proportional to the ionization energy loss can be measured, allowing for the measurement of radiation intensity.

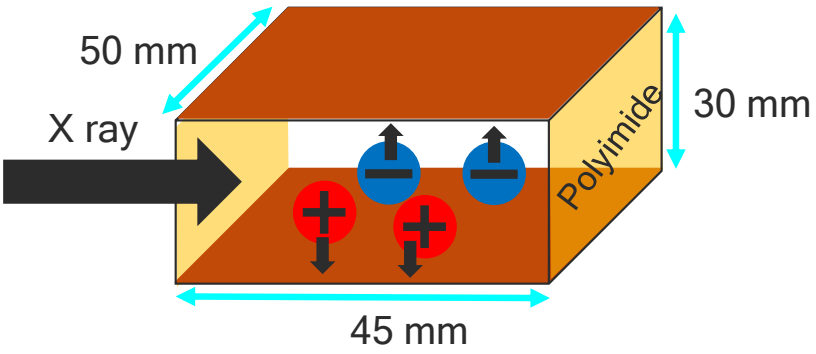

Figure A.1: A schematic illustration of the ionization chamber.

A.2 Design and production of the ionization chamber

The fabricated ionization chamber is shown in Figure A.3. Its dimensions are $L \times W \times T = 50 \times 45 \times 30$ mm. Two parallel copper tapes face each other, composing a gas gap of 30 mm. The chamber body is made of acrylic plates. Two chamber windows are on the top and bottom (the $L \times T$ face) polyimide foils. The X-rays enter the window. For the gas for ionization, argon (Ar) was chosen for its large energy loss against X-rays.

A.3 Setup

The setup for the X-ray intensity measurement using the ionization chamber is shown in Figure A.4. The measurement procedure of the X-ray intensity is as follows:

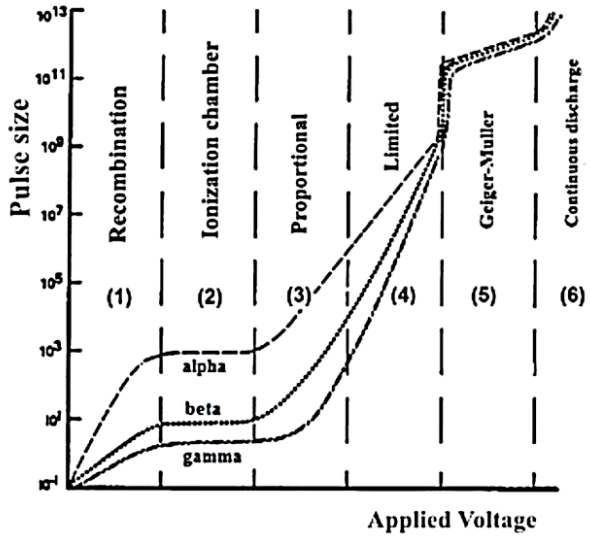

Figure A.2: The relation between the number of ionized electrons (Vertical axis) and applied voltages (Horizontal axis) [49].

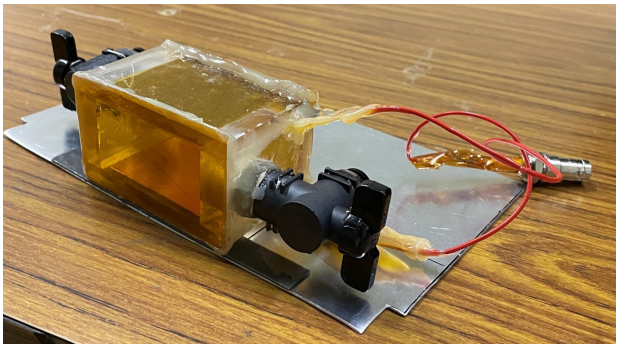

Figure A.3: The fabricated ionization chamber.

- Apply voltage to the ionization chamber in increments of $100\,\mathrm{V}$
- Irradiate the chamber with the same X-ray as in the aging test (Tube current: $30\,\mathrm{mA}$, Tube voltage: $50\,\mathrm{kV}$)
- Measure the current for each applied voltage when the X-ray is on and off, to evaluate the leakage current in the ionization chamber
- Finding an operating condition for the ionization region by identifying the voltage range where the differences between the two measured currents remain constant
- Estimate the X-ray intensity from the current difference.

The chamber current dependence on tube current and tube voltage was investigated separately. With the ionization chamber operating at a given voltage, either the tube current or voltage was varied while keeping the other parameter constant, and the corresponding current differences were measured.

Additionally, the X-ray profile was also measured. A $1\,\mathrm{mm}\phi$ (Pb) collimator is placed $2\,\mathrm{cm}$ in front of the ionization chamber window. The xyz coordinate system is defined relative to the output window, as shown in Figure A.5: x represents the horizontal direction, y the vertical direction, and z-axis aligns with the X-ray direction. The origin was set at the center of the output window. The setup for the X-ray profile measurement is shown in Figure A.6. The X-rays (Tube current: $30\,\mathrm{mA}$, Tube voltage: $50\,\mathrm{kV}$) irradiate the chamber through the collimator at measurement points spaced in

1 mm steps within the range ($-0.4\,\mathrm{cm} < x < 0.4\,\mathrm{cm}$, $-0.4\,\mathrm{cm} < y < 0.4\,\mathrm{cm}$). At each point, the current difference between X-ray on and off was recorded.

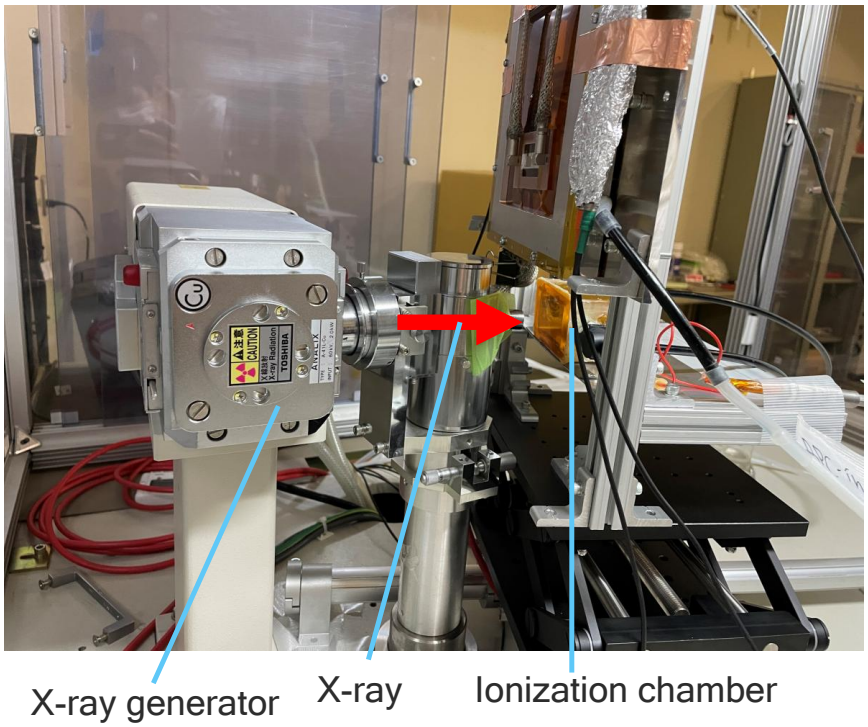

Figure A.4: Setup for the X-ray intensity measurement using the ionization chamber.

A.4 Results

Determation of the operating voltage

The observed currents as a function of the applied voltage between two electrodes of two days are shown in Figure A.7. It was found that the current remained constant from 700 V onward. No significant difference was observed in the currents in the plateau region between the measurements from day 1 and day 2. The operating voltage of the ionization chamber was set to 1000 V, as this value was guaranteed to be within the ionization region. At this voltage, a current of 17 nA flowed through the chamber.

Calculation of the X-ray intensity

The intensity I at position z is expressed with the intensity at $z = 0$, I_0 as follows:

$$I = I_0 \exp(-\mu\rho z). \tag{A.1}$$

where μ is the photoelectric absorption coefficient of Ar for 8 keV X-rays, and ρ is the density of Ar. The number of photons absorbed in the ionization chamber is given by:

$$I_0 - I_0 \exp(-\mu\rho z). \tag{A.2}$$

The resulting current flowing through the chamber i is calculated using elementary charge e, the X-ray energy E, and the work function of Ar W:

$$i = \frac{E}{W} \times I_0\{1 - \exp(-\mu\rho z)\} \times e. \tag{A.3}$$

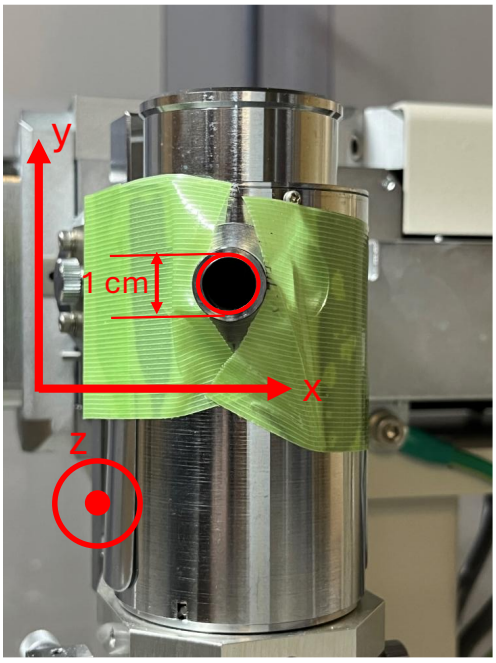

Figure A.5: The output window and xyz coordinates.

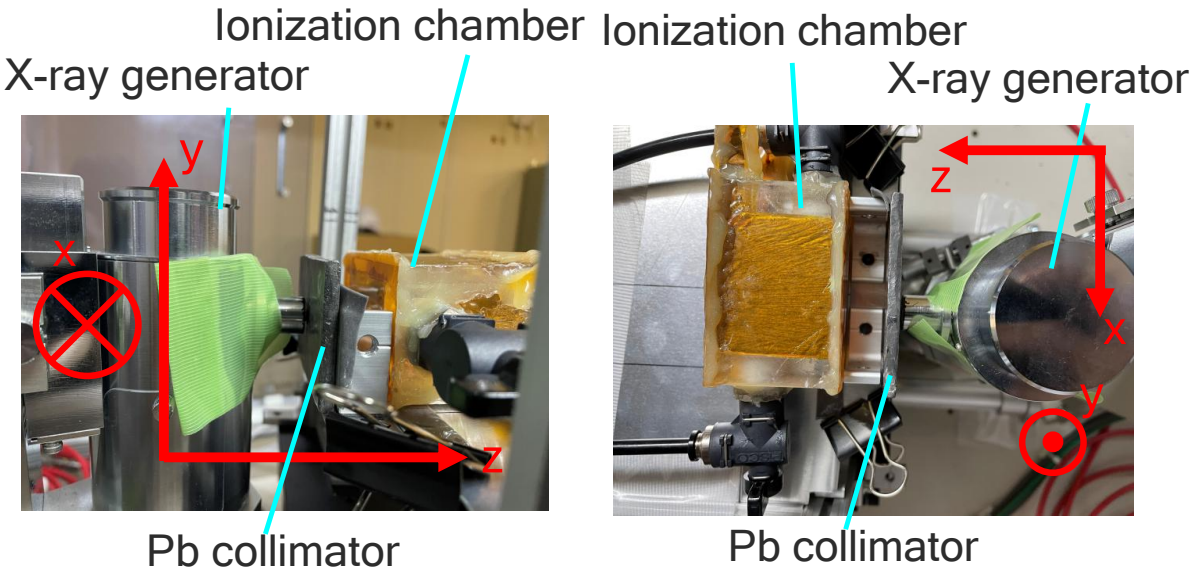

(a) Lateral view.

(b) Top view.

Figure A.6: Setup for the X-ray profile measurement.

Therefore, the X-ray intensity is determined as follows:

$$I_0 = \frac{i}{e} \cdot \frac{W}{E}\{1 - \exp(-\mu\rho z)\}^{-1}. \tag{A.4}$$

Substituting the known values $i = 17\,\mathrm{nA}$, $e = 1.602 \times 10^{-19}\,\mathrm{C}$, $W = 26\,\mathrm{eV}$, $E = 8.04\,\mathrm{keV}$, $\mu = 117\,\mathrm{cm}^2/\mathrm{g}$ [50], $\rho = 1.7 \times 10^{-3}\,\mathrm{g/cm}^3$, and $z = 4.5\,\mathrm{cm}$. we obtain:

$$I_0 = (5.99 \pm 0.03) \times 10^8\ \mathrm{photon/s}. \tag{A.5}$$

Dependence on tube current and tube voltage

The dependence of intensity on tube voltage is shown in Figure A.8. The tube current was set to $2\,\mathrm{mA}$ to prevent abnormal operation of the X-ray generator at low tube voltages. As the tube voltage increased, the intensity also increased.

The dependence of intensity on tube current is shown in Figure A.9. The tube voltage was set to $50\,\mathrm{kV}$. Since the X-ray intensity is proportional to the tube current, a linear fit was applied to the data. The results confirmed that intensity was directly proportional to the tube current.

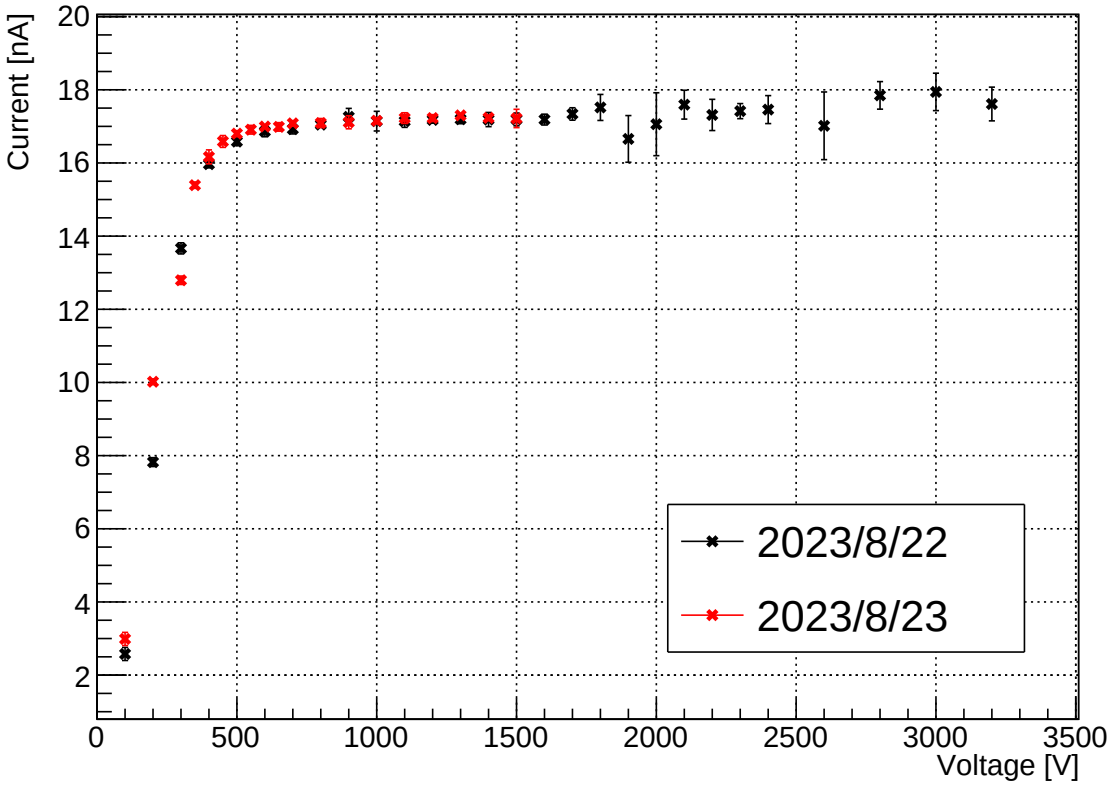

Figure A.7: The current flew in the ionization chamber.

X-ray profile

The result of the X-ray profile measurement is shown in Figure A.10. The data revealed that the intensity was localized at $(-0.2\,\mathrm{cm},\ 0.2\,\mathrm{cm})$ and spread vertically within a $1\,\mathrm{mm} \times 3\,\mathrm{mm}$ region, despite the expected $1\,\mathrm{cm}\phi$ circular distribution. This deviation was attributed to the collimator shape

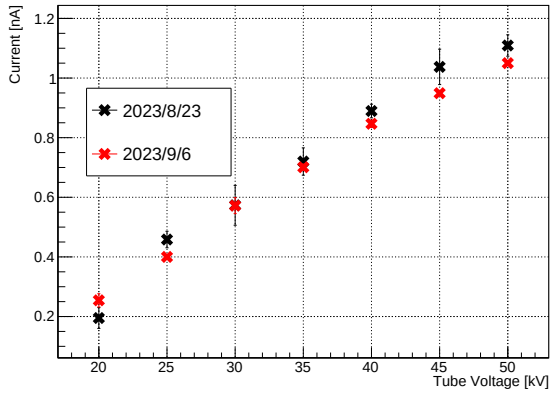

Figure A.8: Dependence of tube voltage vs intensity in the IC (Tube current: 2 mA).

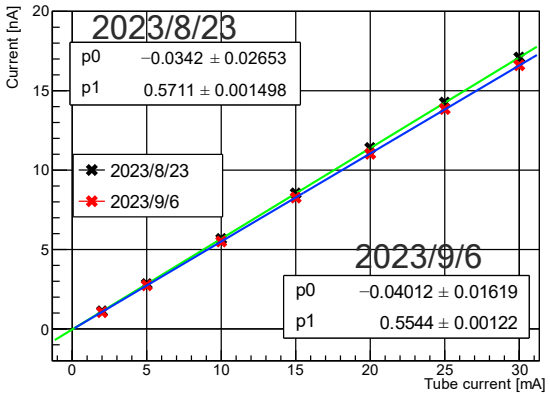

Figure A.9: Dependence of tube current vs intensity in the IC (Tube current: 50 kV). Fitted with a linear function (p1: Slope, p0: y-intercept).

of the X-ray generator. As a result, the irradiation range was narrower than anticipated, affecting the calculation of the irradiation dose.

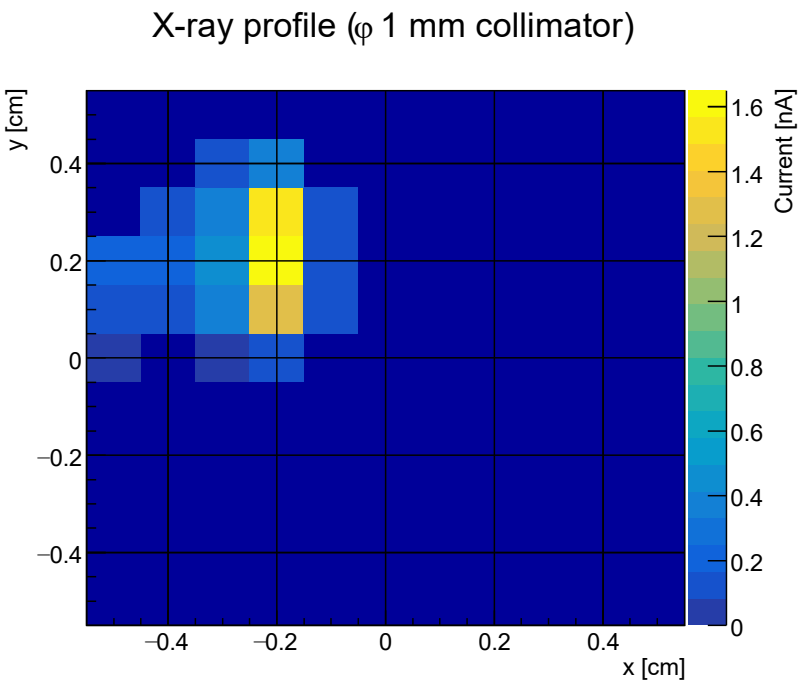

Figure A.10: X-ray profile measured by the ionization chamber.

Acknowledgements

I would like to express my deepest gratitude to Prof. Atsuhiko Ochi, who introduced me to the world of gaseous detectors. I learned a lot about experimental particle physics and enjoyed my research opportunities he provided with me at Kobe University. May he rest in peace.

I would like to express my sincere appreciation to Mr. Masato Takahashi and Prof. Yuji Yamazaki for their guidance throughout my research. Despite the challenges after the unfortunate passing of Prof. Atsuhiko Ochi, Prof. Yuji Yamazaki has always been eager to support us and engage in insightful discussions from different perspectives, which have greatly stimulated me. Mr. Masato Takahashi carries out our research with me and helps me whenever needed. I am always in awe of his passion and dedication to research. Let us take care of ourselves, we will never sacrifice our well-being for research. I will do my best for my doctoral study, emphasizing the importance of maintaining a healthy work-life balance.

I am particularly grateful to my second readers, Prof. Kentaro Miuchi and Prof. Eiichi Matsuoka.

I would like to thank Mr. Kensuke Yamamoto, Dr. Atsushi Oya, Mr. Weiyuan Li, Prof. Wataru Ootani, Dr. Sei Ban in RDC group, and Dr. Yusuke Uchiyama at KEK for carrying out our research together and supporting me in the meeting.

Furthermore, I would like to thank Prof. Hisaya Kurashige, Prof. Yasuo Takeuchi, Prof. Junpei Maeda, Prof. Atsumu Suzuki, Dr. Satoshi Higashino, and Ms. Junko Kitagawa for support and encouragement in Particle Physics Laboratory, Kobe University.

I would like to acknowledge Prof. Ken Sakashita at the Platform-C, KEK, Prof. Angela Papa, Dr. Malte Hildebrandt, Dr. Stefan Ritt, Ms. Anita Govaerts Van Loon at PSI, and Dr. Rui De Oliveira at CERN for their support in providing research facilities and for their dedicated efforts.

I am grateful for the camaraderie and time spent with Mr. Ryota Namai, Mr. Shota Nishi, Mr. Rukumo Higuchi, Mr. Ryugo Mizuhiki, Ms. Yui Murata, Mr. Haiwen Zhong, Mr. Haruki Morimoto, Mr. Li Zhang, Mr. Rintaro Yamaguchi, Mr. Yuma Sano, Mr. Yuki Asami, Mr. Kodai Taniguchi, Mr. Keita Sakura, Mr. Shinichiro Wada, Mr. Keishi Suzuki, Mr. Takamasa Sone, Mr. Ryosuke Tanaka, Mr. Mahiro Sasada, and undergraduate students in the laboratory.

I also appreciate the enjoyable discussions and moments mainly at PSI shared with Prof. Toshinori Mori, Dr. Toshiyuki Iwamoto, Dr. Lukas Gerritzen, Mr. Taku Yonemoto, Ms. Ayaka Matsushita, Mr. Ryusei Umakoshi, Mr. Taisei Takatsu, Mr. Hiroyasu Ogawa, Ms. Rei Sakakibara, Mr. Takumi Seino in the University of Tokyo, Prof. Satoshi Mihara at KEK, and Ms. Paphatchaya Kheawyoi.

References

[1] Fukuda. et al., Evidence for oscillation of atmospheric neutrinos, Physical review letters, Vol. 81, No. 8, p. 1562, 1998, DOI: 10.1103/PhysRevLett.81.1562.

[2] Ahmad, Q Retal. et al., Direct evidence for neutrino flavor transformation from neutral-current interactions in the Sudbury Neutrino Observatory, Physical review letters, Vol. 89, No. 1, p. 011301, 2002, DOI: PhysRevLett.89.011301.

[3] Baldini, AM. et al., Search for the lepton flavour violating decay $\mu^+ \to e^+\gamma$ with 10^{-14} with the full dataset of the MEG experiment, The European Physical Journal C, Vol. 76, No. 8, pp. 1–30, 2016, DOI: 10.1140/epjc/s10052-016-4271-x.

[4] Afanaciev, K. et al., A search for μ+$\to$ e+ γ with the first dataset of the MEG II experiment, The European Physical Journal C, Vol. 84, No. 3, p. 216, 2024, DOI: 10.1140/epjc/s10052-024-12416-2.

[5] Oya, A., Development of ultra-low material RPC detector for further sensitivity improvement of MEG II experiment, Master's thesis, The University of Tokyo, 2020.

[6] Yamamoto, K., Development of ultra-low mass and high-rate capable resistive plate chamber for background reduction in the MEG II experiment, Master's thesis, The University of Tokyo, 2022.

[7] Takahashi, M., Development of DLC-RPC for background suppression in MEG II experiment, Master's thesis, Kobe University, 2023.

[8] Higgstan, 2024, https://higgstan.com/.

[9] Particle Data Group, https://pdg.lbl.gov/.

[10] Crittenden, R. R. and Walker, W. D. and Ballam, J., Radiative Decay Modes of the Muon, Phys. Rev., Vol. 121, pp. 1823–1832, Mar 1961, DOI: 10.1103/PhysRev.121.1823.

[11] Kuno, Yoshitaka and Okada, Yasuhiro., Muon decay and physics beyond the standard model, Rev. Mod. Phys., Vol. 73, pp. 151–202, Jan 2001, DOI: 10.1103/RevModPhys.73.151.

[12] S.M. Bilenky and S.T. Petcov and B. Pontecorvo, Lepton mixing, $\mu \to e\gamma$ decay and neutrino oscillations, Physics Letters B, Vol. 67, No. 3, pp. 309–312, 1977, DOI: 10.1016/0370-2693(77)90379-3.

[13] Georgi, Howard and Glashow, Sheldon L, Unity of all elementary-particle forces, Physical Review Letters, Vol. 32, No. 8, p. 438, 1974, DOI: 10.1103/PhysRevLett.32.438.

[14] Yanagida, Tsutomu, Horizontal Symmetry and Masses of Neutrinos, Progress of Theoretical Physics, Vol. 64, No. 3, pp. 1103–1105, 09 1980, DOI: 10.1143/PTP.64.1103.

[15] Baldini, A. M. et al., The design of the MEG II experiment: MEG II Collaboration, The European Physical Journal C, Vol. 78, No. 5, may 2018, DOI: 10.1140/epjc/s10052-018-5845-6.

[16] Baldini, AM. et al., Muon polarization in the MEG experiment: predictions and measurements: The MEG Collaboration, The European Physical Journal C, Vol. 76, pp. 1–12, 2016, DOI: 10.1140/epjc/s10052-016-4047-3.

[17] Paul Scherrer Institut (PSI), The PSI proton accelerator, 2024, https://www.psi.ch/en/research/the-psi-proton-accelerator.

[18] Rossella, M et al., Test and characterization of SiPMs for the upgrade of MEGII high resolution Timing Counter, Journal of Instrumentation, Vol. 19, No. 03, p. C03004, 2024, DOI: 10.1088/1748-0221/19/03/C03004.

[19] K. Ieki. et al., Large-area MPPC with enhanced VUV sensitivity for liquid xenon scintil-

lation detector, Nuclear Instruments and Methods in Physics Research Section A: Accelerators, Spectrometers, Detectors and Associated Equipment, Vol. 1066, p. 169509, 2019, DOI: 10.1016/j.nima.2019.02.010.
[20] K. Afanaciev. et al., Operation and performance of the MEG II detector, The European Physical Journal C, Vol. 84, No. 2, p. 190, 2024, DOI: 10.1140/epjc/s10052-024-12415-3.
[21] Iwai, R., Development and commissioning of MEG II Radiative Decay Counter, Master's thesis, The University of Tokyo, 2017.
[22] Stefan Ritt and Roberto Dinapoli and Ueli Hartmann, Application of the DRS chip for fast waveform digitizing, Nuclear Instruments and Methods in Physics Research Section A: Accelerators, Spectrometers, Detectors and Associated Equipment, Vol. 623, No. 1, pp. 486–488, 2010. 1st International Conference on Technology and Instrumentation in Particle Physics, DOI: 10.1016/j.nima.2010.03.045.
[23] Oya, A., Search for $\mu \to e\gamma$ with the first year data of the MEG II experiment, Doctoral Dissertation, The University of Tokyo, 2023.
[24] Baldini, Alessandro. et al., The Search for $\mu^+ \to e^+\gamma$ with 10^{-14} Sensitivity: The Upgrade of the MEG Experiment, Symmetry, Vol. 13, No. 9, p. 1591, August 2021, DOI: 10.3390/sym13091591.
[25] Biagi, S., Imonte, program to compute gas properties.
[26] Werner Riegler and Christian Lippmann and Rob Veenhof, Detector physics and simulation of resistive plate chambers, Nuclear Instruments and Methods in Physics Research Section A: Accelerators, Spectrometers, Detectors and Associated Equipment, Vol. 500, No. 1, pp. 144–162, 2003. NIMA Vol 500, DOI: 10.1016/S0168-9002(03)00337-1.
[27] Lippmann, C., Detector Physics of Resistive Plate Chambers, Ph.D. dissertation, Frankfurt U, 2003.
[28] Raether, H., Electron avalanches and breakdown in gases, 1964.
[29] Francke, T and Peskov, V., Innovative Applications and Developments of Micro-Pattern Gaseous Detectors, 2014, DOI: 10.4018/978-1-4666-6014-4.
[30] R. Santonico and R. Cardarelli, Development of resistive plate counters, Nuclear Instruments and Methods in Physics Research, Vol. 187, No. 2, pp. 377–380, 1981, DOI: 10.1016/0029-554X(81)90363-3.
[31] G. Aielli. et al., Test and performances of the RPC trigger chambers of the ATLAS experiment at LHC, Nuclear Instruments and Methods in Physics Research Section A: Accelerators, Spectrometers, Detectors and Associated Equipment, Vol. 533, No. 1, pp. 193–198, 2004, Proceedings of the Seventh International Workshop on Resistive Plate Chambers and Related Detectors, DOI: 10.1016/j.nima.2004.07.026.
[32] Shah, MA. et al., The CMS RPC detector performance and stability during LHC RUN-2, Journal of Instrumentation, Vol. 14, No. 11, p. C11012, 2019, DOI: 10.1088/1748-0221/14/11/C11012.
[33] Liu, Z. et al., Novel low resistivity glass: MRPC detectors for ultra high rate applications, Nuclear Instruments and Methods in Physics Research Section A: Accelerators, Spectrometers, Detectors and Associated Equipment, Vol. 959, p. 163483, 2020, DOI: 10.1016/j.nima.2020.163483.
[34] Ogawa, K., 炭素スパッタを用いた積層型 Fast Timng RPC の開発, Master's thesis, Kobe University, 2018.
[35] Yamamomo, K., Studies on DLC characterisation, RD51 Collaboration Meeting, 2023.
[36] Ochi, A., Introduction to Resistive DLC collaboration, RD51 Mini-Week, 2018.
[37] PCS Instruments, The Science Behind Diamond like Coatings (DLCs), https://pcs-instruments.com/.
[38] TRENG F Products, Inc., https://www.treng-f-products.co.jp/.
[39] DuPont, https://www.dupont.com/.
[40] Be-Sputter, https://www.be-sputter.co.jp/.
[41] D. Bartos et al, Ageing studies of Multi-Strip Multi-Gap Resistive Plate Counters based on low resistivity glass electrodes in high irradiation dose, Nuclear Instruments and Methods in Physics

Research Section A: Accelerators, Spectrometers, Detectors and Associated Equipment, Vol. 1024, p. 166122, 2022, DOI: 10.1016/j.nima.2021.166122.

[42] Aly, R. et al., Aging study on Resistive Plate Chambers of the CMS Muon Detector for HL-LHC, Journal of Instrumentation, Vol. 15, No. 11, p. C11002, nov 2020, DOI: 10.1088/1748-0221/15/11/C11002.

[43] Quaglia, L. et al., Performance and aging studies for the ALICE muon RPCs, Journal of Instrumentation, Vol. 16, No. 04, p. C04002, apr 2021, DOI: 10.1088/1748-0221/16/04/C04002.

[44] Phan, N.S. et al., The novel properties of SF6 for directional dark matter experiments, Journal of Instrumentation, Vol. 12, No. 02, p. P02012, feb 2017, DOI: 10.1088/1748-0221/12/02/P02012.

[45] Rigaku, https://rigaku.com/.

[46] Masato Takahashi. et al., Radiation hardness studies of RPC based on diamond-like carbon electrodes for MEG II experiment, Nuclear Instruments and Methods in Physics Research Section A: Accelerators, Spectrometers, Detectors and Associated Equipment, Vol. 1066, p. 169509, 2024, DOI: 10.1016/j.nima.2024.169509.

[47] ULVAC-PHI, INCORPORATED., https://www.ulvac-phi.com/ja/?lang=ja_JP.

[48] Eternal Technology Corporation, https://eternaltechcorp.com/.

[49] Marcia Dutra R. Silva, Ionizing Radiation Detectors, Mitsuru Nenoi, Evolution of Ionizing Radiation Research, chapter 8, IntechOpen, Rijeka, 2015, DOI: 10.5772/60914.

[50] NIST, https://www.nist.gov/.